*People's Democratic Republic of Algeria*

Ministry of Higher Education and Scientific Research

University of August 20th 1955-Skikda

Faculty of Science

Department of Chemistry

# Thesis

Submitted to the Department of Chemistry

For the requirement for a Doctor Degree (LMD) in Chemistry

Specialty: Materials Chemistry

Presented by

***Settara Khaoula***

# Elaboration and characterization of Transparent Conductive Oxide (TCO) based on ZnO:Mn/Ag/ZnO:Mn Multilayers

Jury composed of:

| | | | |
|---|---|---|---|
| Chettah Abd Elhak | Full Professor | President | University of Skikda |
| Akkari Hocine | Full Professor | Supervisor | University of Batna-2 |
| Lekoui Fouaz | Senior Researcher | Co-supervisor | CDTA |
| Haddadi Sofiane | Senior Researcher | Examiner | CDTA |
| Chiha Mahdi | Full Professor | Examiner | University of Skikda |
| Naili Noura | Associated Professor | Examiner | University of Skikda |

*2024/2025*

*République Algérienne Démocratique et Populaire*

Ministère de l'enseignement supérieur et de la recherche scientifique

Université 20 Août 1955 Skikda

Faculté des Sciences

Département de Chimie

# Thèse

Soumis au Département de Chimie

Pour l'obtention du diplôme de Doctorat (LMD) en Chimie

Spécialité : Chimie des matériaux

Présenté par

***Settara Khaoula***

# Elaboration et caractérisation d'oxydes conducteurs transparents (TCO) à base de multicouches ZnO:Mn/Ag/ZnO:Mn

Devant le jury :

| | | | |
|---|---|---|---|
| Chettah Abd Elhak | Professeur | Président | Université de Skikda |
| Akkari Hocine | Professeur | Directeur de thèse | Université de Batna-2 |
| Lekoui Fouaz | MRA | Co- directeur de thèse | CDTA |
| Haddadi Sofiane | MRA | Examinateur | CDTA |
| Chiha Mahdi | Professeur | Examinateur | Université de Skikda |
| Naili Noura | MCA | Examinateur | Université de Skikda |

*2024/2025*

# Dedication

Regardless of the hurdles that lie in our way, despite the difficulties we face, craving knowledge will always push us towards the future and be our unique and only asset.

With the expression of my greatest gratitude, I dedicate this modest work to those who supported and encouraged me during these years of study:

My dear parents, who sacrificed everything for me

Thanks to you I am here, and thanks to you I will be far away...

You will always remain the first in my heart.

My siblings: Wafa, Anis, Imene and Abderraouf

My fiancé Zohir

My supervisors Pr Akkari and Dr Lekoui

All my dear friends and those I love, near and far.

# *Acknowledgement*

First of all, I thank **ALLAH**, the Almighty, for granting me the will and strength to accomplish this work.

All the work in this thesis was done at the Center for the Development of Advanced Technologies (**CDTA**). I am grateful and glad that I got the honor to work with their incredible and amazing team. For that, I want to give a special thanks to CDTA director **Dr. Mohammed Traiche**

The director of the Ionized Media & Laser Division **Dr. El-Hachemi Amara**

and all members and researchers, especially **Dr. Garoudja Elyes**, **Dr. Filali Walid**, **Dr. Hassani Salim** and **Dr. Oussalah Slimane**

I wish to express my deepest gratitude to my advisor, **Prof. Akkari Hocine**, for his support, encouragement, and valuable advice, without which I would not have been able to complete a significant part of this work and for always being a source of inspiration and pride ever since I started my master degree in materials chemistry.

I express my deep gratitude, heartfelt appreciation, and sincere thanks to my co-advisor, **Dr. Lekoui Fouaz**, a researcher at the CDTA, for all the time and effort he puts into this work. I admire his human qualities, constructive remarks, patience, and skills, which have greatly assisted me in writing this manuscript.

I would like to warmly thank and express my gratitude to the members of the jury who kindly agreed to evaluate this thesis work and attend my thesis defense:

Professor **Chettah Abd Elhak**, Doctor **Haddadi Sofiane**, Professor **Chiha Mahdi** and Doctor **Naili Noura**

I want to express my gratitude to **Pr. Halil I. AkyildizMr**, Associate Professor at Uludag University, and all the members of the **AKYILDIZ RESEARCH GROUP**, **Aymen**, **Burak** and **Sumeyye**, for welcoming me into the laboratory, supporting me, and effectively supervising my short internships.

With my deep feelings of gratitude, I would like to especially thank **my parents** who wanted so much to see me succeed and for their precious and invaluable support. I also thank my **sisters** and **brothers**, who have always supported me.

Furthermore, I must thank my dear fiance, **Benchiekh Zohir**. You have been a listener and a supporter of all my endeavors. Your partnership, steadfastness, and love sustain me.

I would also like to express my gratitude to my dearest friends and colleagues, **Amina** and **Nesrine**, for always being there to encourage me and support me.

Finally, I would like to thank all those who contributed, directly or indirectly, to the completion of this work.

# List of tables

# List of Figures

# List of abbreviations

| | |
|---|---|
| **ZnO** | *Zinc oxide* |
| **TCOs** | *Transparent conductive oxides* |
| **Ag** | *Silver* |
| **Mn** | *Manganese* |
| **VB** | *Valence band* |
| **CB** | *Conduction band* |
| **CVD** | *Chemical vapor deposition* |
| **MBE** | *Molecular beam epitaxy* |
| **DMS** | *Diluted magnetic semiconductor* |
| **SK** | *Stranski-Krastanov* |
| **LEDs** | *Light-emitting diodes* |
| **UVB** | *Ultraviolet B* |
| **UVA** | *Ultraviolet A* |
| **GHS** | *Globally harmonized system of classification and labelling of chemicals* |
| **LCDs** | *Liquid crystal displays* |
| **OLEDs** | *Organic light-emitting diodes* |
| **OMO** | *oxide/metal/oxide* |
| **SPR** | *Surface plasmon resonance* |
| **SP** | *Spray pyrolyze* |
| **UPS** | *Ultrasonic Pyrolytic Spray* |
| **EDS** | *Electrostatic Deposition Spray* |
| **CVD** | *Chemical vapor deposition* |
| **CBD** | *Chemical bath deposition* |
| **PVD** | *Physical vapour deposition* |
| **PCVD** | *Photolytic chemical vapour deposition* |
| **PECVD** | *Plasma-enhanced chemical vapour deposition* |
| **TCVD** | *Thermal chemical vapour deposition* |
| **APCVD** | *Atmospheric pressure chemical vapor deposition* |
| **LPCVD** | *Low-pressure chemical vapor deposition* |
| **UHV-CVD** | *Ultra High Vacuum chemical vapor deposition* |
| **MOCVD** | *Metal-organic chemical vapor deposition* |
| **ALD** | *Atomic layer deposition* |

| | |
|---|---|
| **ALE** | *Atomic layer epitaxy* |
| **LAD** | *Laser ablation deposition* |
| **DC** | *Direct Current* |
| **AC** | *Alternating Current* |
| **MBE** | *Molecular beam epitaxy* |
| **UHV** | *Ultra-high vacuum* |
| **XRD** | *X-ray Diffraction* |
| **SEM** | *Scanning Electron Microscope* |
| **CDTA** | *Center for Development of Advanced Technologies* |
| **GA** | *Genetic algorithms* |
| **DE** | *Differential evolution* |
| **PSO** | *Particle swarm optimization* |
| **BBO** | *Biogeography-based optimization* |
| **DA** | *Dragonfly algorithm* |
| **LVM** | *Local vibration mode* |
| **EDX** | *Energy Dispersive X-ray* |
| **FWHM** | *Full Width at Half-Maximum* |
| **RMSE** | *Root Mean Squared Error* |
| **LSPR** | *Localized Surface Plasmon Resonance* |

# Summary

# General Introduction

# General Introduction

Throughout history, minerals have been used as decorative objects, weapons, and everyday items. In the early 16th century, significant progress was made in the field of science, mostly due to the contributions of Dr. Georgius Agricola (1494-1555) [1]. Furthermore, the industrial revolution played a crucial role in driving the need for materials and their investigation, leading to increasing collaboration between the fields of physics, chemistry, and material science. Over the past few decades, there has been a significant surge in the extraction and production of minerals in various countries across the globe [2]. Algeria is a highly appealing destination for global mining investments due to its abundant reserves of minerals, including silver, gold, gypsum, lead, and zinc [3].

Minerals play a crucial role in the world's economic progress. However, their importance extends beyond just economic benefits. Minerals including zinc, cobalt, iron, and manganese, together with their oxide forms, play significant roles in physical, chemical, and catalytic processes as well as in the production of fuels, precious stones, diodes, lasers, sensors, batteries, and even as a foundation in items intended for human use [4]. Specifically, zinc oxide (ZnO) has a wide variety of applications due to its interesting properties, such as high chemical and thermal sensitivity, easy preparation, strong oxidation capacity, and thermodynamic stability compared to other materials [5]. Some research has reported the use of this oxide in textiles and sunscreens thanks to its antimicrobial capacity and resistance to UV radiation due to its compatibility with living organisms [6, 7]. For this reason, ZnO has been studied by various manufacturing methods and in its various forms (bulk, nanoparticle and thin film). ZnO is a semiconductor, a part of the transparent conductive oxides (TCOs) that are characterized by their electrical and optical properties important for electronic device applications. This type of materials depends on their specific defects, which modify their structural, surface and electrical properties [8].

Among the wide band gap oxides, doped ZnO is considered a prominent candidate for applications in optoelectronics and transparent electronics due to its gap (3.34 eV) and large exciton bond (60 meV) at room temperature (25-27 °C) [9]. For these reasons, and due to the rapid evolution of science in search of new and better physical properties in materials, which are implemented in innovative technological applications, and which can replace existing devices through the use of materials with better performance, increasingly efficient and with a smaller size, seeking to carry out the study and analysis of the performance of ZnO thin films

by studying the relationship between doping it with a metal and its properties, grown on a glass substrate using rapid thermal evaporation technique, with the aim of studying the optical and electrical properties of these thin films.

In the early 2000s, researchers investigated a new multilayered sandwich structure oxide/metal/oxide to improve the conductivity and properties of the TCOs. The key challenge was to balance the thickness of each layer to optimize both the electrical and optical properties. Studies demonstrated that incorporating an Ag layer between ZnO layers could significantly reduce sheet resistance while preserving high optical transmittance [10]. The ZnO/Ag/ZnO multilayer structure involves alternating layers of ZnO and silver (Ag) to exploit the beneficial attributes of each component. ZnO layers provide optical transparency and are conductive to form a conductive pathway, while the Ag layer, known for its superior electrical conductivity, enhances the overall conductivity of the structure without significantly impacting transparency. The Ag layer's role as a conductive interlayer between two ZnO layers capitalizes on its excellent metallic conductivity and its ability to maintain a thin layer, minimizing its impact on transparency [11].

To this end, in this thesis work, we have dedicated ourselves to the manufacture of thin multilayers of pure and doped ZnO films depending on the dopant percentage. These films were characterized structurally, optically, and electronically, and they have potential future use in photovoltaic fields. Our work is divided into 4 main chapters:

- In the first chapter, we present fundamental concepts and information about thin films, transparent conductive oxides TCOs and the materials used, giving a clear vision about the properties and applications of our films.
- In the second chapter, we explain the various deposition techniques of thin films and their characterization.
- In chapter three, we explain the deposition method and conditions we used to elaborate all of our samples along with the instruments used to study the structure, morphology, wettability, optical and electrical properties.
- Finally, the chapter four presents the results we found and detailed explanation of each of them. This chapter is divided into two parts, the first one is studying the single layer of pure and doped ZnO, while the second part is about ZnO/Ag/ZnO and Mn:ZnO/Ag/ZnO:Mn thin films.

## References

*[1] Aldrich, M. L., Leviton, A. E., & Sears, L. L. (2009). Georgius Agricola, De Animantibus Subterraneis, 1549 and 1556: A translation of a Renaissance essay in zoology and natural history. Proceedings of the California Academy of Sciences, 60(1), 89.*

*[2] Dutta, T., Kim, K. H., Uchimiya, M., Kwon, E. E., Jeon, B. H., Deep, A., & Yun, S. T. (2016). Global demand for rare earth resources and strategies for green mining. Environmental Research, 150, 182-190.*

*[3] Stambouli, A. B., Khiat, Z., Flazi, S., & Kitamura, Y. (2012). A review on the renewable energy development in Algeria: Current perspective, energy scenario and sustainability issues. Renewable and sustainable energy reviews, 16(7), 4445-4460.*

*[4] National Research Council, Division on Earth, Life Studies, Board on Earth Sciences, Committee on Earth Resources, & Committee on Critical Mineral Impacts of the US Economy. (2008). Minerals, critical minerals, and the US economy. National Academies Press.*

*[5] Theerthagiri, J., Salla, S., Senthil, R. A., Nithyadharseni, P., Madankumar, A., Arunachalam, P., ... & Kim, H. S. (2019). A review on ZnO nanostructured materials: energy, environmental and biological applications. Nanotechnology, 30(39), 392001.*

*[6] Tan, L. Y. (2018). Functionalization of cotton fabric with Zno/Pva for antibacterial textile application (Doctoral dissertation, UTAR).*

*[7] Türemen, M., Demir, A., & Gokce, Y. (2021). The synthesis and application of chitosan coated ZnO nanorods for multifunctional cotton fabrics. Materials Chemistry and Physics, 268, 124736.*

*[8] Klein, A. (2013). Transparent conducting oxides: Electronic structure–property relationship from photoelectron spectroscopy with in situ sample preparation. Journal of the American Ceramic Society, 96(2), 331-345.*

*[9] Meyer, B. K., Alves, 1. H., Hofmann, D. M., Kriegseis, W., Forster, D., Bertram, F., ... & Rodina, A. V. (2004). Bound exciton and donor–acceptor pair recombinations in ZnO. physica status solidi (b), 241(2), 231-260.*

*[10] Sahu, D. R., Lin, S. Y., & Huang, J. L. (2006). ZnO/Ag/ZnO multilayer films for the application of a very low resistance transparent electrode. Applied surface science, 252(20), 7509-7514.*

*[11] Mohamed, S. H. (2008). Effects of Ag layer and ZnO top layer thicknesses on the physical properties of ZnO/Ag/Zno multilayer system. Journal of Physics and Chemistry of Solids, 69(10), 2378-2384.*

# Objectives

## General objective

Study the structure and optoelectrical properties of Mn:ZnO/Ag/ZnO:Mn thin films deposited by rapid thermal evaporation on an ordinary glass substrate destined for photovoltaic applications.

## Specific objectives

- Deposition of pure and Mn doped ZnO layers with different Mn percentages (5%, 10%, 15% and 20%).
- Studying the effect of Mn on the structure, morphology, and optical properties of ZnO thin films.
- Deposition of ZnO/Ag/ZnO and Mn:ZnO/Ag/ZnO:Mn multilayers with different Mn percentages (5%, 10%, 15% and 20%).
- Studying the effect of Mn, multilayering and silver on the structure, morphology, optical properties, electrical properties and wettability of ZnO thin films.

# Bibliographic study

# Introduction

Materials have consistently played a crucial part in the development and evolution of cultures historically, depending on their ability to produce and modify them according to human needs [1]. Only a few centuries ago, scientists started to comprehend the relationship between the composition of materials and their properties. Since then, the process of designing and altering materials has become more precise and efficient, aiming to achieve specific characteristics that make them suitable for various applications in science and engineering [2]. In this way, research in materials has become an essential discipline to address the scientific and industrial requirements of modern society [3]. This discipline in recent decades has been highly refined thanks to the advances in science, which have allowed us to have a greater and better understanding of the structure and properties of materials [4,5].

In recent decades, materials science has emerged as a strategic study for development in all areas of engineering and applied science [6]. Materials formed into thin films occupy a primary place in the advances in materials technology, such as optoelectronics, gas detection, and health science [4]. One of the thin films that gained a huge interest in applied and elemental research is those that use zinc oxide (ZnO) because it is promising for application in several fields [7]. This chapter provides an overview and essential background information regarding this exceptional material, serving as a foundation to facilitate the comprehension of our present work.

## I.1. Semiconductors

The term "semi" is typically used to describe a range that falls between two limitations. At the same time "conductor" refers to any substance that permits the flow of electric charge when a voltage source of limited magnitude is applied to its terminals [8]. Therefore, semiconductors are materials that can behave as electrical conductors or as electrical insulators, depending mainly on the physical conditions in which they are found: temperature and pressure, the intensities of the electrical or magnetic field to which the material is subjected or the chemical composition (the level of impurities present in their structure) [9].

In insulators, the electrical conductivity is less than $10^{-10}$ $(\Omega cm)^{-1}$, which means that these materials do not have a flow of electrons, making them poor conductors such as glass, polyethylene, etc. In conductive materials, the conductivity is $10^{4}$ to $10^{9}$ $(\Omega cm)^{-1}$, which allows

electrons to have weak bonds and move freely, such as gold and silver. This makes the conductivities of semiconductors between $10^{-10}$ and $10^{4}$ $(\Omega cm)^{-1}$ [10].

Semiconductors are composed of very varied chemical elements, which come from different regions of the Periodic Table but share certain chemical traits (generally tetravalent) that give them their particular electrical properties [11]. Currently, the most used semiconductor is silicon (Si), particularly in the electronics and computing industry [12].

The increase in the production of almost perfect crystals helped study their properties and thermoelectric effects with greater precision, unlike metals. Semiconductors are produced from these almost perfect crystals, which are crystalline systems whose valence band (full of electrons) is separated from the conduction band (empty) by a forbidden band called a "band gap". One way to differentiate between a semiconductor and a metal is through its conductivity. For a metal, it increases with the elimination of impurities, while for a semiconductor, it decreases [9].

There are semiconductors at room temperature that have an appreciable electrical conductivity due to the presence of impurities in their structure [9]. When the charge carriers are negative (mostly electrons), they are called "n-type", which is known as a semiconductor with impurities. And when the charge carriers are positive (mostly holes), it is called "p-type" [13]. These two types of semiconductors have higher conductivity due to their concentration of impurities. They do not depend on temperature and are called extrinsic semiconductors [14].

In a p-type semiconductor, an electron ionizes an acceptor impurity, generating a hole in the valence band. Thus, the localized states are positioned near the upper edge of the VB [13,15]. For an n-type semiconductor, an electron travels from the donor impurity to the conduction band after ionization, where the states are located at the lower edge of this same band. In **Figure I.1**, we see the schema of the band structure for both types of semiconductors.

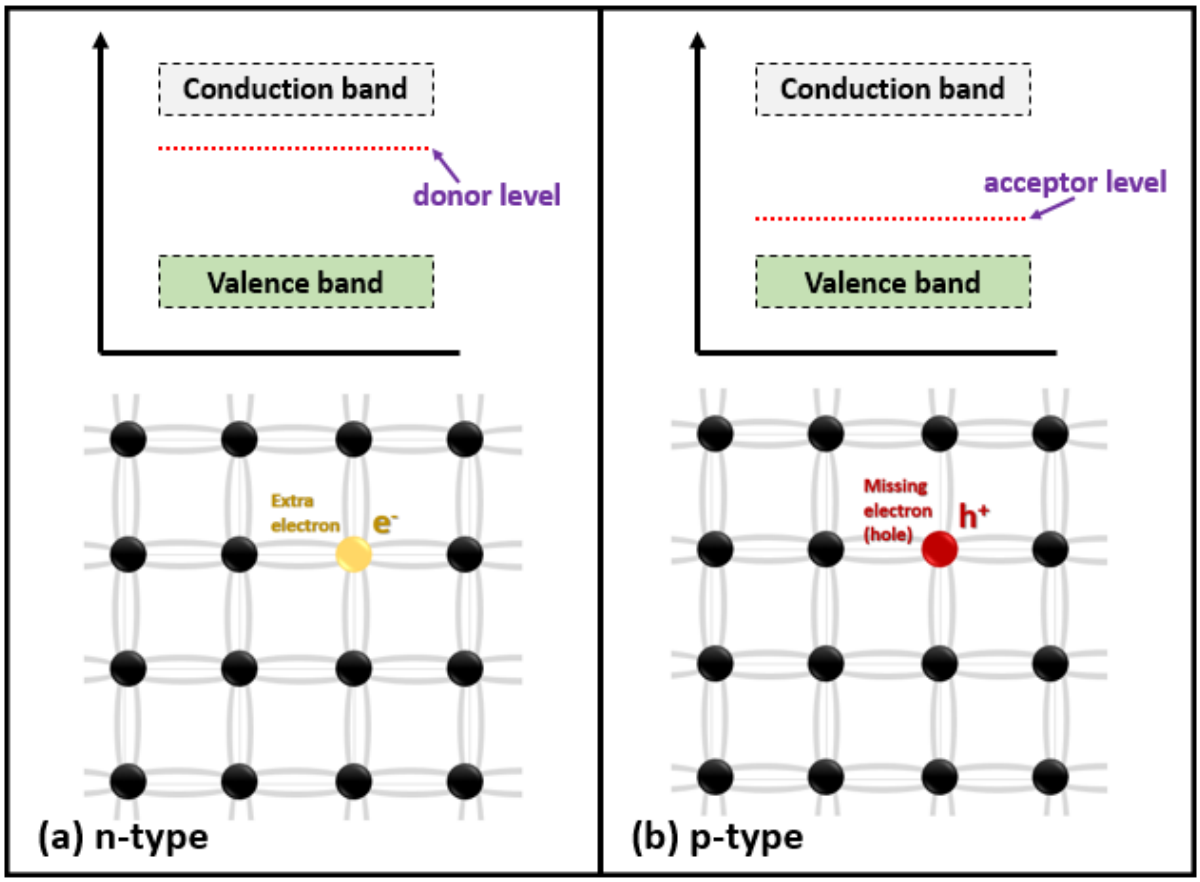


***Figure I.1*** *Schema of n-type (a) and p-type (b) semiconductor [13].*

Due to the various applications of semiconductor materials, techniques that can produce pure or doped semiconductors, which are also known as intrinsic and extrinsic semiconductors, respectively, have been needed.

- Intrinsic: It is a semiconductor without impurities or defects in its crystal lattice structure. At absolute zero Kelvin temperature (−273.15 °C), the material behaves as an insulator. However, as the temperature rises, the thermal movement causes some bonds to break. Each broken bond creates an electron-hole pair, causing the semiconductor to become a weak conductor. The energy needed to break a bond or create an electron-hole pair is referred to as the gap energy or forbidden energy gap [16, 17].
- Extrinsic: it is a semiconductor with impurities in its crystal lattice structure. These impurities contribute to the generation of charge carriers, in addition to the electron-hole pairs that are created through thermal processes [16].

## I.2. Thin films

A thin film is a very thin layer of a material, usually between nanometers and a few microns. Thin films in the photovoltaic field have been developed and implemented to reduce costs. They are formed or grown on surfaces called substrates [18, 19]. The materials that are deposited can be monocrystalline, polycrystalline, or even amorphous, with different stoichiometries [20]. The term “thin film” is defined by H. Adachi and K. Wasa as a low-dimensional material formed by condensation resulting from an individual deposit of atoms on a substrate. Another description of a thin film is expressed as a uniform deposit of material in the range of nanometer to several micrometers thick (0.1 to 300 μm) [21].

The concept of thin film has become a recurring aspect in research, especially in the area of materials science, due to its technological impact, since it makes it possible to obtain new materials as a result of synthesis from precursor substances. In turn, these new materials provide a coating with specific properties to the surface where they are applied [22]. The importance of obtaining thin films can be deduced from devices such as computers or solid-state microelectronic devices, all of them based on materials whose structure is formed by thin-film deposition. An excellent example is the manufacture of semiconductor devices, an industry totally dependent on the formation of thin-film solid-state films of a wide variety of materials obtained by a deposition process in both the gas phase and the solid, liquid or vapor phase [23].

Thin films have long been widely used in various fields, including optics, mechanics, and electronics. Background from the 18th century shows that coatings in the form of films were applied to ceramic pieces using a silver salt solution that, decomposing when heated, left a decorative silver film on the surface [24]. Currently, these films have been considerably developed for multiple purposes, among which are an aesthetic surface finish, protection against corrosion and wear in multiple products, and use in optical coatings, as a protector, thermal or electrically conductive, as well as to provide magnetic and optical (luminescent) properties for application in the manufacture of electronic devices [25, 26].

Throughout the second half of the 20th century, the development of electronics opened novel opportunities and created significant enthusiasm for thin-film technology. Later, the development of integrated semiconductors utilizing thin-film materials instead of conventional bulk materials marked a major breakthrough in device downsizing [27].

### I.3. Background on ZnO thin films

The study of ZnO has a long history, it goes back to the end of 18th century, where researchers such as W. Khalef, et al. identified ZnO as a distinct chemical substance as a glucose biosensor electrode [28]. However, in the mid-20th century, the emergence of semiconductor technology led to the transition towards thin film technology. This shift was facilitated by the development of thin film deposition techniques like sputtering, chemical vapor deposition (CVD), and molecular beam epitaxy (MBE). These advancements allowed researchers to investigate more about ZnO qualities. In the 1980s, zinc oxide thin films gain more interest for their potential to be transparent conductive oxides (TCOs). Researchers have shown the ability of ZnO thin films to be very transparent to light and have low resistance to electricity. This makes them excellent for applications in flat-panel displays and solar cells [29, 30]. This period marked the initiation of ZnO thin films as a promising material in optoelectronics, laying the foundation for additional investigation into its characteristics and uses.

During the 1990s, researchers' attention shifted towards enhancing the efficiency and stability of ZnO thin films by doping it with different metals [31-33]. Manganese (Mn) dopants were introduced to create Mn doped ZnO which exhibited ferromagnetism at room temperature, a property that was not present in pure ZnO [34]. This discovery was revolutionary, as it suggested that ZnO has the ability to act as a diluted magnetic semiconductor (DMS), that combines both magnetic and semiconductor characteristics. The research on the properties of Mn doped ZnO thin films rapidly got recognition due to their possible applications in spintronics, a field that uses the spin of electrons, in addition to their charge, for advanced electronic devices [35]. Research has concentrated on enhancing the Mn doping levels [36], deposition techniques [37-39], and annealing processes [40] in order to get specific properties. More studies explored the mechanisms that explain the observed ferromagnetism in Mn-doped ZnO. The findings revealed that the magnetic characteristics were caused by the interaction between Mn ions and the ZnO host lattice [41, 42]. During this time, theoretical models were developed to explain the observed findings, specifically focusing on the role of hole carriers in facilitating ferromagnetic interactions [43].

Advancements in synthesis techniques and material engineering have enhanced control over doping levels and film quality, hence furthering the progress in many fields [44]. Research on Mn doped ZnO thin films has recently expanded to investigate more characteristics and applications. For example, researchers have studied the addition of Mn to ZnO films for its

potential applications in gas sensors [45], data storage devices [46], and solar cells [47]. In the future, research will likely prioritize addressing current obstacles, such as obtaining uniform doping, enhancing film stability, and investigating new applications.

### I.4. Growth mechanisms of thin films

Since the beginning of the technological development associated with the fabrication of thin films, there has been interest in understanding the formation process and the development of the internal structure of the films. Thin films start to grow when atoms reach and condense on the substrate surface. A homogeneous thin film is obtained when bound atoms ("clusters") grow and then merge. The structure of the growing film depends on the initial nucleation energy and its microstructural evolution [48]. The growth of thin films involves three steps (**Figure I.2**):

*1. Nucleation* refers to the early phase of thin film formation, during which small clusters of atoms or molecules emerge on the surface of the substrate. This stage is influenced by several factors, including deposition rate, the temperature of the substrate, and the energy of the surface [49].

- Heterogeneous Nucleation: typically occurs on pre-existing surface features or impurities, which act as nucleation sites. The nucleation rate can be greatly influenced by the characteristics of the substrate and its surface roughness. For example, a substrate that is uneven or has a specific design can improve the process of nucleation by offering more surface areas for atoms to cluster together [50].
- Homogeneous nucleation: Although it is less frequent in thin film deposition, it can occur in the vapour phase, leading to the creation of nuclei without any surface help. This process is less common and typically requires higher levels of supersaturation [50].

*2. Growth:* Following nucleation, the growth of thin films involves expanding these initial nuclei into a continuous film. The growth mode is influenced by the deposition method and the interaction between deposited atoms and the substrate [49, 51].

- Volmer-Weber growth, also known as island growth, is a process where little islands of material are initially formed on the substrate and later merge together to create a continuous film. This mode is commonly observed in situations where the atoms that are deposited onto the substrate have a surface energy that is significantly higher than that of the substrate [52].

- The Frank-Van der Merwe model, also referred to as Layer-by-Layer Growth: This mode involves the formation of one atomic layer at a time. Uniform layer development is commonly observed in situations where the deposited material has a lower surface energy than the substrate [53].
- Stranski-Krastanov (SK) Growth: The SK is a hybrid process that involves both layer-by-layer and island growth. At first, the film grows in a sequential step, with multiple layers being added one after another, until islands start to develop. This mode is common in systems where there is a difference in the arrangement of atoms between the film and the substrate [54].

*3. Coalescence:* It involves the merging of individual islands or droplets, leading to the formation of a continuous film. Factors such as island size, deposition rate, and substrate temperature have an influence on the dynamics of coalescence [51].

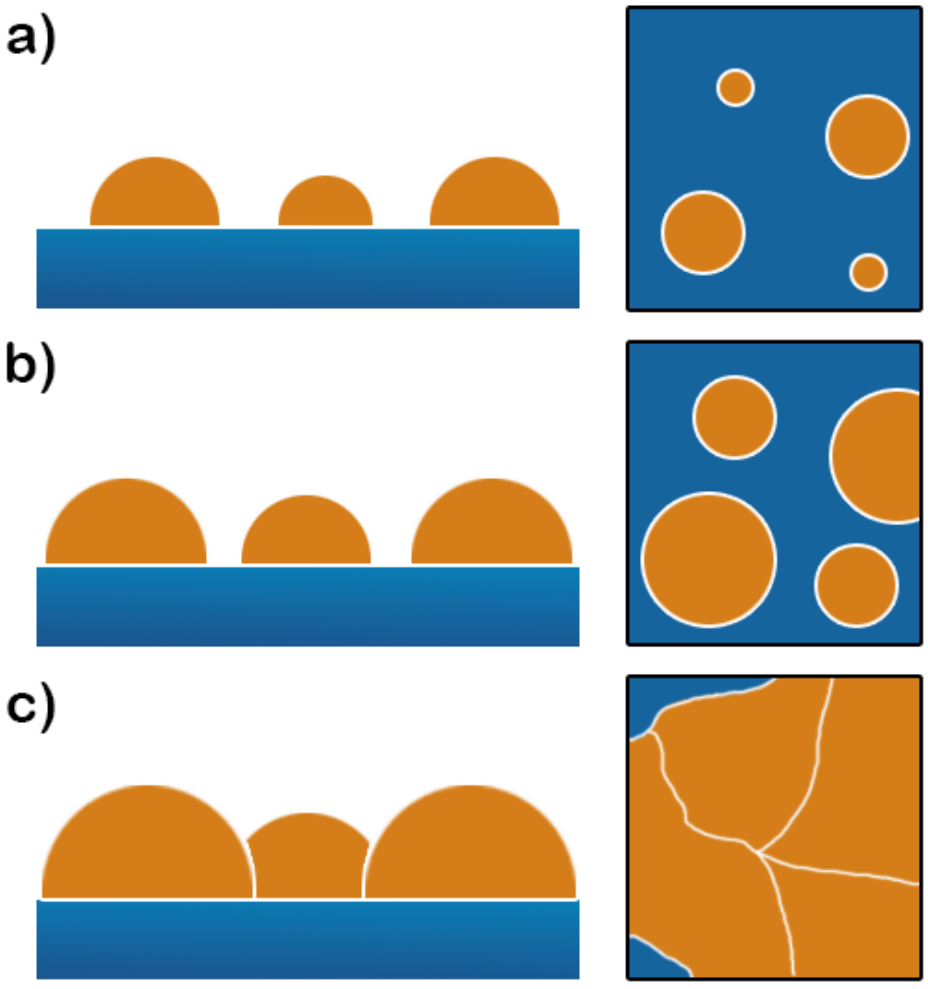


***Figure I.2.*** *Growth steps of thin films: a) Nucleation, b) Growth and c) Coalescence [50-54].*

### I.5. Zinc oxide

Zinc, a transition metal, has a valence state of +2. This allows it to combine with oxygen to create zinc oxide, thanks to the difference in electronegativity between the two elements, resulting a highly ionic bond. Zinc oxide is one of the most studied semiconductors due to its characteristic properties, such as its non-toxicity and exceptional chemical and thermal stability [55]. Zinc oxide (ZnO) is classified as an "n" type semiconductor and belongs to group II-IV. It has a band gap of approximately 3.35eV, a high melting point of around 2000ºC, and an electrical resistivity of 106 Ω/cm [56,57]. These properties make zinc oxide a material of significant interest in various industries. It finds applications in producing catalysts, electrical components, and electronic devices.

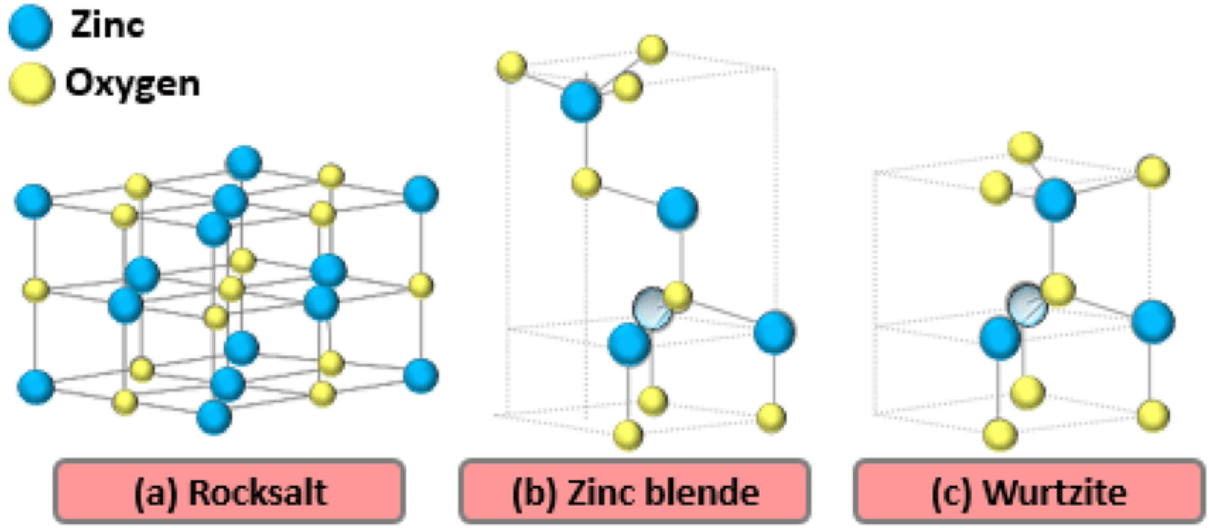


***Figure I.3.*** *The structures of ZnO: (a) Rocksalt, (b) Zinc blende and (c) Wurtzite [58].*

ZnO has three crystalline structures (**Figure I.3**): rock-salt, Zinc blende cubic, and hexagonal Wurtzite, the latter being the most thermodynamically stable and common [58]. Furthermore, Wurtzite is characterized by having two subnetworks of $Zn^{2+}$ and $O^{2-}$ perpendicular to the “c” axis; that is, it has a compact hexagonal matrix of Oxygen anions with half of the tetrahedral voids occupied by Zinc cations, where Zn is an acceptor and O is a donor.

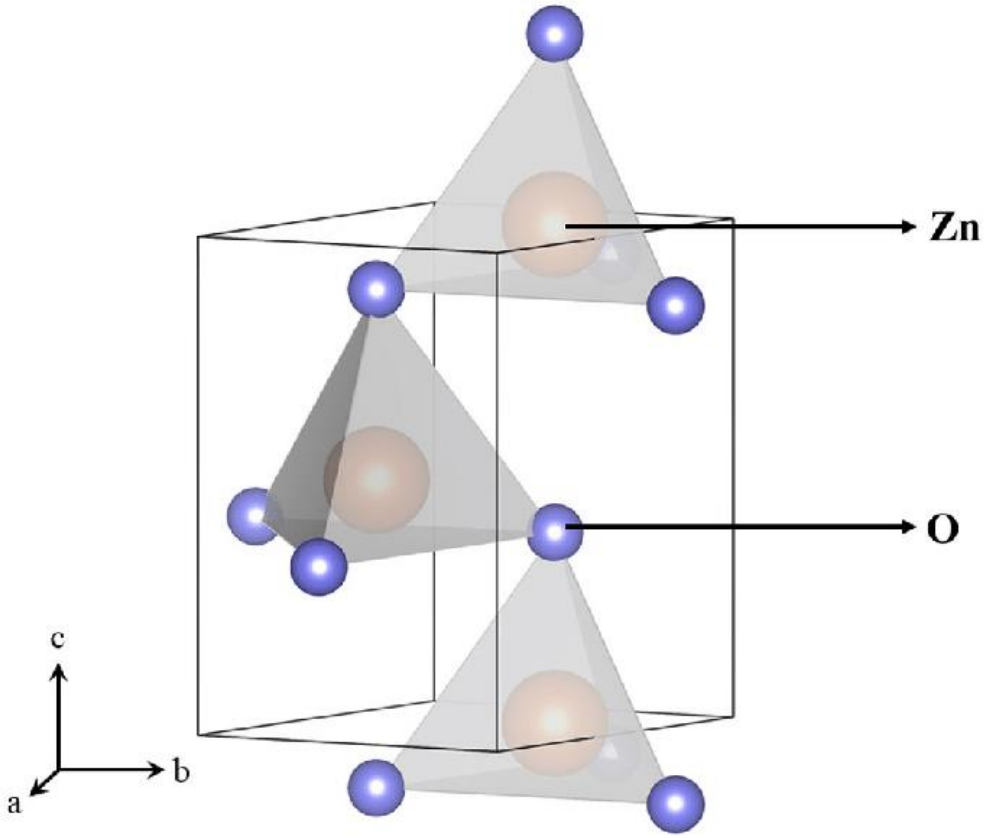


***Figure I.4.*** *Wurtzite structure of ZnO designed in Vesta [59]*

**Figure I.4** shows the structure of Wurtzite designed in the VESTA program (Visualization for Electronic and Structural Analysis), with network parameters of a = 3.25 Å and c = 5.21 Å [59], where the atoms in red and blue are Zn and O, respectively.

### I.5.1. Properties of ZnO

Zinc oxide is an inorganic compound that is relatively abundant, chemically stable, easy to prepare, and non-toxic. It is insoluble in water but soluble in dilute acids and bases [60]. Its boiling point is extremely high, 1975°C, a temperature at which it also decomposes [61]. It is a semiconductor formed by the elements of group $II^b$ ($_{30}$Zn) and group VI ($_8$O). Zinc has five stable isotopes of which the most common are zinc 64 (48.89%), zinc 66 (27.81%), and zinc 68 (18.57%) while oxygen consists almost purely of the Oxygen 16 isotope (99.76%) [62].

Zinc has an electronic configuration $(1s)^2$ $(2s)^2$ $(2p)^6$ $(3s)^2$ $(3p)^6$ $(3d)^{10}$ $(4s)^2$, while oxygen has a configuration of $(1s)^2$ $(2s)^2$ $(2p)^4$. The bonding of ZnO in its crystal lattice involves a hybridization of the electronic states, leading to four equivalent orbitals in a tetrahedral geometry. In the resulting semiconductor crystal, the s bond states constitute the valence band,

while the conduction band originates from its antibonding counterpart [59]. **Table I.1** summarize ZnO properties.

***Table I.1.*** *Properties of ZnO*

| *Chemical formula* | *ZnO* |
|---|---|
| *Molar mass* | 81.68 g/mol [63] |
| *Density* | 5.606 g/cm³ [64] |
| *Melting point* | 2248 K [65] |
| *Bandgap* | 3.35 eV (direct) [56] |
| *Exciton binding energy* | 60 meV [66] |

### I.5.1.1. Piezoelectric properties

ZnO has important piezoelectric properties, which refer to the effect described by Jacques and Pierre Curie in which when mechanical stress is applied to a material, it generates electrical energy [67]. In addition, it has a strong pyroelectric property, which is the ability of some crystalline materials to generate an external electric current in response to a change in temperature [68]. These properties are a result of its little symmetry in its wurzite crystalline form and its great electromechanical coupling.

### I.5.1.2. Optical properties

The optical properties of a semiconductor originate in the material's intrinsic and extrinsic properties. Intrinsic optical transitions, also called fundamental transitions, occur between the electrons in the conduction band (CB) and the holes in the valence band (VB), including excitonic effects caused by Coulomb interaction [69]. Extrinsic properties are related to impurities or dopants and point defects, which generally create electronic states within the bandgap and influence the absorption and emission processes. When the recombination of an electron-hole pair results in the emission of a photon, the process is called radiative recombination. A recombination that does not produce photons is called non-radiative recombination, in which energy is exchanged with the network as heat through phonon emissions [70].

### I.5.5.3. Electrical properties

ZnO has a high resistivity attributed to the incorporation of oxygen molecules between the crystalline faces obtained during the growth process, creating a potential barrier in these

areas that negatively affects the conduction process. Its conductivity is attributed to a deviation in the stoichiometry of the films due to a lack of oxygen or an excess of zinc in the crystalline lattice [57]. However, low-resistivity ZnO films have been used to manufacture solar cells as transparent conductive contacts [71]. Another property of zinc oxide is its n-type conductivity, which is caused by the formation of native defects such as oxygen vacancies and interstitial zinc. Depending on the growth method, the carrier concentration varies between 1016 and 1017 $cm^{-3}$, and the electron mobility from 130 to 205 $cm^2\ V^{-1}\ s^{-1}$ at room temperature [72].

### I.5.2. Applications

Due to the excellent physical-chemical properties, stability, abundance on earth, safety, and economical processing that ZnO presents, it has a wide range of applications, such as:

- In rubber manufacturing, ZnO activates vulcanization to make the rubber harder and more cold-resistant. Due to its thermal conductivity, it is used in car tires to prevent deformation upon contact with the asphalt [73].
- In the manufacture of concrete, where it is used to reduce the protection and processing time against water [74].
- It is also used as a white pigment for its ability to filter and protect against UVA (wavelength between 320 - 400 nm) and UVB (wavelength between 280 - 320 nm) solar radiation [75].
- As an anticorrosive coating for galvanised iron to preserve its flexibility and adhesion on surfaces [75].
- It is used as a semiconductor in light-emitting diodes (LEDs), transparent electrodes, and liquid crystals for use in electronic transparency acoustic devices and gas sensors [76]
- As an active material in thin films and the manufacture of LEDs [75].
- In the production of varistors, solar cells, and transparent conductive films [75].

### I.5.3. Doping of ZnO

To construct ZnO nanostructured devices, it is necessary to fabricate nanometric thin films of high crystalline quality with both n-type and p-type conductivity [77]. However, one of the main problems that arise when growing ZnO is its doping. This problem occurs when

doping it with an impurity to obtain a certain type of conductivity; making an n-type semiconductor is a very simple process, while it is quite complicated to achieve a p-type [78].

The stable and reproducible growth of p-type ZnO, with high conductivity and electronic mobility, is difficult to obtain due to the electric charge self-compensation effects and the low solubility of the dopants. These effects can be caused by various mechanisms, such as the low energy of the formation of oxygen vacancies ($V_o$), and interstitial zinc ($Zn_i$), which promotes the formation of these donor defects during the synthesis of ZnO, which induces a self-compensation effect of electrical charge by promoting the formation of holes through the incorporation of acceptor impurities. It is important to note that these crystalline defects cause ZnO to have n-type conductivity [79-81]

It has been reported that the structural, optical, electrical and magnetic properties of ZnO thin films are governed by the deposition parameters, the post-treatment of the sample and the chosen dopant material. This is why properly selecting doping elements is crucial to establishing the desired fundamental properties in ZnO [82]. The optical and electrical properties of ZnO films or nanowires can be enhanced by adding dopant elements from group IA, IIIA and VIIA, and IB. Some elements that stand out are Potassium (K), Sodium (Na), Lithium (Li), Aluminum (Al), Boron (B), Indium (In), Gallium (Ga), Iodine (Y), Manganese (Mn), Copper (Cu) and Silver (Ag) among others. It is known that these materials can be acceptors and would increase the gap conduction of the semiconductor.

### I.6. Manganese

Manganese is a chemical element with atomic number Z=25 and one of the transition metals of the first long period of the periodic table; It is located between chromium and iron. It has properties in common with both metals. Manganese represents the twelfth most abundant metal in the lithosphere. This metal was discovered in 1774 by the Swedish chemist Carl Wilhelm Scheele [83]. Although little known or used in its pure form, it is of great practical importance in the manufacture of steel. Pure manganese is silver in color, but it is not found in this form in nature [84]. It combines with other substances such as oxygen, sulfur, or chlorine. It is found naturally in various types of rocks such as pyrolusite ($MnO_2$), manganite ($MnO(OH)$), braunite ($3Mn_2O_3 \cdot MnSiO_3$), Pyroxmangite ($MnSiO_3$), rhodochrosite ($MnCO_3$), hübnerite ($MnWO_4$).

### I.6.1. Properties

Organoleptically, manganese is a soft element, bright silvery-white in color, with a crystalline texture and odorless, **table I.2** summarize Mn properties. It is in a solid state at room temperature and under normal pressure. It is not originally ferromagnetic, but it can become so once it has undergone different special treatments. It is one of the main elements involved in the steel manufacturing process. Manganese is a fairly reactive metal. Although it reacts slowly in its solid state, its powder reacts easily and in some cases, very vigorously. Manganese oxidizes easily in air to form a brown layer of oxide [85]. It also does so at elevated temperatures and with acids releasing hydrogen. In this respect, its behavior is very similar to its neighbor with a higher atomic number, iron. Metallic manganese is not classified as a dangerous substance in the GHS or as a dangerous good for transport.

***Table I.2.*** *Properties of Mn [86].*

| *Symbol* | *Mn* |
|---|---|
| *Atomic number* | 25 |
| *Molar mass* | 54,938 g/mol |
| *Density* | 7.43 g/cm³ |
| *Melting point* | 1245°C |
| *Ionic Radius* | 0.80 Å |
| *Atomic Radius* | 1.26 Å |
| *Covalent Radius* | 1.39 Å |
| *Atomic structure* | $[Ar]3d^5\ 4s^2$ |
| *Ionization potential* | 7.46 eV |
| *Electronegativity* | 1.5 |

### I.6.2. Applications

Due to its properties, manganese derivations or compositions have multiple applications:

- Compounds such as manganese dioxide are used as a desiccant element and catalyst for paints and varnishes [87].
- The manufacturing process of dry batteries [88].

- Manufacturing and coloring glass and ceramics since many of its compounds have intense colors. Its use has even been detected in cave paintings and glass by the Egyptians and Romans to give them color [89].
- The production of beverage cans [90].
- Increasing the octane rating of the fuel [91].

### I.7. Silver

Silver is a chemical element of internal transition, with atomic number 47 and symbol Ag, it is located in group 11 and period 5 of the Periodic Table, it can be found as a free element and as Silver Sulfide (I). Its main minerals are argyrose ($Ag_2S$), proustite (double sulfide of silver and arsenic), argyritrose (double sulfide of silver and antimony), and kerargyrite (silver chloride) [92].

#### I.7.1. Properties

Silver is a white metal that acquires a metallic shine due to polishing; It is ductile, malleable, and soft; It melts at 962 ºC and volatilizes into blue vapors at higher temperatures [93]. Silver properties are summarized in **table I.3**. It is characterized by having the highest coefficient of electrical conductivity of all metals, but due to its high price, it is not used in electrical applications. Silver does not oxidize in the air. It combines with most metalloids at elevated temperatures. Silver nanoparticles exhibit optical, electrical, and surface properties that depend on size and morphology [92].

***Table I.3.*** *Properties of Ag [92, 94-96].*

| *Symbol* | *Ag* |
|---|---|
| *Atomic number* | 47 |
| *Molar mass* | 107.8 g/mol |
| *Density* | 10.49 g/cm³ |
| *Melting point* | 962°C |
| *Ionic Radius* | 1.26 Å |
| *Atomic Radius* | 1.44 Å |
| *Atomic structure* | [Kr] $4d^{10}$ $5\ s^1$ |
| *Ionization potential* | 7.58 eV |
| *Electronegativity* | 1.9 |

### I.7.2. Applications

Silver has many applications in catalysis, transistors, biosensors, etc. Lately, it has received a lot of attention since in addition to its properties already mentioned, it also presents antimicrobial activity and is already being widely applied in the pharmaceutical, food, textile, and wastewater treatment industries [97, 98].

## I.8. Transparent conductive oxides

Transparent conductive oxides (TCOs) are materials that combine excellent electrical conductivity and high optical transparency within the visible range of light. These components serve a vital role in modern electronic and optoelectronic devices, such as flat-panel displays, touchscreens, and solar cells. TCOs can conduct electric current while also permitting the transmission of visible light, which is advantageous in applications that necessitate both electrical and optical capabilities [99].

TCOs are composed of a non-metallic part, oxygen, which in combination with a metal or a combination of metals makes up a semiconductor with different optoelectronic characteristics. The high electron concentration of TCOs ($10^{19}$ $cm^{-3}$) originates from oxygen vacancies or interstitial atoms in the compound lattice, which act as electron donors. However, the stability of intrinsic TCOs (i.e. without additional doping) can be compromised at high temperatures, consequently affecting the electrical conductivity [100].

In order to increase the electrical conductivity and add stability against temperature effects, TCOs can be modified by doping with metals, metalloids or oxides: aluminium, manganese, zinc oxide, tin (ZnO:Al, ZnO:Mn and $In_2O_3$:ZnO, $In_2O_3$:Sn). Metals can be part of the semiconductor or can be dopants; Another option for doping has been the synthesis of ternary compounds ($Zn_2SnO_4$, $ZnSnO_3$ among others) or modification of the film's growing conditions. Their optical transparency is due to the wide band gap they have, greater than 2.5 eV, which allows visible light to pass through while preventing the passage of infrared and ultraviolet radiation [99-101]. The main materials that have been used in TCOs are indium oxide ($In_2O_3$), tin oxide ($SnO_2$), and zinc oxide (ZnO), however, there is a wide range of TCOs. Some conductive oxides, their optical and electrical properties and typical dopants are shown in **Table I.4**.

***Table I.4.*** *Electrical and optical properties of the thin layer of transparent conductors, band gap Eg, transmittance T and conductivity σ.*

| *TCOs* | *Eg (eV)* | *T (%)* | *σ (Ω$^{-1}$.cm$^{-1}$)* | *Dopants* |
|---|---|---|---|---|
| *ZnO* | 3.2-3.3 | 80-90 | ≤$10^4$ | Al, Ga, B, Ti, F, Mn, Cu |
| *$ZnSnO_3$* | ~3.5 | 80 | $10^2$ | F, Cr, Li, Ta |
| *$Zn_2In_2O_5$* | 2.9 | 80 | $2.5 \times 10^3$ | Sn |
| *$MgIn_2O_4$* | 3.4 | 80 | $10^2$ | Li |
| *CdO* | 2.2-2.6 | 60-80 | ≤20 | In, Sn |
| *$SnO_2$* | 3.9-4.3 | 80-90 | ≤$10^3$ | Sb, F, As, Ta |
| *$In_2O_3$* | 3.55-3.75 | 80-90 | ≤$10^4$ | Sn, Mo, F, Zr, Te, Ge, W |
| *NiO* | 3.6-4 | 40-80 | ≤10 | Mg, Li, Cu, La, Al, Cd |
| *$CuGaO_2$* | 3.6-4.3 | 70-85 | $6 \times 10^{-2}$ | Mg, Zn, Fe |
| *$CuAlO_2$* | 3.5 | 70-80 | 0.3 | Ca, Cr, Mg, Zn, Fe |

In general, TCOs used as transparent electrodes are grown as polycrystalline or amorphous thin films and, in some cases, as epitaxially grown single crystals. In any of their three growth forms, these TCO films should exhibit a conductivity in the order of $10^3$ $\Omega^{-1}$.cm$^{-1}$ or higher and an average transmittance in the visible range of 80 % or higher. To work as a thin film TCO, it needs to have a forbidden gap above 3 eV and an electron concentration of about $10^{19}$ electrons/cm$^3$. This means that it is a degenerate n-type or p-type semiconductor [102].

The TCO films used as electrodes are made up of binary systems, because the process of growing a compound with these characteristics allows a greater degree of control of the chemical composition, compared to a tertiary or multicomponent compound. TCOs have many applications, we could site:

1) Flat-panel displays, such as liquid crystal displays (LCDs) and organic light-emitting diodes (OLEDs), heavily depend on TCOs for their electrode layers that allow for transparency. The electrodes play a crucial role in the functioning of displays by enabling the passage of electric current while preserving optical transparency [103].
2) Touchscreen technology, including both capacitive and resistive touchscreens, relies on TCOs as transparent conductive layers that provide touch detection and input. [105].

3) Photovoltaic devices: Thin-film solar cells and organic photovoltaics utilize TCOs as electrodes that are capable of collecting and transporting electrical charges produced by light. [105].
4) Energy-Efficient Coatings: TCOs are used in coatings for building materials and vehicles to enhance energy efficiency. TCO-coated surfaces can effectively regulate the transmission of infrared radiation, leading to decreased expenses for heating and cooling [103].
5) Sensors and Photodetectors: TCOs are also used in various types of sensors and photodetectors due to their sensitivity and ability to operate in different environmental conditions [106].
6) Smart Windows: TCOs are incorporated into smart windows, enabling them to change their optical characteristics when exposed to external factors like temperature or electric fields. These windows have the ability to alternate between being transparent and opaque, allowing for the control of light and heat. This feature helps to conserve energy and enhance comfort [107].

### I.9. Oxide/Metal/Oxide

An oxide/metal/oxide (OMO) multilayer is a layered structure mainly made up of alternating oxide and metal layers stacked in a sandwich-like configuration. The structure levels of complexity can vary, with various layers of oxides and metals stacked to achieve specific qualities [108].

- *Oxide Layers:* The oxide layers present in an OMO multilayer are typically transparent and can exhibit either semiconducting or insulating properties. ZnO is commonly chosen because it has outstanding optical transparency and electrical conductivity characteristics. The thickness of these layers is critical since it directly affects the optical and electrical characteristics of the multilayer [109].
- *Metal Layer:* The metal layer, often made of silver (Ag) or gold (Au), has high electrical conductivity and plays a crucial role in the surface plasmon resonance (SPR) phenomena. The thickness and quality of the metal layer are crucial factors in maximizing the performance of the multilayer in different applications [109].

## Conclusion

This chapter provides essential and fundamental information on the materials used to produce the desired TCO thin films, which include zinc oxide, silver and manganese. The structure, properties, and applications of those materials were provided. It also gives a bibliographic study on thin films, TCOs and Oxide/Metal/Oxide systems and various terms that are necessary to understand this work.

## References

*[1] Habermas, J. (1975). Towards a reconstruction of historical materialism. Theory and Society, 2(3), 287-300.*

*[2] Rankin, W. J. (2011). Minerals, metals and sustainability: meeting future material needs. CSIRO publishing.*

*[3] Callister Jr, W. D., & Rethwisch, D. G. (2020). Materials science and engineering: an introduction. John wiley & sons.*

*[4] Raghavan, V. (2015). Physical metallurgy: principles and practice. PHI Learning Pvt. Ltd..*

*[5] Peter, Y. U., & Cardona, M. (2010). Fundamentals of semiconductors: physics and materials properties. Springer Science & Business Media.*

*[6] Callister Jr, W. D., & Rethwisch, D. G. (2020). Materials science and engineering: an introduction. John wiley & sons.*

*[7] Özgür, Ü., Alivov, Y. I., Liu, C., Teke, A., Reshchikov, M. A., Doğan, S., ... & Morkoç, A. H. (2005). A comprehensive review of ZnO materials and devices. Journal of applied physics, 98(4).*

*[8] Boylestad, R. L., & Nashelsky, L. (2002). Electronic devices and circuit theory. Pearson Educación.*

*[9] Sze, S. M., & Ng, K. K. (2006). pn Junctions. Physics of semiconductor devices, 2, 80-89.*

*[10] Hummel, R. E., & Hummel, R. E. (1998). Electrical properties of materials. Understanding Materials Science: History· Properties· Applications, 180-216.*

*[11] Madelung, O. (2004). Semiconductors: data handbook. Springer Science & Business Media.*

*[12] Rojas, J. P., Torres Sevilla, G. A., Ghoneim, M. T., Inayat, S. B., Ahmed, S. M., Hussain, A. M., & Hussain, M. M. (2014). Transformational silicon electronics. ACS nano, 8(2), 1468-1474.*

*[13] Zhang, C., Zhang, J., Ma, X., & Feng, Q. (2021). Semiconductor photovoltaic cells. Springer.*

*[14] Mott, N. (2004). Metal-insulator transitions. CRC Press.*

*[15] Cao, Y. C. (2011). Impurities enhance semiconductor nanocrystal performance. Science, 332(6025), 48-49.*

*[16] Balkan, N., Erol, A., Balkan, N., & Erol, A. (2021). Intrinsic and Extrinsic Semiconductors. Semiconductors for Optoelectronics: Basics and Applications, 37-78.*

*[17] Rahman, M. A. (2014). A review on semiconductors including applications and temperature effects in semiconductors. American Scientific Research Journal for Engineering, Technology, and Sciences (ASRJETS), 7(1), 50-70.*

*[18] Vook, R. W. (1982). Structure and growth of thin films. International Metals Reviews, 27(1), 209-245.*

*[19] Goswami, A. (1996). Thin film fundamentals. New age international.*

*[20] Ohring, M. (2002). Materials science of thin films: depositon and structure. Academic press.*

*[21] Adachi, H., & Wasa, K. (2012). Thin films and nanomaterials. Handbook of Sputter Deposition Technology: Fundamentals and Applications for Functional Thin Films, Nano-Materials and MEMS:, 3-39.*

*[22] Alique, D. (2018). Processing and characterization of coating and thin film materials. Advanced ceramic and metallic coating and thin film materials for energy and environmental applications, 27-72.*

*[23] Kim, H. (2003). Atomic layer deposition of metal and nitride thin films: Current research efforts and applications for semiconductor device processing. Journal of Vacuum Science & Technology B: Microelectronics and Nanometer Structures Processing, Measurement, and Phenomena, 21(6), 2231-2261.*

*[24] White, E., Slenski, G., Marchese, M., Dobbs, B., & Ziegenhagen, J. (1719). AVIONIC CORROSION: CASE HISTORIES. NA CitA1089 CP, 4, 502.*

*[25] Sharma, S., Sudhakara, P., Omran, A. A. B., Singh, J., & Ilyas, R. A. (2021). Recent trends and developments in conducting polymer nanocomposites for multifunctional applications. Polymers, 13(17), 2898.*

*[26] Acosta, E. (2021). Thin films/properties and applications. In Thin Films. IntechOpen.*

*[27] Haertling, G. H. (1992). Recent developments in bulk and thin film PLZT materials and devices. Ferroelectrics, 131(1), 1-12.*

*[28] Khalef, W. K., Aljubour, A. A., & Faisal, A. D. (1795). Fabrication of Glucose biosensor electrode based on the CuO/ZnO nanostructures. In Journal of Physics: Conference Series (Vol. 2021, p. 012038).*

*[29] Webb, J. B., Williams, D. F., & Buchanan, M. (1981). Transparent and highly conductive films of ZnO prepared by rf reactive magnetron sputtering. Applied Physics Letters, 39(8), 640-642.*

*[30] Chopra, K. L. (1983, January). TRANSPARENT CONDUCTING OXIDE FILMS FOR SOLAR CELLS. In Extended Abstracts (Vol. 1983, No. 1, p. 360). Electrochemical Society.*

*[31] Jimenez-Gonzalez, A. E., Urueta, J. A. S., & Suarez-Parra, R. (1998). Optical and electrical characteristics of aluminum-doped ZnO thin films prepared by solgel technique. Journal of crystal growth, 192(3-4), 430-438.*

*[32] Sanchez-Juarez, A., Tiburcio-Silver, A., Ortiz, A., Zironi, E. P., & Rickards, J. (1998). Electrical and optical properties of fluorine-doped ZnO thin films prepared by spray pyrolysis. Thin Solid Films, 333(1-2), 196-202.*

*[33] Joseph, M., Tabata, H., & Kawai, T. (1999). Ferroelectric behavior of Li-doped ZnO thin films on Si (100) by pulsed laser deposition. Applied physics letters, 74(17), 2534-2536.*

*[34] Fukumura, T., Jin, Z., Ohtomo, A., Koinuma, H., & Kawasaki, M. (1999). An oxide-diluted magnetic semiconductor: Mn-doped ZnO. Applied physics letters, 75(21), 3366-3368.*

*[35] Sharma, P., Gupta, A., Owens, F. J., Inoue, A., & Rao, K. V. (2004). Room temperature spintronic material—Mn-doped ZnO revisited. Journal of Magnetism and Magnetic materials, 282, 115-121.*

*[36] Viswanatha, R., Sapra, S., Sen Gupta, S., Satpati, B., Satyam, P. V., Dev, B. N., & Sarma, D. D. (2004). Synthesis and characterization of Mn-doped ZnO nanocrystals. The Journal of Physical Chemistry B, 108(20), 6303-6310.*

*[37] Kim, Y. M., Yoon, M., Park, I. W., Park, Y. J., & Lyou, J. H. (2004). Synthesis and magnetic properties of Zn1− xMnxO films prepared by the sol–gel method. Solid State Communications, 129(3), 175-178.*

*[38] Liu, C., Yun, F., Xiao, B., Cho, S. J., Moon, Y. T., Morkoç, H., ... & Walukiewicz, W. (2005). Structural analysis of ferromagnetic Mn-doped ZnO thin films deposited by radio frequency magnetron sputtering. Journal of applied physics, 97(12).*

*[39] Lokhande, C. D., Ennaoui, A., Patil, P. S., Giersig, M., Muller, M., Diesner, K., & Tributsch, H. (1998). Process and characterisation of chemical bath deposited manganese sulphide (MnS) thin films. Thin solid films, 330(2), 70-75.*

*[40] Zhang, J., Skomski, R., & Sellmyer, D. J. (2005). Sample preparation and annealing effects on the ferromagnetism in Mn-doped ZnO. Journal of Applied Physics, 97(10).*

*[41] Hong, N. H., Brizé, V., & Sakai, J. (2005). Mn-doped ZnO and (Mn, Cu)-doped ZnO thin films: Does the Cu doping indeed play a key role in tuning the ferromagnetism? Applied Physics Letters, 86(8).*

*[42] Theodoropoulou, N. A., Hebard, A. F., Norton, D. P., Budai, J. D., Boatner, L. A., Lee, J. S., ... & Wilson, R. G. (2003). Ferromagnetism in Co-and Mn-doped ZnO. Solid-State Electronics, 47(12), 2231-2235.*

*[43] Dietl, T. (2002). Ferromagnetic semiconductors. Semiconductor Science and Technology, 17(4), 377.*

*[44] Karmakar, R., Neogi, S. K., Banerjee, A., & Bandyopadhyay, S. (2012). Structural; morphological; optical and magnetic properties of Mn doped ferromagnetic ZnO thin film. Applied surface science, 263, 671-677.*

*[45] Sivalingam, D., Gopalakrishnan, J. B., & Rayappan, J. B. B. (2012). Structural, morphological, electrical and vapour sensing properties of Mn doped nanostructured ZnO thin films. Sensors and Actuators B: Chemical, 166, 624-631.*

*[46] Rana, A., Malik, R., Rana, M., Kaushik, D., Khanna, S. P., Srivastava, R., & Suman, C. K. (2024). Studies of optoelectrical properties of Mn-doped ZnO nanostructure for supercapacitor and photodetector applications. Journal of Alloys and Compounds, 997, 174931.*

*[47] Amjad, M., Khan, M. I., Alwadai, N., Irfan, M., Albalawi, H., Almuqrin, A. H., ... & Iqbal, M. (2022). Photovoltaic properties of ZnO films Co-doped with Mn and La to enhance solar cell efficiency. Nanomaterials, 12(7), 1057.*

*[48] Greene, J. E. (2010). Thin film nucleation, growth, and microstructural evolution: an atomic scale view. In Handbook of deposition technologies for films and coatings (pp. 554-620). William Andrew Publishing.*

*[49] Greene, J. E. (2010). Thin film nucleation, growth, and microstructural evolution: an atomic scale view. In Handbook of deposition technologies for films and coatings (pp. 554-620). William Andrew Publishing.*

*[50] Ruckenstein, E., Berim, G. O., & Narsimhan, G. (2015). A novel approach to the theory of homogeneous and heterogeneous nucleation. Advances in Colloid and Interface Science, 215, 13-27.*

*[51] Ratsch, C., & Venables, J. A. (2003). Nucleation theory and the early stages of thin film growth. Journal of Vacuum Science & Technology A: Vacuum, Surfaces, and Films, 21(5), S96-S109.*

*[52] Fornari, C. I., Fornari, G., Rappl, P. H., Abramof, E., & Travelho, J. D. S. (2018). Monte Carlo simulation of epitaxial growth. Epitaxy; Zhong, M., Ed.; BoD–Books on Demand: Norderstedt, Germany, 113.*

*[53] Van Der Merwe, J. H. (1993). Theoretical considerations in growing uniform epilayers. Interface Science, 1, 77-86.*

*[54] Venäläinen, O., Heiniö, J., & Kaski, K. (1991). Stranski-Krastanov growth of thin film: Monte Carlo simulation. Physica Scripta, 1991(T38), 66.*

*[55] Klingshirn, C. F., Waag, A., Hoffmann, A., & Geurts, J. (2010). Zinc oxide: from fundamental properties towards novel applications.*

*[56] Benhaliliba, M. (2022). A rectifying Al/ZnO/pSi/Al heterojunction as a photodiode. Micro and Nanostructures, 163, 107140.*

*[57] Aghamalyan, N. R., Goulanian, E. K., Hovsepyan, R. K., Vardanyan, E. S., & Zerrouk, A. F. (2003). Effect of lithium impurity on the opto-electrical properties of zinc oxide films. physica status solidi (a), 199(3), 425-430.*

*[58] Rahman, A., Harunsani, M. H., Tan, A. L., & Khan, M. M. (2021). Zinc oxide and zinc oxide-based nanostructures: biogenic and phytogenic synthesis, properties and applications. Bioprocess and Biosystems Engineering, 44(7), 1333-1372.*

*[59] Prasad, R., & Bhame, S. D. (2020). Review on texturization effects in thermoelectric oxides. Materials for Renewable and Sustainable Energy, 9(1), 3.*

*[60] Moezzi, A., McDonagh, A. M., & Cortie, M. B. (2012). Zinc oxide particles: Synthesis, properties and applications. Chemical engineering journal, 185, 1-22.*

*[61] Polarz, S., Roy, A., Merz, M., Halm, S., Schröder, D., Schneider, L., ... & Driess, M. (2005). Chemical vapor synthesis of size-selected zinc oxide nanoparticles. Small, 1(5), 540-552.*

*[62] Klingshirn, C. F., Waag, A., Hoffmann, A., & Geurts, J. (2010). Zinc oxide: from fundamental properties towards novel applications.*

*[63] Aruja, T. C., Sharma, R., Dhiman, V., Chand, S., & Kondal, N. (2022). ZnO based nanoadsorbents for purification of lead contaminated water. Materials Today: Proceedings.*

*[64] Anwar, M., Kayani, Z. N., Hassan, A., Sagheer, R., Riaz, S., & Naseem, S. (2022). Analysis of the Nd dopant on optical, dielectric and biological properties of ZnO nanostructures. Journal of the Mechanical Behavior of Biomedical Materials, 126, 105016.*

*[65] Wang, F., Wu, J., Xia, C., Hu, C., Hu, C., Zhou, P., ... & Liu, X. (2014). Thermodynamic and elastic properties of hexagonal ZnO under high temperature. Journal of alloys and compounds, 597, 50-57.*

*[66] Sun, H. D., Makino, T., Segawa, Y., Kawasaki, M., Ohtomo, A., Tamura, K., & Koinuma, H. (2002). Enhancement of exciton binding energies in ZnO/ZnMgO multiquantum wells. Journal of applied physics, 91(4), 1993-1997.*

*[67] Pandey, R. K., Dutta, J., Brahma, S., Rao, B., & Liu, C. P. (2021). Review on ZnO-based piezotronics and piezoelectric nanogenerators: Aspects of piezopotential and screening effect. Journal of Physics: Materials, 4(4), 044011.*

*[68] Zhang, D., Wu, H., Bowen, C. R., & Yang, Y. (2021). Recent advances in pyroelectric materials and applications. Small, 17(51), 2103960.*

*[69] Pankove, J. I. (1975). Optical processes in semiconductors. Courier Corporation.*

*[70] Ellmer, K., & Bikowski, A. (2016). Intrinsic and extrinsic doping of ZnO and ZnO alloys. Journal of Physics D: Applied Physics, 49(41), 413002.*

*[71] Kim, D., Kim, H., Jang, K., Park, S., Pillai, K., & Yi, J. (2011). Electrical and optical properties of low pressure chemical vapor deposited Al-doped ZnO transparent conductive oxide for thin film solar cell. Journal of the Electrochemical Society, 158(4), D191.*

*[72] Bang, S., Lee, S., Park, J., Park, S., Jeong, W., & Jeon, H. (2009). Investigation of the effects of interface carrier concentration on ZnO thin film transistors fabricated by atomic layer deposition. Journal of Physics D: Applied Physics, 42(23), 235102.*

*[73] Javadi, S. M. (2020). Applications of ZnO and MgO nanoparticles in reducing zinc pollution level in rubber manufacturing processes: a review. Current Biochemical Engineering, 6(2), 103-107.*

*[74] Nayak, C. B., Taware, P. P., Jagadale, U. T., Jadhav, N. A., & Morkhade, S. G. (2022). Effect of SiO2 and ZnO nano-composites on mechanical and chemical properties of modified concrete. Iranian Journal of Science and Technology, Transactions of Civil Engineering, 46(2), 1237-1247.*

*[75] Wang, Z. L. (2004). Nanostructures of zinc oxide. Materials today, 7(6), 26-33.*

*[76] Rahman, F. (2019). Zinc oxide light-emitting diodes: a review. Optical Engineering, 58(1), 010901-010901.*

*[77] Thangavel, R., & Chang, Y. C. (2012). Investigations on structural, optical and electrical properties of p-type ZnO nanorods using hydrothermal method. Thin solid films, 520(7), 2589-2593.*

*[78] Klingshirn, C. (2007). ZnO: From basics towards applications. physica status solidi (b), 244(9), 3027-3073.*

*[79] Al-Hardan, N. H., Jalar, A., Hamid, M. A., Keng, L. K., Ahmed, N. M., & Shamsudin, R. (2014). A wide-band UV photodiode based on n-ZnO/p-Si heterojunctions. Sensors and Actuators A: Physical, 207, 61-66.*

*[80] Balakrishnan, L., Gowrishankar, S., Elanchezhiyan, J., & Gopalakrishnan, N. (2011). Influence of Al concentration on electrical, structural and optical properties of Al–As codoped p-ZnO thin films. Physica B: Condensed Matter, 406(23), 4447-4452.*

*[81] Thangavel, R., & Chang, Y. C. (2012). Investigations on structural, optical and electrical properties of p-type ZnO nanorods using hydrothermal method. Thin solid films, 520(7), 2589-2593.*

*[82] Tarwal, N. L., & Patil, P. S. (2011). Enhanced photoelectrochemical performance of Ag–ZnO thin films synthesized by spray pyrolysis technique. Electrochimica Acta, 56(18), 6510-6516.*

*[83] Lennartson, A., & Lennartson, A. (2017). The chemical works of carl wilhelm scheele (pp. 19-103). Springer International Publishing.*

*[84] Boskovic, C. (2019). Element 25–Manganese. Australian Journal of Chemistry, 72(6), 407-410.*

*[85] Hammond, C. R. (2000). The elements. Handbook of chemistry and physics, 81.*

*[86] Sarbas, B. (2013). Mn Manganese: Natural Occurrence. Minerals (Native metal, solid solution, silicide, and carbide. Sulfides and related compounds. Halogenides and oxyhalogenides. Oxides of type MO). Springer Science & Business Media.*

*[87] Hage, R., De Boer, J. W., & Maaijen, K. (2016). Manganese and iron catalysts in alkyd paints and coatings. Inorganics, 4(2), 11.*

*[88] Bader, M., Dietz, M. C., Ihrig, A., & Triebig, G. (1999). Biomonitoring of manganese in blood, urine and axillary hair following low-dose exposure during the manufacture of dry*

*cell batteries. International archives of occupational and environmental health, 72, 521-527.*

*[89] Siddall, R. (2018). Mineral pigments in archaeology: their analysis and the range of available materials. Minerals, 8(5), 201.*

*[90] Hagelstein, K. (2009). Globally sustainable manganese metal production and use. Journal of environmental management, 90(12), 3736-3740.*

*[91] Kaiser, J. (2003). Manganese: a high-octane dispute.*

*[92] Stwertka, A. (2002). A Guide to the Elements. Oxford University Press.*

*[93] Sofie, S. W., Gannon, P., & Gorokhovsky, V. (2009). Silver–chromium oxide interactions in SOFC environments. Journal of Power Sources, 191(2), 465-472.*

*[94] Rathjen, A., Zimmermann, J., Haverkamp, V., & Krüger, K. (2015, January). Adhesion and Electrical Properties of Low Temperature Processed Ag-PMMA-Films in Inkjet Printing. In NIP & Digital Fabrication Conference (Vol. 31, pp. 452-456). Society for Imaging Science and Technology.*

*[95] Pluym, T. C., Powell, Q. H., Gurav, A. S., Ward, T. L., Kodas, T. T., Wang, L. M., & Glicksman, H. D. (1993). Solid silver particle production by spray pyrolysis. Journal of aerosol science, 24(3), 383-392.*

*[96] Rahm, M., Zeng, T., & Hoffmann, R. (2018). Electronegativity seen as the ground-state average valence electron binding energy. Journal of the American Chemical Society, 141(1), 342-351.*

*[97] Sharma, R. K., Yadav, S., Dutta, S., Kale, H. B., Warkad, I. R., Zbořil, R., ... & Gawande, M. B. (2021). Silver nanomaterials: synthesis and (electro/photo) catalytic applications. Chemical Society Reviews, 50(20), 11293-11380.*

*[98] Gao, T., Yang, D., Ning, L., Lei, L., Ye, Z., & Li, G. (2014). Ultrafine and well dispersed silver nanocrystals on 2D nanosheets: synthesis and application as a multifunctional material for electrochemical catalysis and biosensing. Nanoscale, 6(24), 14828-14835.*

*[100] Delahoy, A. E., & Guo, S. (2011). Transparent conducting oxides for photovoltaics. Handbook of Photovoltaic Science and Engineering, 32, 716-796.*

*[101] Afre, R. A., Sharma, N., Sharon, M., & Sharon, M. (2018). Transparent conducting oxide films for various applications: A review. Reviews on advanced materials science, 53(1), 79-89.*

*[102] Mallick, A., & Basak, D. (2018). Revisiting the electrical and optical transmission properties of co-doped ZnO thin films as n-type TCOs. Progress in Materials Science, 96, 86-110.*

*[103] Shigesato, Y. (2010). In Based TCOs. In Handbook of transparent conductors (pp. 149-169). Boston, MA: Springer US.*

*[104] Blake, J., & Paynton, R. (2011). Transparent Film and Substrate Technology for Touch Screens and Flexible-Display Applications. Information Display, 27(9), 34-38.*

*[105] Fortunato, E., Ginley, D., Hosono, H., & Paine, D. C. (2007). Transparent conducting oxides for photovoltaics. MRS bulletin, 32(3), 242-247.*

*[106] Yun, J. H., Kumar, M. D., Park, Y. C., Kim, H. S., & Kim, J. (2015). High performing ITO/Ge heterojunction photodetector for broad wavelength detection. Journal of Materials Science: Materials in Electronics, 26, 6099-6106.*

*[107] Cui, H. N. (2005). Preparation and characterization of optical multilayered coatings for smart windows applications.*

*[108] Dalapati, G. K., Sharma, H., Guchhait, A., Chakrabarty, N., Bamola, P., Liu, Q., ... & Sharma, M. (2021). Tin oxide for optoelectronic, photovoltaic and energy storage devices: a review. Journal of materials chemistry A, 9(31), 16621-16684.*

*[109] Lim, D. C., Jeong, J. H., Hong, K., Nho, S., Lee, J. Y., Hoang, Q. V., ... & Cho, S. (2018). Semi-transparent plastic solar cell based on oxide-metal-oxide multilayer electrodes. Progress in Photovoltaics: Research and Applications, 26(3), 188-195.*

# Deposition techniques
# and
# Characterization methods

# Introduction

This chapter is devoted to deposition methods in the field of thin films and the characterization techniques used for the study of the structure, morphology and properties of the films.

## II.1. Deposition techniques

ZnO thin films can be manufactured using different methods, depending on the application for which they are destined. These methods can be divided between wet deposition and dry deposition to modify their physicochemical properties.

### II.1.1. Wet deposition

#### II.1.1.1. Electrodeposition

It is a technique for coating and covering substrates quickly and at low costs. It is used to coat large surfaces and has the possibility of changing the substrate properties with a metallic coating. It is possible to deposit a layer of metal on a chosen substrate. The fundamental principle that governs this phenomenon is the electrolysis of a material. In these systems, the processes and factors that affect charge transport are evaluated; this is done through an interface between chemical phases, for example, between an electronic conductor (electrode) and an ionic conductor (electrolyte) [1]. This deposition involves a reduction process, that is, a decrease in the oxidation state (gain of electrons) and a deposition of the metal on the conductive surface. In the deposition, two processes take place that take place at the electrodes; one of them is based on the electrons being transferred through the metal-solution interface in which a transfer of electrons occurs that causes the oxidation or reduction of the compound [2], as shown in **Figure II.1**.

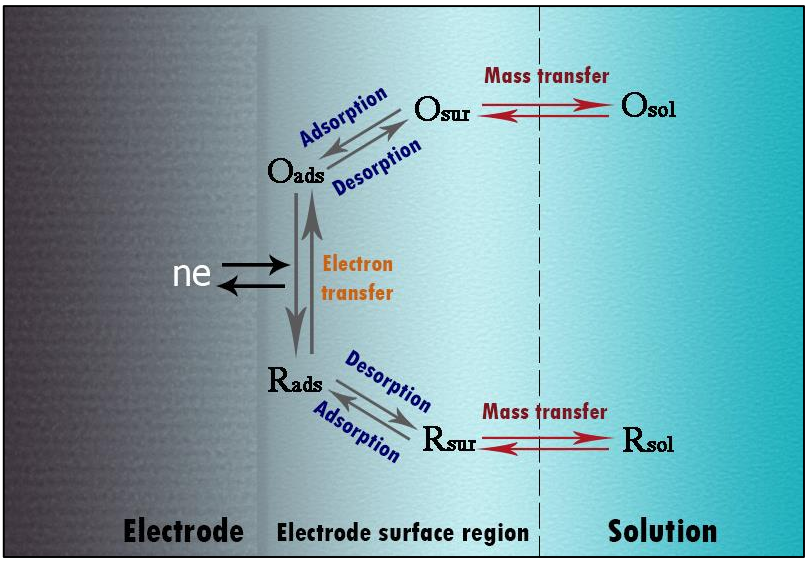


***Figure II.1.*** *General scheme of the phenomena on the surface of an electrode [3].*

It should be noted that processes such as adsorption or desorption can also occur depending on the deposition potential or the composition of the solution. These reactions are dominated by Faraday's law, which indicates that the amount of chemical reaction caused by the flow of current is directly proportional to the amount of electricity circulated. These processes are called faradic processes [3].

The electrode/electrolyte interfaces show a distribution of ions on the solution side known as the double layer model (see **Figure II.2**), which is composed of the Helmholtz layer (layer of ions and solvent in physical contact with the electrode) and the diffuse layer (layer of ions located near the electrode, whose concentration deviates from the concentration of the central zone) [2].

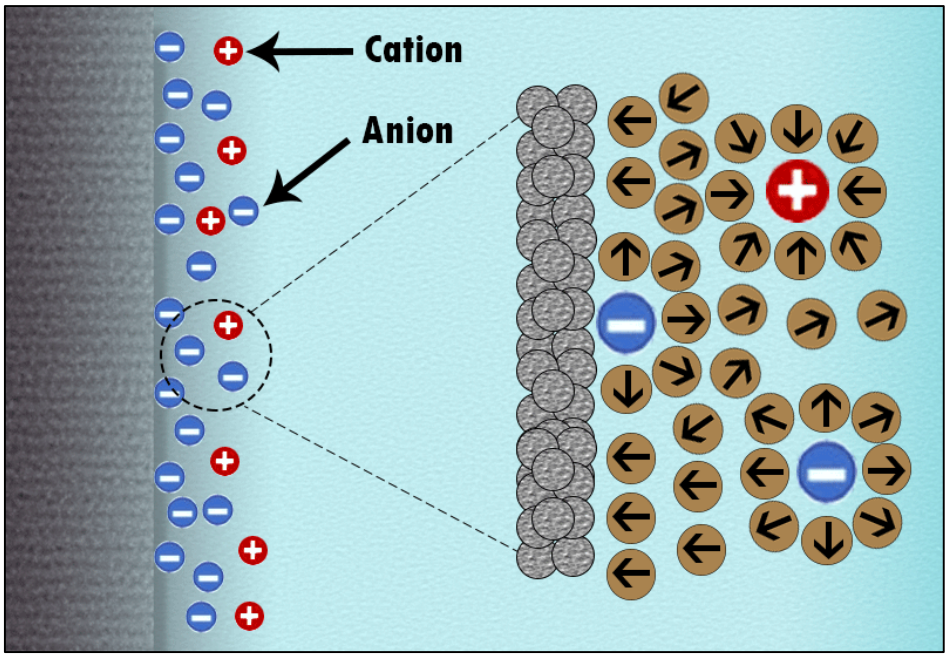


***Figure II.2.*** *Model of the electrical double layer in specific adsorption conditions [3].*

### II.1.1.2. Sol-gel

The sol-gel process is defined as a colloidal route used to synthesize amorphous and polycrystalline materials with an intermediate phase, including a gel-only state. Its importance lies in the fact that it requires a lower temperature compared to traditional synthesis methods [4]. Sol-gel is a chemical route that begins with the synthesis of a colloidal suspension of solid particles or clusters in a liquid (sol) and the hydrolysis and condensation of this sol to form a solid material filled with solvent (gel) [5]. Subsequently comes the ageing stage, where the solvent is extracted from the gel, allowing it to sit at room temperature for a while. At the end of the aging stage, there are generally still solvents and water in the material, in addition to the pore size being considerable; This involves subjecting the material to a heat treatment, at the end of which, as Pierre [6] expresses it, the material is obtained in the form of a monolith or thin film.

— *Sol-gel precursors*

The most used precursors in the sol-gel process are metal-organic compounds, whose chemical formula is: $M\text{-}(OR)_n$, where M is the metal (M =Si, Ti, Zr, AI, Sn...), OR is an alkoxide group ($-OCH_3$, $-OCH_2CH_3$...) and n is the valence of the metal. Other precursors used are water-soluble salts, among which are nitrates, chlorides, and sulfates, which are commonly used. In many applications, for cost considerations, salts become more attractive than alkoxides. During

the sol-gel process, several reactions occur, which cause the system to evolve from a sol state to a gel state [7, 8].

— *Advantages and disadvantages of the sol-gel process*

**1)** Advantages: [9, 10]

- Chemical homogeneity of the various components on a molecular scale.
- Direct and precise control of the stoichiometry of complex systems at relatively low temperatures (energy savings).
- High purity of the materials obtained.
- Obtaining new solids with improved properties.
- Possibility of making mixtures of various oxides at the atomic level, favoring the uniformity of the additives or dopants in the system.
- Possibility of obtaining serval types of materials such as powders, films or coatings, microspheres, and fibers.
- Simplicity of processing.

**2)** Disadvantages: [10]

- Existence of pores and residual carbon.
- High cost of precursors.
- Long periods for the formation of products.

### II.1.1.3. Spray pyrolyze

Spray pyrolyze (SP) deposition has been used for decades in different research, started in 1966 by Chamberlin and Skarman, [11] with the growth of thin films for solar cell applications. In general terms, the Spray Pyrolytic technique consists of generating fine droplets of a precursor solution using a carrier gas and spraying them on a hot substrate. For the deposition process, this technique differs from the others of its classification because it starts with a precursor solution in aerosol, which is directed towards the surface of the substrate, and due to the effect of temperature (pyrolysis), the aerosol decomposes, leaving a coating or film on the surface [12]. This process can be divided into three stages, as shown in **Figure II.2**.

The precursor solution can be composed of organic and inorganic salts (chlorides, nitrates, acetates, acetylacetonates, etc.) and dissolved in an alcohol medium, organic solvents, or even deionized water, depending on the desired results and the economic aspect of the products themselves. This results in mineral oxides, metal oxides, noble metals,

superconducting oxides, sulfides, chalcogenides, and selenides, among others [13]. In this way, it has been used in thermal coatings, devices such as solar cells, sensors, and anti-reflective coatings, among many more [14]. Because it is considered an aerosol deposit, there are different atomization systems (dissemination of the solution in tiny droplets), such as [15, 16]:

- Pneumatic atomization (air atomizing spray), in which a stream of compressed air is used, is also known as a pressurized spray.
- Ultrasonic Atomization is generally identified as Ultrasonic Pyrolytic Spray, which uses the vibration of a device (piezoelectric) that vibrates at high frequencies due to the phenomenon of cavitation and atomization of the solution.
- Electrostatic atomization, also called Electrostatic Deposition Spray (EDS), where the process uses a high electric field for deposition.

I) Precursor solution spray: In this stage, spray droplets are formed when the precursor solution is expelled out of the nozzle by the carrier gas. The size of the spray droplets will depend mainly on the nozzle exit diameter, the pressure of the carrier gas, and the physical properties of the solvent (density, viscosity, and surface tension). Additionally, the initial velocity of the drops must be sufficient for stage II to be carried out and to reach the surface of the substrate (stage III) [17, 18].

II) Droplet transport: in this stage, the drops travel from the nozzle to the vicinity of the substrate. The initial velocity and size of the droplets, the distance from the nozzle to the substrate, and the temperature of the substrate determine the physicochemical changes that the spray droplets can undergo during transport. On the way to the substrate, the drops can experience three forces acting simultaneously: gravitational force, thermophoresis force, and Stokes force [17,18].

III) Pyrolysis of the droplets: In this stage the transformation of the droplets occurs due to the action of heat. Figure 1-4 shows how droplets as they move through the environment toward the hot substrate undergo various changes depending on the size of the droplets and the temperature of the substrate. The four processes (A-D) shown in **Figure II.3** represent the four ways in which the droplet can interact with the substrate surface. The temperature ranges of these processes will depend on the physical properties of the solvent and the interaction of the droplets with the environment [15- 18].

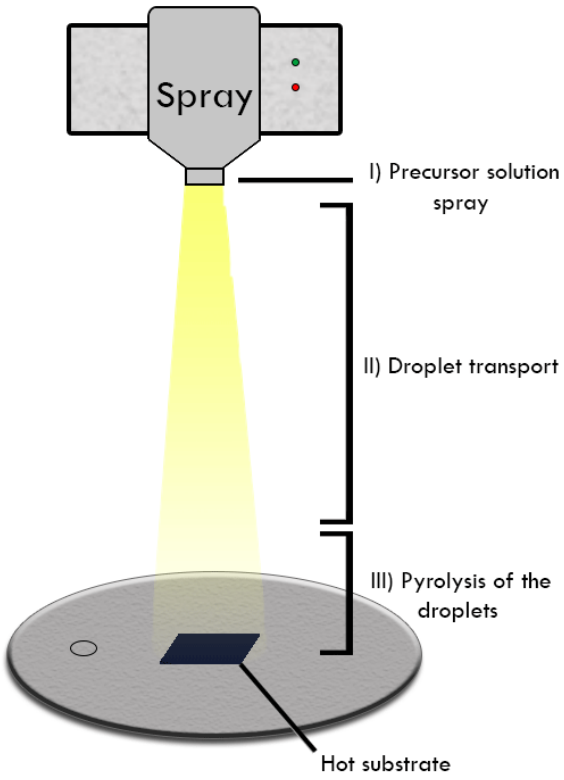


***Figure II.3.*** *Scheme of spray pyrolysis technique.*

- Process A) Low temperature—Large initial drop size: When large drops form and the substrate temperature is not high enough to completely evaporate the solution, the drop will reach the substrate and vaporize, leaving a dry precipitate. In addition, the temperature of the substrate will decrease due to the evaporation of the solvent, which can negatively affect the reaction.
- Process B) Medium-Low Temperature – Medium-High Initial Drop Size: If medium droplets form initially or the temperature increases, some evaporation of the solvent in the droplet occurs. When the concentration in the droplet exceeds the solubility limit due to evaporation, the precursor forms a dry precipitate on the surface, where decomposition occurs. Some particles evaporate and condense in gaps between the particles. Therefore, pores form, and a rough surface is favored.
- Process C) Medium-high temperature—Medium-low initial drop size: A decrease in droplet size or an increase in temperature produces the formation of a precipitate (process B). When the precipitate approaches the surface of the substrate, it vaporizes, and a heterogeneous reaction takes place on the substrate. This reaction is similar to the chemical vapor deposition (CVD) process.

- Process D) High temperature – Low initial drop size: When small droplets form or the temperature is high enough, the droplet quickly forms a precipitate. In the vicinity of the substrate, the precipitate vaporizes, and subsequently a chemical reaction occurs in the vapor phase. This homogeneous reaction leads to the formation of crystals that fall in powder form on the substrate, without any adhesion.

As shown in the description of processes A-D (**figure II.4**), the evaporation of the droplets and the subsequent pyrolysis stage are strongly related to the temperature of the substrate and the operational parameters that allow different droplet sizes to be obtained. Depending on the evaporation speed of the droplets and the pyrolysis stage, films with different morphologies can be obtained. Due to the size distribution obtained in the spray droplets, the four processes mentioned above occur simultaneously. For this reason, a study of operational parameters will be carried out to obtain the best conditions for the evaporation of the solvent and the reaction of the precursor on the substrate [18].

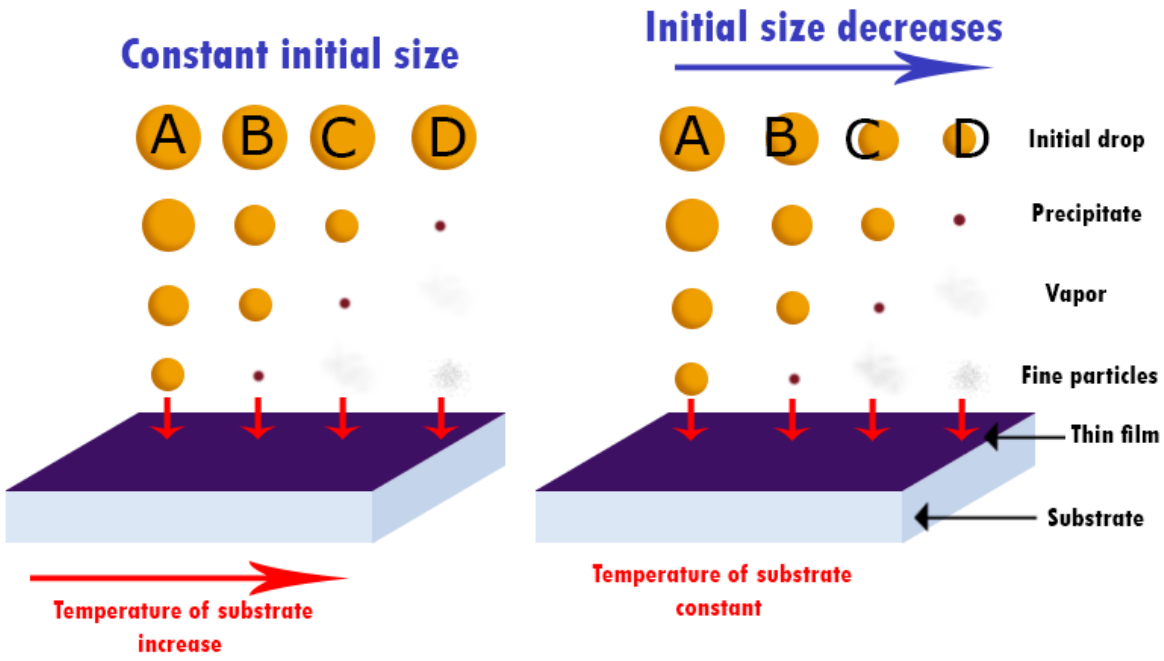


***Figure II.4.*** *Schematic of how the droplet can interact with the surface of the substrate [19].*

### II.1.1.4. Chemical bath deposition

Chemical bath deposition (CBD) is a simple and highly feasible deposition method for the synthesis of semiconductor thin films at atmospheric pressure and low temperature (below the boiling point of water). The first reported works date back to the 19th century when silver

films were deposited (1835) for the production of mirrors and lead sulfide (PbS) as the first semiconductor (1884) [20]. In this technique, a chemical bath involves different chemical reactions that take place in an alkaline solution contained in a beaker. Said solution is formed from different aqueous solutions: a source of metal ions (commonly a salt), one of the non-metallic ions or chalcogenides, a complementary agent (the most used is $NH_3$) whose function is to trap the metal ions in the reaction and release them gradually, and a source of hydroxyl ions ($OH^-$). The deposition of metal ions from the film is carried out by the condensation of metal ions and chalcogenides on the initial layer. The film will form on one or more substrates that will be immersed in the solution. With this method, it is possible to manufacture thin films of large areas at a low cost which would make it feasible to implement it at an industrial level [21].

The quality and properties of the films are influenced by different parameters such as [22-24]:

- Nature of the substrate: for this parameter, several characteristics may or may not affect the deposit, for example, the adhesion of the material, its cleanliness, roughness, etc.
- pH: there are currently some studies that show how the deposit is greatly affected by small variations in this parameter.
- Temperature: its effect is on the reaction rate of the solution and also on the adhesion of the film.
- The nature of the salt: the metal ion source must have a high solubility in water.
- Time: is related to the thickness of the films, generally there is an optimal time interval for growth.
- Type of complexing agent: it must be stable under certain deposition conditions to allow the slow and gradual release of the metal ion.

**Advantages and Disadvantages of the chemical bath deposition technique**

*Advantages [25,26]:*

- Energy consumption is minimal
- No sophisticated or high vacuum equipment is used
- Relatively low levels of pollution are generated
- It is a simple technique
- It is suitable for large-area production

*Disadvantages [25,26]:*

- Low deposit ratio
- Residuous generation
- Instability problems due to reactions with the environment

### II.1.2. Dry deposition

Dry deposition is divided in two main groups: chemical vapour deposition (CVD) and physical vapour deposition (PVD):

#### II.1.2.1. Chemical vapour deposition

Chemical vapour deposition consists of reacting gaseous chemical compounds within a reaction chamber with the substrates to be coated. The gases react on the surface of the substrate forming solid deposits of uniform thickness in an activated environment (heat, light, plasma). It is a versatile process suitable for the manufacture of powders, fibers, and thin films. With CVD, it is possible to process most metals, many non-metallic elements such as carbon and silicon, and several compounds, including carbides, nitrides, intermetallic oxides, and many others [27]. This technology is now essential in the manufacture of semiconductors and other electronic components, in the coating of tools, bearings, and other wear-resistant parts, and in optoelectronic and corrosion applications [28]. CVD can be classified as follows [28, 29]:

1) *By Input Power Source*
    - Photolytic chemical vapour deposition (PCVD): excitation by a light source or a laser.
    - Plasma-enhanced chemical vapour deposition (PECVD): excitation by electrons in a plasma where an electric field accelerates the electrons.
    - Thermal chemical vapour deposition (TCVD): heating the gas and/or the substrate.
2) *By Pressure Regime*
    - Atmospheric pressure chemical vapor deposition (APCVD): 760 Torr
    - Sub-atmospheric chemical vapor deposition: 10 Torr to 760 Torr
    - Low-pressure chemical vapor deposition LPCVD: 0.01-10 Torr

- Ultra High Vacuum chemical vapor deposition (UHV-CVD): The lowest pressure the chamber can reach is $10^{-9}$ Torr, but depositions are made from $10^{-6}$ to $10^{-3}$ Torr

*3) By Gas Precursor / Film Structure/ Growth Mechanism*

- Metal-organic chemical vapor deposition (MOCVD): Gas precursors are low-boiling organometallic liquids or solids that can sublime without decomposition.
- Epitaxy or vapour phase Epitaxy: To grow low defect density single crystal layers, they are divided into two types:
  - Homo-epitaxy: the film and the substrate are the same material.
  - Hetero-epitaxy: the film and the substrate are different materials.
- Non-epitaxial growth: Polycrystalline or amorphous films.
- Atomic layer deposition (ALD) or Atomic layer epitaxy (ALE): It is a variant of CVD used to deposit thin films one atomic layer at a time. Films produced using ALD technology are highly uniform, and the process can be enhanced by thermal or plasma.

### II.1.2.2. Physical vapour deposition

The physical vapour deposition (PVD) technique uses the condensation of the matter when atomized on substrates to form thin films. This technique falls into several techniques: cathode sputtering, laser ablation deposition (LAD), molecular beam epitaxy, and thermal evaporation [30].

#### II.1.2.2.1. Cathode sputtering

It is a non-thermal evaporation process in which the atoms located on the surface of a material are expelled physically through the transfer of momentum produced by bombarding energetic particles of atomic size on a soft material. The material particles are usually gaseous ions accelerated from plasma. In contrast, the material that is sprayed can be an element, an alloy, a composite material, or a mixture of several elements [31].

The literature presents different mechanisms for depositing coatings by sputtering depending on the type of source, chamber, and phenomenon used in the process. The following are the most mentioned types of sputtering: diode sputtering, Bias Sputtering, Ion-beam

sputtering, Direct Current (DC) sputtering, Alternating Current (AC) sputtering, and Magnetron sputtering [31].

#### II.1.2.2.2. Pulsed laser deposition

Although the consideration of pulsed laser as an energy source for evaporation and subsequent deposition of certain materials since the advent of lasers (around 1960), it took over two decades for the technique to achieve convincing results in the fabrication of high-quality thin films [32]. The first reports of deposits dated to 1965, in which dielectric and semiconductor deposition were accomplished using ruby lasers [33]. However, it was not until the mid-1980s that the PLD approach revealed its full potential, when Dijkkamp et al. [34] successfully deposited high-temperature superconductors. Since then, DLP film fabrication has been widely used not only for superconductors but also for a wide variety of complex oxides, including materials unattainable through thermodynamic equilibrium processes.

The PLD process is fundamentally simple, it basically consists of focusing a pulsed laser beam on a material (referred to as the target) to induce its evaporation-ablation. the target and substrate are positioned in a vacuum chamber, facing one other. Prior to deposition, the substrate is subjected to a high temperature ranging from 500 °C to 720 °C. The highest laser fluence (2 J/cm$^2$) is concentrated on a revolving target composed of solid material. The pulsed laser deposition method for thin films is executed through the subsequent processes [31]:

- Interaction of radiation with the target.
- Dynamics of materials that have undergone ablation.
- Deposit of the materials removed from the target onto the substrate.
- Nucleation and growth of the thin film on the substrate surface.

This method has at least the following three advantages over other conventional chemical synthesis methods:

- Low selectivity of Ablation materials.
- The possibility of a clean synthesis of nanostructures.
- The possibility of a chemical modification of nanostructures during the Ablation process.

### II.1.2.2.3. Molecular beam epitaxy

The molecular beam epitaxy (MBE) technique was introduced by Alfred Y. Cho in the early 1970s, drawing upon the foundational concepts of the "three temperature method" established by Gunther in 1958 and Arthur's research on the kinetics and structure of the GaAs surface during its interaction with molecular beams of Ga and $As_2$. In the beginning, this technique mainly obtained structures based on GaAs and AlGaAs. Still, it has now become a very versatile technique and is suitable for the epitaxial growth of semiconductor structures as well as metals, superconductors, or insulators [35].

MBE is a crystal growth technique based on the interaction of molecular beams with a heated substrate. This process is carried out under ultra-high vacuum (UHV) conditions with base pressures of the order of $10^{-10} \sim 10^{-11}$ Torr. The term “molecular beams” refers to a unidirectional kinetic flow of atoms or molecules without collisions between them, in contrast to a viscous flow. The term “epitaxial” refers to the fact that each atomic layer grows in an orderly manner on the crystalline structure of the previous layer. This implies that in growth by MBE, the quality of the substrates, which must be monocrystalline, is very important. During the last decades, it has been widely demonstrated that epitaxial material growth technologies have unique advantages over simpler techniques, despite their generally higher technological cost [36].

Since its initial development, the MBE technique has promoted research in the field of semiconductors and the development of optoelectronic devices. Nowadays it is used in the growth of elemental semiconductors of group IV (Si, Ge) and compound semiconductors III-V (GaAs, AlAs, InAs, GaP, AlP, InP, GaSb, AlSb, InSb, GaN, AlN, InN) and II-VI (ZnSe, ZnTe, CdSe, CdTe) among other materials [37].

### II.1.2.2.4. Thermal evaporation

Thermal evaporation was invented by Faraday during the 1850s by the explosion of a metal in a vacuum. The deposition of tiny metallic layers via the Joule effect was identified by Nahrwold in 1887. After World War II, evaporation techniques were utilized in several industrial applications. In this technique, the deposition is carried out by heating the material to the melting point of the material to evaporate. Thus, the material in the form of vapour condenses on the substrate. The evaporation rate increases with the difference between the vapour pressure of the source and the ambient pressure. This is why the deposition takes place

in a vacuum chamber, under a typical pressure of $10^{-4}$ Pa but to obtain very pure deposits, a vacuum of $10^{-7}$-$10^{-8}$ Pa is sometimes applied. This vacuum is achieved with a diffusion pump system or a turbo-molecular pump and a mechanical pump. The assembly of the technique (shown in **Figure II.5**) is simple, and it is very appropriate for depositing metals and some low melting point metals or oxides (Al, Ag Au, SiO, etc.) [38]. Among the main advantages of thermal evaporation are the high deposition rates and the control of the synthesis parameters, which allow the growth of the films to occur in a matter of seconds.

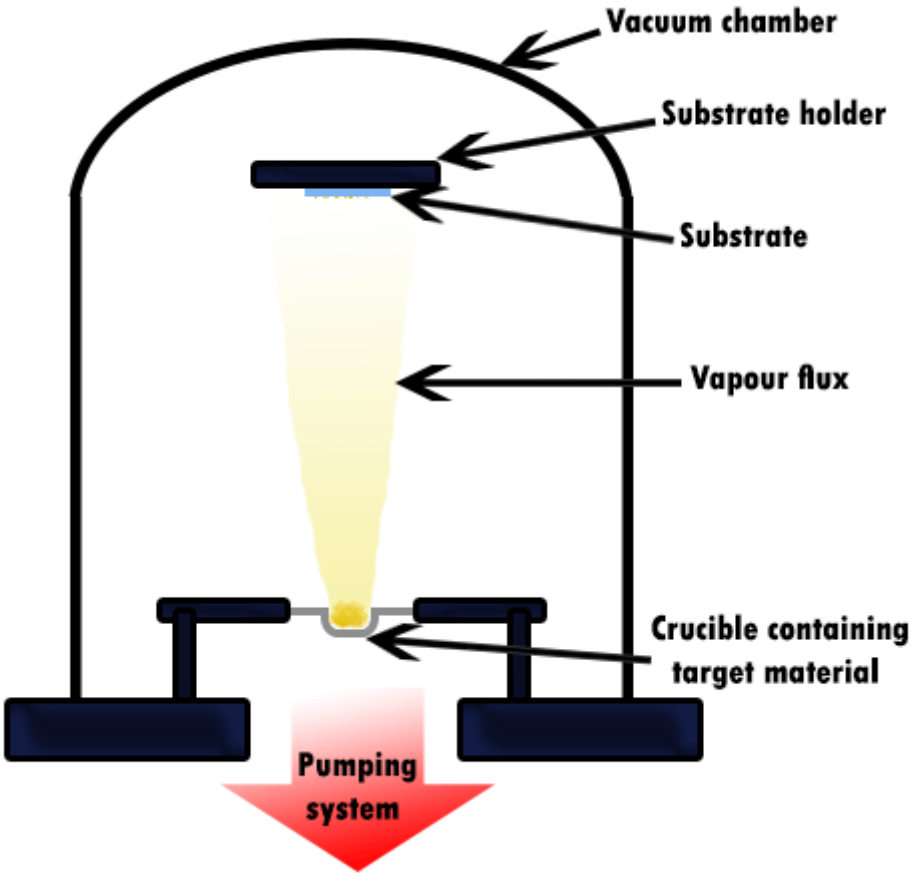


***Figure II.5.*** *Schematic of thermal evaporation technique.*

**Heating methods**

Evaporation techniques can be categorized based on the heating methods used to heat the source [39,40]:

- *Joule heating:* It consists of heating the material to be deposited by the Joule effect which will be deposited on a substrate; a strong current is passed through a refractory

metal filament, a crucible, or a boat. The evaporated material will then cover the substrate, which is generally positioned in the upper part of the vacuum chamber.

- *Electron beam heating:* It is based on the energy transfer and evaporation of the material by an electron beam. In this process, the material is heated to a sufficiently high temperature through the use of an electron beam heat source to directly change from solid to gaseous state and then deposit on the target substrate to form a thin film.
- *Electric arc heating:* An electric arc is generated by separating two electrodes connected to the terminals of a source. The formation of an intense electric field induces the ionization of the air, normally insulating, which then becomes conductive.

**Notion of vacuum**

A vacuum is a volume of gas contained in a substance that has a pressure lower than atmospheric pressure. Depending on the system pressure, different vacuum ranges can be distinguished. Although there are three ranges (low vacuum, high vacuum and ultra-high vacuum), physically we can only differentiate two based on the behaviour of the gas, namely low vacuum and high vacuum [41].

*Low vacuum*

The pressure in this range is between 1 bar and $10^{-3}$ mbar. Within this range, the gas inside the chamber is considered to be a viscous fluid, and it can be said that it is subject to the laws of ideal gases. In this range, there are still collisions between molecules and the behaviour of the fluid is completely predictable using the ideal gas model [39,40].

*High vacuum*

In this range, the pressure is less than $10^{-3}$ mbar. In this case, the residual gas in the chamber of the system stops behaving like a viscous fluid, to behaves like a free particle. Therefore, the concept of pressure must be changed to that of molecular density. The molecular density depends on the pressure and temperature at which the vapour or gas is found [42].

*Ultra-high vacuum*

The pressure boundary between high and ultra-high vacuum depends on the application to be performed since this separation has changed over time and with technological advances, although at present we can say that ultra-high vacuum starts from $10^{-9}$ mbar, currently reaching vacuums of up to around $10^{-15}$ mbar [42].

**Vacuum pumps**

There are different types of pumps to generate vacuum. Each of them has a different operation and reaches different minimum pressures. For example, mechanical pumps can be piston pumps, liquid-ring pumps, rotary pumps, these are used to generate a primary vacuum (typically not less than $10^{-3}$ mbar) [44].

To reach higher vacuums, it is necessary to use other types of pumps, among which are the diffusion pump or turbo-molecular pumps, which, in a typical high vacuum system, are placed between the mechanical pump and the chamber to be evacuated [41]. There are many other types of vacuum pumps as shown in **figure II.6**.

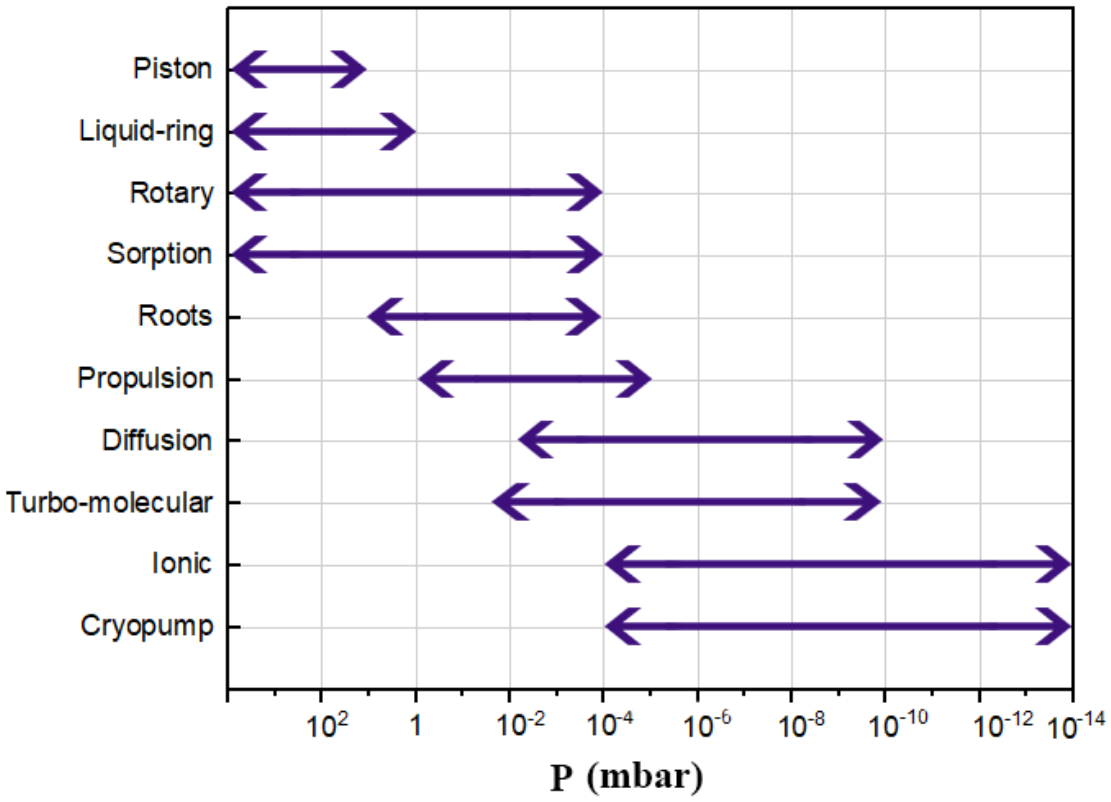


***Figure II.6.*** *Different types of pumps and their pressure range [45].*

## II.2. Characterization methods

The different characterization techniques to which the thin films and multilayers of pure and doped ZnO were subjected to analyze their structural, morphological, optical and electrical properties are described below.

### II.2.1. X-ray Diffraction (XRD)

Most of our current knowledge about the crystalline structures of materials has been obtained from research carried out using the X-ray diffraction technique. Diffraction occurs when an electromagnetic wave encounters a series of regularly spaced obstacles capable of dispersing the wave, separated by distances of the same order of magnitude as the wavelength. The conditions for diffraction to occur are described below.

#### II.2.1.1. Bragg's Law

The law of Bragg explains simply the behaviour of diffracted beams in a crystal. He considered the crystal to be composed of parallel planes (hkl). X-rays are a form of electromagnetic radiation with high energy and short wavelength approximately equal to the interplanar distance of crystalline solids. When an X-ray beam hits a solid material, it is dispersed in all directions due to the electrons associated with the atoms of the crystalline planes. Bragg assumes that these crystalline planes (hkl) act as mirrors reflecting the incident X-ray beam [46].

The constructive interference of scattered waves causes diffraction. The waves are mutually reinforced if the waves scattered by the obstacles are in phase or with a phase difference of 2πn radians (where n is an integer number) [46].

**Figure II.7** illustrates a schematic representation of Bragg's law. The reflected incident beam and the parallel planes of atoms with Miller indices (hkl) separated by a distance $d_{hkl}$ are indicated. It is assumed that a parallel, monochromatic and coherent beam of X-rays of wavelength λ incident on these planes with an angle θ and is scattered by atoms A and B. For the beam to be constructively interfered with, the difference in the optical path travelled by ray 2 must be equal to an integer $n$ of wavelength [47, 48]:

$$n\lambda = \overline{CB} + \overline{BD} \quad \text{(II.1)}$$

$$n\lambda = 2\, d_{hkl}\, \sin\theta \quad \text{(II.2)}$$

The **equation II.2** is Bragg's law, where $n$ is an integer corresponding to the diffraction order. Since sinθ will never exceed one, the equation can only be established for wavelengths $\lambda < 2d$.

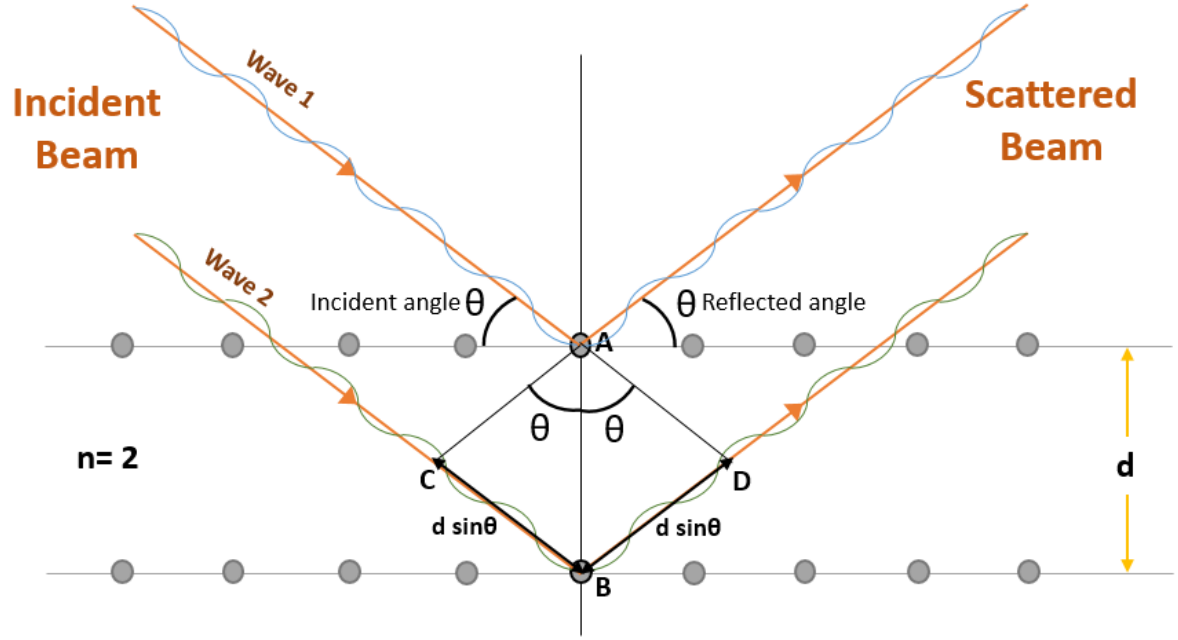


***Figure II.7.*** *Schematic representation of Bragg's law conditions [46,47].*

### II.2.1.2. Diffraction technique

One of the diffraction techniques is exposing the thin film to monochromatic X-ray radiation using a diffractometer, which determines the angles at which diffraction occurs in the samples. The geometric configuration used is a parallel beam, using a global mirror (parabolic mirror), and it is achieved that the rays are parallel when they hit the sample. The parallel rays' incident on the sample and a parallel diffracted beam is obtained, despite any inhomogeneities the sample may present. This configuration allows the angle of incidence of the X-ray beam on the film to be set. A diagram of this configuration can be seen in Figure 2.2. The sample (thin film) is placed on the fixed sample holder. At point A, a monochromatic X-ray beam is generated, reflected in a Gobel mirror and then hits the sample. Point B represents the scintillation detector rotating around the O axis and moving at a constant angular velocity, recording the intensities of the diffracted X-rays. The angular position, as a function of 2θ, is determined using a vertical goniometer [46-48].

### II.2.2. Ultraviolet-Visible-NIR spectroscopy

The optical properties of thin films can be characterized by measurements of transmittance (percentage of energy transmitted) and/or absorbance (percentage of energy absorbed) and reflectance (capacity of a surface to reflect light) [49]. These measurements allow determining, by indirect graphical methods (Tauc plot method), the optical band gap of the material, which is a very important property or parameter in the study of TCOs.

Ultraviolet-Visible-NIR spectroscopy is a widely used non-destructive method that provides information on the optical properties of materials. Absorption spectroscopy is a technique that measures and interprets the changes in electromagnetic radiation when it interacts with the material. It is known that in the visible and ultraviolet regions, there are changes that involve the electronic energies of atoms or molecules. When an electromagnetic wave of the defined wavelength hits a solid or substance, it will undergo absorption. The fraction of radiation absorbed depends on the nature of the material and the thickness of the sample [49]. The intensity of the incident beam is represented by $I_0$, the intensity of the transmitted beam by I, and the thickness of the sample by t. The absorption or optical density of a material is defined as [50]:

$$A = log\frac{I_0}{I} \tag{II.3}$$

The intensity of the transmitted beam depends on the thickness and characteristics of the material and is related to the intensity of the incident beam by the expression [51]:

$$I = I_0 \exp(-\alpha t) \tag{II.4}$$

where $\alpha$ is the absorption coefficient, and t is the thickness of the material.

A UV-Vis spectrometer plots the sample's absorbance or optical density as a function of the wavelength of the incident beam.

Because $\frac{I}{I_0}$ is the fraction of light transmitted by the material, it is multiplied by 100 to give the total transmittance of the material, as seen in **equation II.5**.

$$T = \frac{I}{I_0} \times 100 \tag{II.5}$$

From **equation II.4** and **equation II.5**, we can express the absorption coefficient as:

$$\alpha = \frac{1}{t} \ln\left(\frac{100}{\%T}\right) \quad \text{(II.6)}$$

This approximate relationship is established, neglecting reflections at all interfaces (air/layer and air/substrate).

In the strong absorption domain ($\alpha > 10^4 cm^{-1}$) for a direct gap such as that of ZnO, α is expressed as a function of the band gap (Eg) according to the following equation [49]:

$$\alpha h\nu = A(h\nu - E_g)^{1/2} \quad \text{(II.7)}$$

Where A is a constant and hν represents the energy of a photon.

The Tauc plot method can be used to estimate the band gap of a thin film from the absorption coefficient α. By scanning the entire energy domain and plotting $(\alpha h\nu)^2$ as a function of the energy of a photon (hν), we could obtain the value of Eg from extrapolating the linear part of α to the x-axis (i.e. for α = 0) [50].

### II.2.3. Scanning Electron Microscopy

The Scanning Electron Microscope (SEM) was invented in 1937 by Manfred von Ardenne [52]. It utilizes an electron beam to generate a picture. The resolution of a microscope refers to its capacity to accurately differentiate two distinct points or objects as separate and identifiable entities. When the objects are in such proximity that their resolving capacity is insufficient, they merge into a single image and become indistinguishable [53].

Preparing the samples for this microscope is quite simple, as most scanning electron microscopes just require them to be conductive. Next, the surface is subjected to electron scanning using accelerated electrons emitted from the cannon. An electromagnet-based lens detector quantifies and measures the quantity and intensity of electrons emitted by the sample, enabling the generation of three-dimensional digital images. The resolution of the microscope varies between 4 nm and 20 nm. Typically, its depth of focus is 10 mm, which is significantly less compared to the transmission electron microscope. An advantage of the scanning electron microscope is its ability to generate three-dimensional images by focusing on the surface of the structures [53, 54].

### II.2.4. Raman spectroscopy

In 1928, C.V. Raman discovered the phenomenon that bears his name. With only rudimentary instrumentation available, Sir Raman used sunlight as a source and a telescope as

a collector; and the detector was his eyes. Raman spectroscopy is a high-resolution photonic technique that provides chemical and structural information on any material, allowing its identification. Analysis using this technique is based on the examination of the light scattered by a material when a monochromatic beam of light falls on it. A small part of the light is scattered inelastically, experiencing slight changes in the frequency of the incident light. Therefore, this technique does not require special preparation of the sample before analysis and does not alter the properties of the materials, so it is considered non-destructive [55, 56].

Raman spectroscopy analysis is based on having a monochromatic beam of light with a frequency $v_0$ incident on a sample whose molecular characteristics are to be determined. Most of the light scattered by the sample has the same frequency as the incident light, but a very small part has a change in frequency, resulting from the interaction of the light with matter. The light that maintains the same frequency $v_0$ as the incident light is known as Rayleigh scattering and does not provide any information about the composition of the sample. On the other hand, the scattered light that has frequencies different from the incident light is what provides information about the molecular composition of the sample and is what we know as Raman scattering. The new frequencies, $+v_r$ and $-v_r$, are the Raman frequencies, characteristic of the chemical nature and physical state of the sample and independent of the incident radiation [56,57].

### II.2.5. Four-point probe test

The electrical conductivity of materials (σ) is the ability of a material to conduct electric current through it. It depends on the number of electrons belonging to the conduction band, the number of holes in the valence band and the mobility of the charge carriers (electrons or holes) [58]. Conductivity also depends on other physical factors specific to the material and on temperature. It is determined from Ohm's law, which states that the current running between two points in a conductor is directly proportional to the potential difference across its ends [59].

The four-point probe method (**figure II.8**) is an experimental method commonly used to measure the shit resistance and resistivity of a bulk semiconductor. It is applied in four aligned points, equidistant by a small distance l and which rest on the surface of the layer. A current I is sent between point 1 and point 4, and the V is measured between points 2 and 3; the ratio (V/I) is linked to the resistivity according to the dimensions of the sample.

The sheet resistance Rs can then be calculated using the following equation [60]:

$$R_s = \frac{\pi}{\ln(2)} \frac{\Delta V}{I} = 4.5324 \frac{\Delta V}{I} \quad \text{(II.8)}$$

Where ΔV is the change in voltage measured between the inner probes (2 and 3), and I is the current applied between the outer probes (1 and 4).

If the thickness is known, the resistivity of the film (ρ) can be calculated using sheet resistance as follows [60]:

$$\rho = R_s \times thikness \quad \text{(II.9)}$$

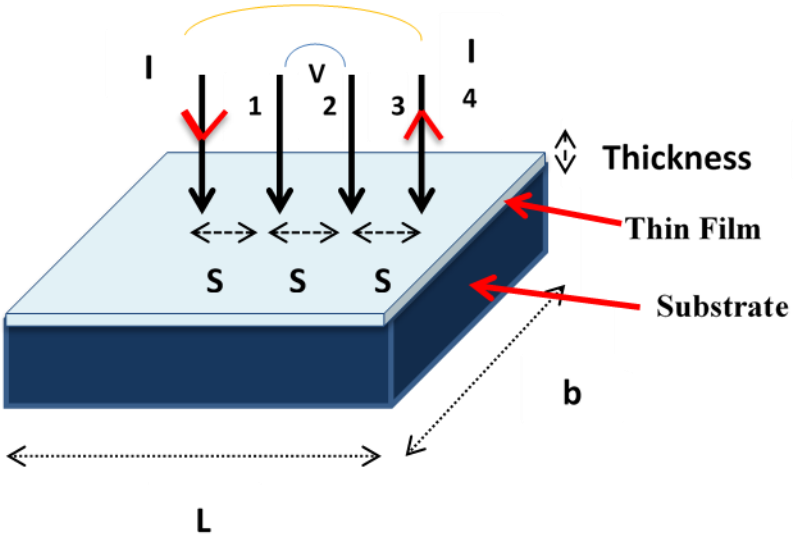


***Figure II.8.*** *Simplified illustration of the four-point technique [61].*

### II.2.6. Contact angle

Contact angle measurement is an important technique used to determine the wettability of a surface. It is defined as the angle created between the tangent to the liquid surface and the solid surface at the point where both come into touch. This measurement provides critical information regarding the interaction between a liquid and a solid substrate, which is important for many applications in the fields of material science, engineering, and chemistry. The contact angle, represented as θ, is obtained by examining the shape of a droplet that is placed on a surface. This study is done using techniques like the sessile drop method, where a liquid droplet is placed on a solid surface and the angle is evaluated using image analysis. The Young-Laplace equation, which governs the equilibrium of forces at the contact line, establishes a relationship between the contact angle and the surface tensions of both the liquid and the solid [62, 63].

High contact angles, which are more than 90°, indicate a surface that repels water (hydrophobic). On such a surface, the liquid forms droplets that do not spread much, showing the lowest level of wettability. On the other hand, low contact angles, which are less than 90°, imply a surface that attracts water (hydrophilic). On a hydrophilic surface, the liquid spreads more easily, which means the highest level of wettability. The accuracy of contact angle measurements is crucial for comprehending surface interactions in various applications, including coatings, adhesives, biomedical implants, and microfluidic devices [62-64].

## Conclusion

In this second chapter, we presented an overview of different wet and dry deposition techniques. Each method could provide us with specific characteristics of films depending on several parameters (such as deposition time). Choosing the deposition technique is critical in the application of the deposited thin film. We also described the structural, morphological, optical, and electrical characterization techniques used during this work.

## References

*[1] Chen, H., Wei, Z., Zheng, X., & Yang, S. (2015). A scalable electrodeposition route to the low-cost, versatile and controllable fabrication of perovskite solar cells. Nano Energy, 15, 216-226.*

*[2] Lincot, D. (2005). Electrodeposition of semiconductors. Thin solid films, 487(1-2), 40-48.*

*[3] Crapnell, R. D., & Banks, C. E. (2024). Interpreting Electrochemistry. In The Handbook of Graphene Electrochemistry (pp. 25-89). London: Springer London.*

*[4] Guo, Y. (1993). Sol-gel synthesis and characteristics of the rare earth phosphate glasses. The Catholic University of America.*

*[5] Hench, L. L., & West, J. K. (1990). The sol-gel process. Chemical reviews, 90(1), 33-72.*

*[6] Pierre, A. C. (2020). Introduction to sol-gel processing. Springer Nature.*

*[7] Guglielmi, M., & Carturan, G. (1988). Precursors for sol-gel preparations. Journal of Non-Crystalline Solids, 100(1-3), 16-30.*

*[8] Danks, A. E., Hall, S. R., & Schnepp, Z. J. M. H. (2016). The evolution of 'sol–gel'chemistry as a technique for materials synthesis. Materials Horizons, 3(2), 91-112.*

*[9] Hench, L. L., & West, J. K. (1990). The sol-gel process. Chemical reviews, 90(1), 33-72.*

*[10] Pierre, A. C. (2020). Introduction to sol-gel processing. Springer Nature.*

*[11] Chamberlin, R. R., & Skarman, J. S. (1966). Chemical spray deposition process for inorganic films. Journal of the Electrochemical Society, 113(1), 86.*

*[12] Workie, A. B., Ningsih, H. S., & Shih, S. J. (2023). An comprehensive review on the spray pyrolysis technique: Historical context, operational factors, classifications, and product applications. Journal of Analytical and Applied Pyrolysis, 170, 105915.*

*[13] Skrabalak, S. E., & Suslick, K. S. (2006). Porous carbon powders prepared by ultrasonic spray pyrolysis. Journal of the American Chemical Society, 128(39), 12642-12643.*

*[14] Jung, D. S., Park, S. B., & Kang, Y. C. (2010). Design of particles by spray pyrolysis and recent progress in its application. Korean Journal of Chemical Engineering, 27, 1621-1645.*

*[15] Falcony, C., Aguilar-Frutis, M. A., & García-Hipólito, M. (2018). Spray pyrolysis technique; high-K dielectric films and luminescent materials: a review. Micromachines, 9(8), 414.*

*[16] Ukoba, K. O., Eloka-Eboka, A. C., & Inambao, F. L. (2018). Review of nanostructured NiO thin film deposition using the spray pyrolysis technique. Renewable and Sustainable Energy Reviews, 82, 2900-2915.*

*[17] Lehraki, N., Aida, M. S., Abed, S., Attaf, N., Attaf, A., & Poulain, M. (2012). ZnO thin films deposition by spray pyrolysis: Influence of precursor solution properties. Current applied physics, 12(5), 1283-1287.*

*[18] Patil, P. S. (1999). Versatility of chemical spray pyrolysis technique. Materials Chemistry and physics, 59(3), 185-198.*

*[19] Falcony, C., Aguilar-Frutis, M. A., & García-Hipólito, M. (2018). Spray pyrolysis technique; high-K dielectric films and luminescent materials: a review. Micromachines, 9(8), 414.*

*[20] Ezekoye, B. A., Offor, P. O., Ezekoye, V. A., & Ezema, F. I. (2013). Chemical bath deposition technique of thin films: a review. International Journal of Scientific Research, 2(8), 452-456.*

*[21] Guneri, E., Ulutas, C., Kirmizigul, F., Altindemir, G., Gode, F., & Gumus, C. (2010). Effect of deposition time on structural, electrical, and optical properties of SnS thin films deposited by chemical bath deposition. Applied Surface Science, 257(4), 1189-1195.*

*[22] Göde, F. A. T. M. A., Gümüş, C. E. B. R. A. İ. L., & Zor, M. U. H. S. İ. N. (2007). Investigations on the physical properties of the polycrystalline ZnS thin films deposited by the chemical bath deposition method. Journal of Crystal Growth, 299(1), 136-141.*

*[23] Abdulrahman, A. F., Ahmed, S. M., Ahmed, N. M., & Almessiere, M. A. (2020). Enhancement of ZnO nanorods properties using modified chemical bath deposition method: effect of precursor concentration. Crystals, 10(5), 386.*

*[24] Baviskar, P. K., & Karade, S. S. (2023). Chemical Bath Deposition: Thin Films with Assorted Morphologies. In Simple Chemical Methods for Thin Film Deposition: Synthesis and Applications (pp. 27-95). Singapore: Springer Nature Singapore.*

*[25] Kassim, A., Tee, T. W., Abdullah, A. H., Nagalingam, S., & Min, H. S. (2010). Deposition and characterization of Cu 4 SnS 4 thin films by chemical bath deposition method. Macedonian journal of chemistry and chemical engineering, 29(1), 97-103.*

*[26] Choy, K. L. (2003). Chemical vapour deposition of coatings. Progress in materials science, 48(2), 57-170.*

*[27] Kern, W., & Schuegraf, K. K. (2001). Deposition technologies and applications: Introduction and overview. In Handbook of Thin Film Deposition Processes and Techniques (pp. 11-43). William Andrew Publishing.*

*[28] Morosanu, C. E. (2016). Thin films by chemical vapour deposition (Vol. 7). Elsevier.*

*[29] Chaudhari, M. N., Ahirrao, R. B., & Bagul, S. D. (2021). Thin film deposition methods: A critical review. Int. J. Res. Appl. Sci. Eng. Technol, 9(6), 5215-5232.*

*[30] Wang, C., Dai, X., Guan, X., Jia, W., Bai, Y., & Li, J. (2020). LiCoO2 thin film cathode sputtered onto 500° C substrate. Electrochimica Acta, 354, 136668.*

*[31] Schneider, C. W., & Lippert, T. (2010). Laser ablation and thin film deposition. Laser Processing of Materials: Fundamentals, Applications and Developments, 89-112.*

*[32] Xia, Q., Zan, F., Zhang, Q., Liu, W., Li, Q., He, Y., ... & Xia, H. (2023). All-solid-state thin film lithium/lithium-ion microbatteries for powering the Internet of things. Advanced Materials, 35(2), 2200538.*

*[33] Birnbaum, M. (1965). Semiconductor surface damage produced by ruby lasers. Journal of Applied Physics, 36(11), 3688-3689.*

*[34] Dijkkamp, D., Venkatesan, T., Wu, X. D., Shaheen, S. A., Jisrawi, N., Min-Lee, Y. H., ... & Croft, M. (1987). Preparation of Y-Ba-Cu oxide superconductor thin films using pulsed laser evaporation from high T c bulk material. Applied Physics Letters, 51(8), 619-621.*

*[35] Orton, J. W., & Foxon, T. (2015). Molecular beam epitaxy: a short history. Oxford University Press.*

*[36] TYRRELL, B. (2020). MOLECULAR BEAM EPITAXY. In Between Making And Knowing: Tools In The History Of Materials Research (pp. 357-365).*

*[37] Asahi, H., & Horikoshi, Y. (Eds.). (2019). Molecular Beam Epitaxy: Materials and applications for electronics and optoelectronics. John Wiley & Sons.*

*[38] Sivaram, S. (2013). Chemical vapor deposition: thermal and plasma deposition of electronic materials. Springer Science & Business Media.*

*[39] Deshpandey, C. V., & Bunshah, R. F. (1991). Evaporation processes (pp. 79-132). Academic, Boston.*

*[40] Gatzen, H. H., Saile, V., Leuthold, J., Gatzen, H. H., Saile, V., & Leuthold, J. (2015). Deposition Technologies. Micro and Nano Fabrication: Tools and Processes, 65-203.*

*[41] Jousten, K. (Ed.). (2016). Handbook of vacuum technology. John Wiley & Sons.*

*[42] Gatzen, H. H., Saile, V., & Leuthold, J. (2015). Micro and nano fabrication. Springer, Berlin, Heidelberg, 1(5.2), 2.*

*[43] Wiegleb, G. (2023). Physical Properties of Gases. In Gas Measurement Technology in Theory and Practice: Measuring Instruments, Sensors, Applications (pp. 7-125). Wiesbaden: Springer Fachmedien Wiesbaden.*

*[44] O'Hanlon, J. F. (2003). A user's guide to vacuum technology. John Wiley & Sons.*

*[45] Biltoft, P. J. (2004). Vacuum Technology (No. UCRL-BOOK-207375). Lawrence Livermore National Lab.(LLNL), Livermore, CA (United States).*

*[46] Pecharsky, V. K., & Zavalij, P. Y. (2003). Fundamentals of diffraction (pp. 99-260). Springer US.*

*[47] Whittig, L. D., & Allardice, W. R. (1986). X-ray diffraction techniques. Methods of Soil Analysis: Part 1 Physical and Mineralogical Methods, 5, 331-362.*

*[48] Fultz, B., Howe, J. M., Fultz, B., & Howe, J. M. (2001). Diffraction and the X-ray powder diffractometer. Transmission electron microscopy and diffractometry of materials, 1-61.*

*[49] Picollo, M., Aceto, M., & Vitorino, T. (2019). UV-Vis spectroscopy. Physical sciences reviews, 4(4), 20180008.*

*[50] Shard, A. G., Schofield, R. C., & Minelli, C. (2020). Ultraviolet–visible spectrophotometry. In Characterization of Nanoparticles (pp. 185-196). Elsevier.*

*[51] Luna, T. R. (2011). Characterization of CoS and Co1-xCdxS thin films deposited by spray pyrolysis technique.*

*[52] McMullan, D. (2004). Appendix II a history of the scanning electron microscope, 1928–1965. In Advances in Imaging and Electron Physics (Vol. 133, pp. 523-545). Elsevier.*

*[53] Zhou, W., Apkarian, R., Wang, Z. L., & Joy, D. (2007). Fundamentals of scanning electron microscopy (SEM). Scanning microscopy for nanotechnology: techniques and applications, 1-40.*

*[54] Goldstein, J. I., Newbury, D. E., Michael, J. R., Ritchie, N. W., Scott, J. H. J., & Joy, D. C. (2017). Scanning electron microscopy and X-ray microanalysis. springer.*

*[55] Singh, R. (2002). CV Raman and the Discovery of the Raman Effect. Physics in Perspective, 4, 399-420.*

*[56] Lyon, L. A., Keating, C. D., Fox, A. P., Baker, B. E., He, L., Nicewarner, S. R., Natan, M. J. (1998). Raman spectroscopy. Analytical Chemistry, 70(12), 341-362.*

*[57] Mulvaney, S. P., & Keating, C. D. (2000). Raman spectroscopy. Analytical Chemistry, 72(12), 145-158.*

*[58] Simon, J., & Andre, J. J. (2012). Molecular semiconductors: photoelectrical properties and solar cells. Springer Science & Business Media.*

*[59] Maier, J. (2023). Physical chemistry of ionic materials: ions and electrons in solids. John Wiley & Sons.*

*[60] Uyanık, Z. (2019). Improvement of transparent conductive hybrid ITO/Ag/ITO electrodes by electro-annealing (Master's thesis, Izmir Institute of Technology (Turkey)).*

*[61] Zhao, T., & Jiang, L. (2018). Contact angle measurement of natural materials. Colloids and Surfaces B: Biointerfaces, 161, 324-330.*

*[52] Le-Quoc, H. (2011). Thermoelectric material Mg 2 Si-Mg 2 Sn elaborated in thin films by plasma assisted co-sputtering.*

*[63] Huhtamäki, T., Tian, X., Korhonen, J. T., & Ras, R. H. (2018). Surface-wetting characterization using contact-angle measurements. Nature protocols, 13(7), 1521-1538.*

*[64] Beketov, G. V., & Shynkarenko, O. V. (2022). SURFACE WETTING AND CONTACT ANGLE: BASICS AND CHARACTERISATION. Chemistry, Physics & Technology of Surface/Khimiya, Fizyka ta Tekhnologiya Poverhni, 13(1).*

# Materials and Methods

## Introduction

This chapter contains a detailed description of the used materials and the experimental procedures adopted to prepare Mn:ZnO thin films and MnZnO/Ag/ZnO:Mn multilayers via the thermal evaporation method. As well as, several characterization techniques that were utilized to investigate the structure, morphology, and optical and electrical properties. Finally, a detailed description of the metaheuristic methods employed to calculate the optical parameters of our films.

### III.1. Experimental deposition device

Vacuum Evaporation was carried out in a device set up at CDTA with a cylindrical Pyrex glass chamber of a volume of 7218.86 $cm^3$, closed at the top by a steel flange with a diameter of 23 cm. The device is equipped with an extraction unit that provides a high vacuum, consisting of a rotary vane pump for the primary vacuum ($10^{-2}$ mbar) and an oil diffusion pump for the secondary vacuum ($10^{-5}$ mbar). The material to be deposited (powder) is placed in a tungsten crucible, which is connected to two electrodes powered by a transformer (**figure III.1**). The powder must be spread evenly in the crucible to prevent clumping. The substrate holder is movable to fix a preferable distance between the crucible and the substrate; in our case, it was located 11 cm away, where many samples can be placed to be coated at the same time.

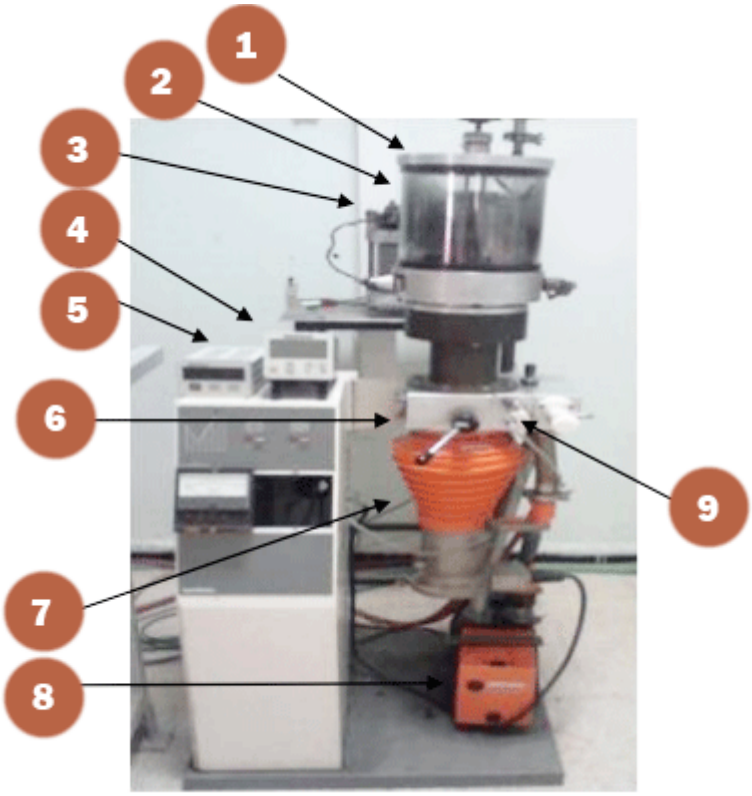


***Figure III.1.*** *Photograph of the CDTA vacuum vaporization device*

**1-** The flask.
**2-** The cylindrical chamber.
**3-** The transformer.
**4-** Primary vacuum display box.
**5-** The secondary vacuum display box.
**6-** Pump ignition buttons.
**7-** Oil diffusion pump
**8-** The rotary vane pump.
**9-** The secondary vacuum pressure gauge.

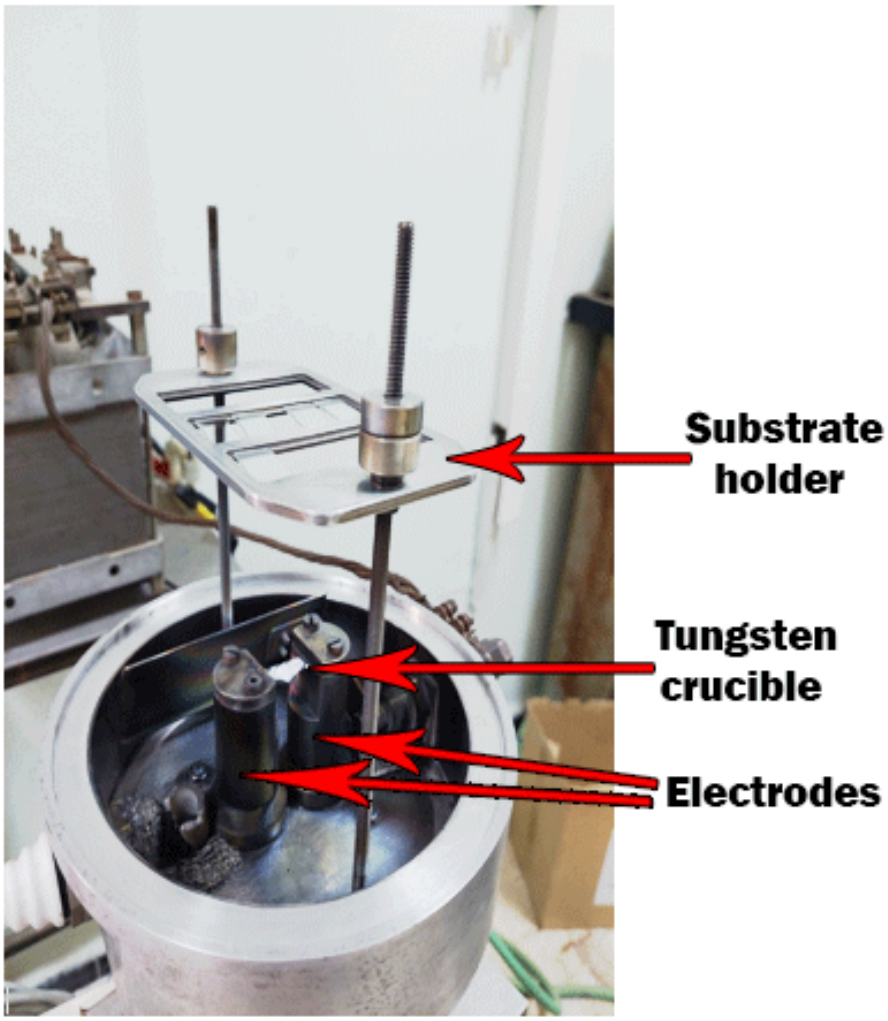


***Figure III.2.*** *Photograph of the interior of the cylindrical chamber.*

### III.2. Materials used and choice of substrates

During our experiments, we used zinc and magnesium powders purchased from SIGMA-ALDRICH, which have a purity of 99.99%. The silver came in grains from GoodFellow50, which also have a purity of 99.99%.

The choice of substrate type is primarily related to the objectives of our layers and the characterizations conducted on the samples after deposition. In our case, our samples are destined for solar cell window applications, so we used ordinary glass as a substrate. The glasses used during our work are microscope clear slides of (Sail Brand), ground edges,1 mm thick and 25.4 x 76.2 $mm^2$ in surface area.

### III.3. Cleaning of substrates

Cleaning is a very important step as it eliminates all traces of grease and dust through a purely chemical process. Before each deposition, the substrates are well-cleaned. First, we immersed the glass substrates in a beaker full of acetone in an ultrasonic bath (**Figure III.3 (A)**) at low frequency (25 kHz) for 10 minutes to remove organic particles, followed by another 10 minutes in ethanol. Finally, we rinsed them with deionized water and dried them on a heating plate (**Figure III.3 (B)**). This operation is carried out just before deposition to prevent the formation of oxide during the substrate's storage.

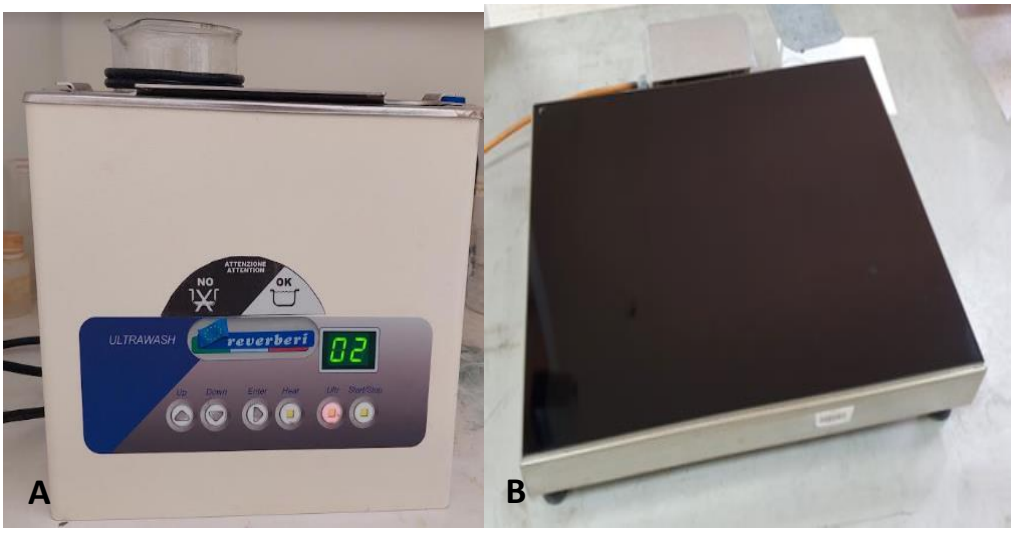


***Figure III.3.*** *Materials used to prepare the deposit: A. The ultrasonic bath and C. the heating plate.*

### III.4. Procedures and deposition conditions

#### III.4.1. Preparing the ZnO and Mn-doped ZnO thin films

At first, we only used ZnO powder to deposit pure ZnO thin film by thermal evaporation. After that, we used a mixture of ZnO and Mn powders. The powders are mixed just before the deposition. We did serval experiments and based on our previous works, the weight percentage of Mn we used is varying from 5 wt.- % to 20 wt.- % for both the Mn doped ZnO thin films samples and the multilayers.

#### III.4.2. Preparing ZnO/Ag/ZnO and Mn:ZnO/Ag/ZnO:Mn multilayers

In this part, we went through several stages to obtain the samples consisting of three layers, with the first sample being ZnO/Ag/ZnO. Starting with the first step, we deposit the first

layer of ZnO on the glass substrate through thermal evaporation. The next step is to deposit a layer of silver on the previous substrate, and for the third step, we add a final layer of ZnO on the two previous layers in the same manner. Finally, we obtain the first sample of the multilayer. For the doped multilayers, we proceed in the same way as for the first sample; however, instead of the ZnO layer, we deposited the Mn-doped ZnO layer by mixing ZnO and Mn powders in the crucible. Mn percentages are the same as in the first part.

### III.4.3. Conditions of deposition

Before starting each experiment, we wait for a sufficient vacuum to be achieved within the chamber. First, we start the primary pumping until we reach a pressure of about $10^{-2}$ mbar, then we will initiate the secondary pumping until we reach around $10^{-6}$ mbar. After vacuum sealing the chamber, we will proceed with the evaporation of the material using a crucible heated electrically by the Joule effect and, finally, the condensation of the vapour onto the substrates. The conditions of deposition for the single layers and multilayers are presented in **Table III.1** and **Table III.2**, respectively. The total time of the deposition of all our samples is 30 seconds. A silicon substrate was placed every time along with glass substrates to determine the thickness of the films, which is then measured using a profilometer.

***Table III.1.*** *Experimental conditions for the deposition of Pure ZnO and Mn-doped ZnO.*

| | $P_1.10^{-2}$ (mbar) | $P_2.10^{-5}$ (mbar) | $P_{Work}.10^{-4}$ (mbar) | Weight (mg) |
|---|---|---|---|---|
| *Pure ZnO* | 2.3 | 2.6 | 1.1 | $Wt_{ZnO}$= 100 |
| | | | | $Wt_{Mn}$= 0 |
| *Mn:ZnO (5wt.-%)* | 2.4 | 2.4 | 1.3 | $Wt_{ZnO}$= 95 |
| | | | | $Wt_{Mn}$= 5 |
| *Mn:ZnO (10wt.-%)* | 2.2 | 2.9 | 1.2 | $Wt_{ZnO}$= 90 |
| | | | | $Wt_{Mn}$= 10 |
| *Mn:ZnO (15wt.-%)* | 2.1 | 3.1 | 1.2 | $Wt_{ZnO}$= 85 |
| | | | | $Wt_{Mn}$= 15 |
| *Mn:ZnO (20wt.-%)* | 2.5 | 2.2 | 1.3 | $Wt_{ZnO}$= 80 |
| | | | | $Wt_{Mn}$= 20 |

***Table III.2.*** *Experimental conditions for the deposition of ZnO/Ag/ZnO and Mn:ZnO/Ag/ZnO:Mn.*

| | $P_1.10^{-2}$ (mbar) | $P_2.10^{-5}$ (mbar) | $P_{Work}.10^{-4}$ (mbar) | Weight (mg) |
|---|---|---|---|---|
| *ZnO/Ag/ZnO* | 2.45 | 2.9 | 1.2 | $Wt_{ZnO}$= 100 |
| | | | | $Wt_{Mn}$= 0 |
| *Mn:ZnO/Ag/ Mn:ZnO (5wt.-%)* | 2.1 | 2.1 | 1.3 | $Wt_{ZnO}$= 95 |
| | | | | $Wt_{Mn}$= 5 |
| *Mn:ZnO/Ag/ Mn:ZnO (10wt.-%)* | 2.5 | 3.5 | 1.3 | $Wt_{ZnO}$= 90 |
| | | | | $Wt_{Mn}$= 10 |
| *Mn:ZnO/Ag/ Mn:ZnO (15wt.-%)* | 2.4 | 3.6 | 1.2 | $Wt_{ZnO}$= 85 |
| | | | | $Wt_{Mn}$= 15 |
| *Mn:ZnO/Ag/ Mn:ZnO (20wt.-%)* | 2.5 | 2.2 | 1.1 | $Wt_{ZnO}$= 80 |
| | | | | $Wt_{Mn}$= 20 |

### III.5. Thermal annealing

Annealing is a heat treatment that involves processing the layer after deposition, combining heating and cooling operations to enhance the material's properties (oxidation and recrystallization of the films). After the deposition, the samples were annealed in a furnace under the atmosphere at 500°C for two hours, along with the preservation of the samples without annealing, which will be used as references for a comparative study.

### III.6. Characterization techniques

This work aims to analyze various structural, optical, electrical properties wettability of TCOs thin films deposited on glass substrates. To this end, several characterizations are necessary to observe and optimize the influence of various deposition factors (**Table III.3**).

***Table III.3.*** *The characterization techniques used in our work.*

| | |
|---|---|
| ***Structural properties*** | *X-ray diffractometer (XRD)* |
| | *Raman spectrometer* |
| ***Morphology*** | Scanning Electron Microscope (SEM) |
| ***Electrical properties*** | Four-point tester |
| ***Wettability*** | Contact angle with surface tensiometer |
| ***Optical properties*** | UV-Visible-NIR spectrometer |

#### III.6.1. X-ray Diffraction (DRX)

The fundamental concept of the X-ray diffraction (XRD) method was explained in Chapter II. We used a Philips X'PertMPD diffractometer (**Figure III.4**) at the CDTA, which is equipped with a Lynxeye linear detector and a copper cathode (with a wavelength of $\lambda_{cu\text{-}k\alpha}$ = 1.54 Å). The diffraction diagrams are collected under normal environmental conditions, covering an angular range of 20° to 80°. The θ-2θ configuration, also known as the "Bragg-Brentano" configuration, is employed for the characterization of our samples. Where the X-ray source remains stationary while the substrate holder and the detector can move. when the sample rotates by an angle θ, the detector, in turn, rotates by an angle 2θ and only collects the rays diffracted by the crystal planes (hkl) at an angle θ that satisfies Bragg's law (the principle is explained in more detail in **Chapter II**).


***Figure III.4.*** *Photograph of the diffractometer.*

### III.6.2. Raman spectroscopy

We used Raman spectroscopy to enhance the structural information of our films. We utilized the LabRam H-Revolution confocal micro-Raman spectrometer from Horiba Jobin Yvon (**Figure III.5**). This device provides high spatial resolution thanks to the combination of an optical microscope equipped with several objectives (×10, ×40, and ×100) and excellent spectral resolution.


***Figure III.5.*** *Photograph of the Raman device.*

### III.6.3. Scanning Electron Microscope (SEM)

During our study, we used scanning electron microscopy (SEM) to identify the morphology of our films. The microscope used is a Jeol JSM-6360LV device with an acceleration voltage ranging from 5kV to 15kV (**Figure III.6**).

***Figure III.6.*** *Photograph of the Scanning electron microscope (SEM) device.*

### III.6.4. Four-point probe technique

To determine the electrical resistance of our thin films, we performed tests using the four-point probe method. The equipment is a Keithley 2400C, which is a SourceMeter SMU Instrument with contact check. It has a voltage range of 200V, a current range of 1A, and a power rating of 20W (**Figure III-7**).


***Figure III.7.*** *Photograph of the four-point device.*

### III.6.5. Surface tensiometer

The wettability of our films was evaluated using an optical tensiometer to measure the Contact angle (**Figure III.8**). For all our films, the contact angle of a water droplet with our thin films was measured three times in three different spots of the sample's surface.

***Figure III.8.*** *Photograph of the optical tensiometer device.*

### III.6.6. UV-Visible-NIR mesurent

#### III.6.6.1. UV-Visible-NIR spectrometer

We used the Shimadzu spectrophotometer UV1280 to determine the transmittance of our layers. It is equipped with a single-beam system and offers a wavelength scanning range from 190 to 1100 nm (**Figure III.9**). The optical parameters were later calculated using Metaheuristic methods: Dragonfly Algorithm (DA) for the single layers and Particle swarm optimization (PSO) for the multilayers.

***Figure III.9.*** *Photograph of the UV1280 spectrophotometer*

### III.6.6.2. Metaheuristic methods

Metaheuristic optimization techniques are general heuristic algorithms applicable to a wide variety of problems, adapted to solving problems for which it is difficult to find a global optimum by classical methods [1]. These algorithms are created based on nature's inspiration and are designed to be flexible and easy to apply. In particular, metaheuristic algorithms excel at identifying subsets that lead to optimal solutions [2]. Metaheuristics appeared in the 1980s [3,4], the word “metaheuristic” is composed of two Greek words, the first means: “beyond or in a higher level” and the second means: “to find or discover” [2,5].

Metaheuristic optimization methods have the following common characteristics [6-9]:

- They are generally non-deterministic and they may not find the optimal solution, let alone prove the optimality of the solution found.
- They are inspired by analogies with physics (simulated annealing), biology (evolutionary algorithms), or even ethology (swarm intelligence).
- They are stochastic, which makes it possible to cope with the combinatorial explosion of possibilities, which limits trapping in local optima.
- They are originally dedicated to combinatorial problems, where the parameters can only take discrete values.
- They have the disadvantage of having several parameters to adjust, and the calculation time is high.

Generally, metaheuristic methods are classified into two categories [1,10,11]:

- Trajectory methods that construct a trajectory in the solution space and which only manipulate a single solution at each generation such as Simulated Annealing, Tabu Search, and Variable Neighborhood Search.
- Methods based on a population of solutions such as evolutionary algorithms (genetic algorithms GA, differential evolution DE, etc.) and swarm intelligence (particle swarm optimization PSO, biogeography-based optimization BBO, dragonfly algorithm DA, etc.).

### III.6.6.2.1. Dragonfly Algorithm (DA)

The Dragonfly Algorithm (DA) is a novel metaheuristic optimization technique developed by Seyedali Mrijalili in 2016 [12]. Inspired by nature, this algorithm is designed to solve efficiently a wide variety of optimization problems. Dragonflies encompass 3000 distinct species, the natural cycle of dragonflies, which consists of two phases (**Figure III.10**), is examined. The first phase, known as the static swarm (exploration phase), involves dragonflies flying in small groups to search for food. The second phase is known as the dynamic swarm (exploitation phase), in which large numbers of dragonflies cause trials to migrate in one direction over vast distances in search of suitable mating locations and distract enemies. In this category, dragonflies fly in large numbers over distances [13, 14].

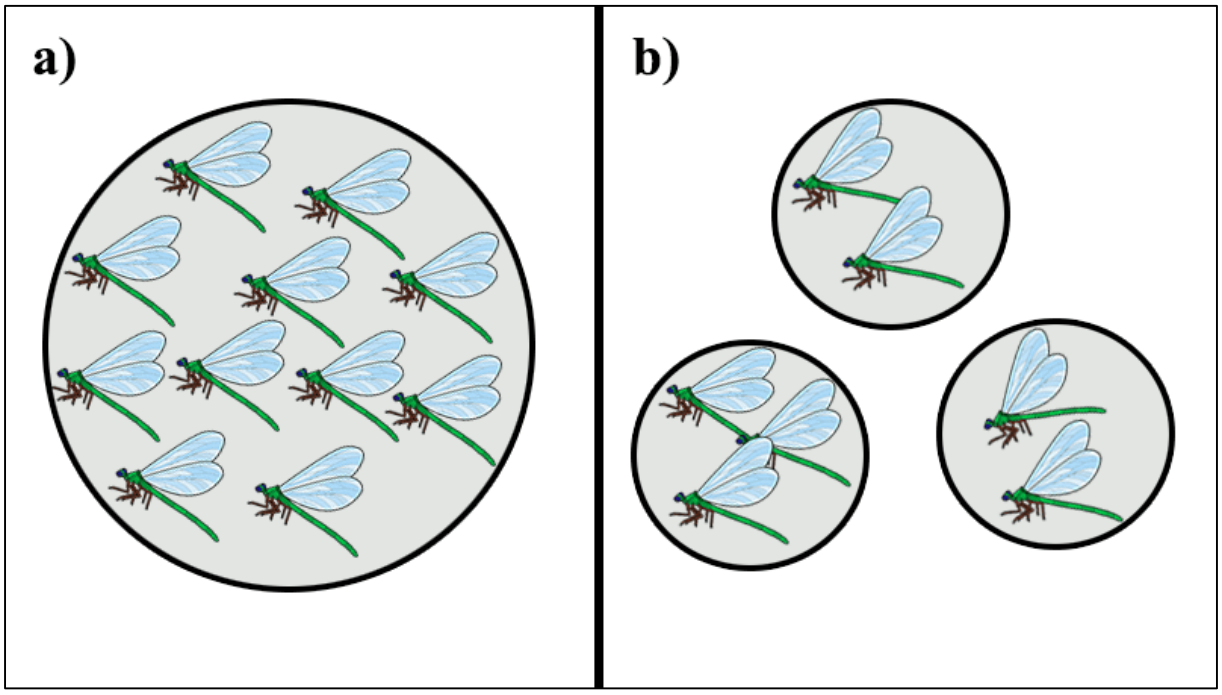


***Figure III.10. a)*** *dynamic swarming emigration behaviour of dragonflies in huge groups;* ***b)*** *Static swarming behaviour of the dragonfly, grouping in small groups.*

The performance of the dragonfly swarm is characterized by using five basic primitive behaviours of the dragonfly in nature (**Figure III.11**). The mathematical model of dragonfly behaviour is detailed as follows [12-14]:

**1) Separation:** represents the static collision avoidance that individuals follow to avoid collision with other individuals in the area, the mathematical interpretation is represented in the following equation:

$$S_i = -\sum_{j=1}^{N} X - X_j \quad \text{(III.1)}$$

where X: represents the position of the current individual, $X_j$: is the position of the jth neighboring individual, N: interprets the magnitude of the locality.

**2) Alignment:** it mentions a dragonfly and how it compares its velocity with other nearby resident dragonflies. **Equation (III.2)** is used to represent the alignment process.

$$A_i = \frac{\sum_{j=1}^{N} V_j}{N} \quad \text{(III.2)}$$

Where $Vj$: is the speed of dragonflies.

**3) Cohesion:** it is expressed in equation (3) and represents the tendency of individuals towards the center of the swarm group.

$$C_i = \frac{\sum_{j=1}^{N} X_j}{N} - X \quad \text{(III.3)}$$

**4) Attraction:** This refers to the movement of individuals searching for food. Equation (4) mathematically expresses the location of the food source.

$$F_i = X^+ - X \quad \text{(III.4)}$$

Where: $X^+$: refers to the location of the food source.

**5) Distraction:** expressed in equation (5), it refers to the trajectory of retreating and avoiding predators.

$$E_i = X^- - X \quad \text{(III.5)}$$

Where: $X^-$: is the location of the predator.

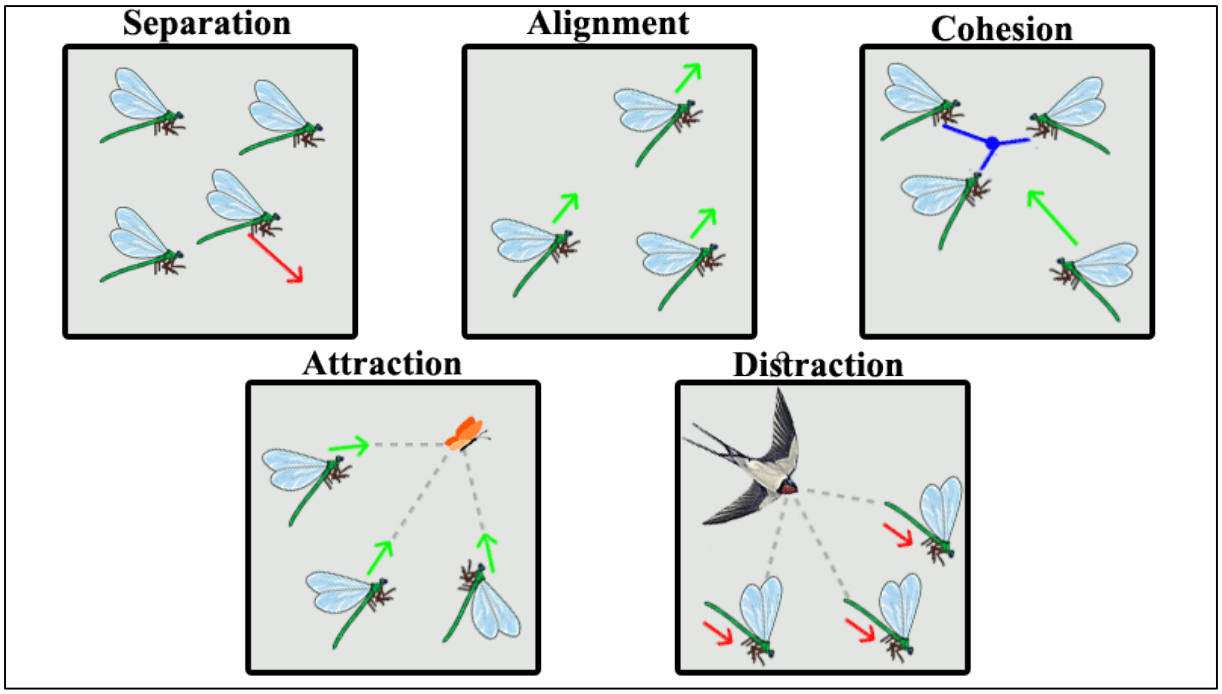


***Figure III.11.*** *Primitive corrective patterns between individuals in a swarm*

All of these five concepts make it possible to simulate the dynamic and static swarming behaviour of dragonflies. The DA algorithm is developed based on the PSO particle swarm optimization method, so there are two main vectors: the first is the step vector, which is similar to the velocity vector in PSO, and the second is the position vector. These two vectors can update the position of dragonflies in the search space and simulate their movement [13]. The location of the vectors ($\Delta X$) and ($X$) representing the direction of the dragonfly's movement is expressed in **equation (III.6)** [12].

$$\Delta X_{t+1} = (sS_I + aA_i + cC_i + fF_i + eE_i) + wX_t X \quad \text{(III.6)}$$

Where $\Delta Xt$: represents the step vector, $t$: the current iteration, and s, a, c, f, e, w: are weights of separation, alignment, cohesion, food, enemy, and inertia, respectively.

The location of the individual is expressed in **equation (III.7)** [12].

$$X_{t+1} = X_t + \Delta X_{t+1} \quad \text{(III.7)}$$

With t: the number of iterations.

During the last stage of optimization, the dragonfly joins together and forms a dynamic swarm to solve the global optimization. Using the Levy mechanism, the position of the dragonflies is updated, it is expressed in **equation (III.8)** [12].

$$X_{t+1} = X_t + levy(d) \cdot X_{t+1} \quad \text{(III.8)}$$

Where $X$: is the number of existing repetitions, $Lev(d)$: Represents the part of the dimension of each of the vectors in its position.

***Mathematical modeling***

The dragonfly algorithm begins the optimization process by creating a group of random solutions to solve a particular optimization problem. That is, the position and pitch vectors of the dragonflies are initialized to random values defined within the upper and lower limits of the different variables. In each iteration, the step and position of each dragonfly are updated using **equations (III.6)**, **(III.7)**, and **(III.8)**. This update continues iteratively until a global optimum for the optimization problem is found [12-14]. More details about the determinations of optical properties are presented in our paper [15]

**III.6.6.2.2. Particle swarm optimization (PSO)**

Since the beginning of time, human beings have had to satisfy their needs. To achieve this objective, man organized himself into groups to be able to overcome better the adversities that could arise. Initially, this was structured in small groups in its nomadic stage to form larger groups in its sedentary stage later, thus allowing the formation of great civilizations that led to man's domination over the other species [16]. However, this social behaviour does not only occur in humans. Smaller species have used this practice to solve the problems that nature can present to them. This form of organization has allowed these species to obtain food and survive attacks by larger species, among many other benefits. This social behaviour is a direct result of the process of species evolution and natural selection. It is clear to note that the individuals of these species that group in “herds” have a greater probability of surviving than those that do not, so natural selection will discard the members that work individually, giving way to these develop communication mechanisms that allow them to organize themselves in a better way [16-18].

Throughout history, man has solved optimization problems, but due to the scientific and technological boom presented in recent years, these problems are increasingly more complex, which is why They have had to devise better methods to solve them. Fortunately, the increase in computational resources today allows us to create algorithms that quickly and efficiently solve these complex optimization problems. An example worth imitating to solve optimization problems is precisely that of nature. Based on how some species solve complex

problems together, a range of algorithms emerge within evolutionary computing: swarm intelligence. Within this is particle swarm optimization (PSO), an algorithm developed by Kennedy and Eberhart in 1995, originally inspired by a set of birds searching for corn. Its objective is to produce computational intelligence using social interactions instead of only individual cognitive abilities [16-18]. Particle swarm optimization may have some similarities to genetic algorithms, but it is much simpler because it does not use mutation/crossover operators or pheromones. Instead, it uses the randomness of real numbers and global communication between particles in the test. In this sense, it is also easier to implement because there is no encoding or decoding of parameters into binary strings as in genetic algorithms, which can also use strings of real numbers [16].

This algorithm explores the space of an objective function by adjusting the trajectories of individual agents, called particles, because these trajectories form fragmented paths in a quasi-stochastic manner. The motion of a swarm particle includes two major components: a stochastic component and a deterministic component. Each particle is attracted to the position of the current global best g* and its own best position $xxii*$ in history while at the same time tending to move randomly [18, 19].

The components used by the PSO algorithm are [19]:

- Cognitive Component It constitutes that the particle has the memory of a previous position and a new one that is optimized. It is responsible for the particle tending to move to the position in which it has the best results; this coefficient $C_1$ is in the range of [0.2], and the coefficient $r_1$ has random values between 0 and 1.
- Social Component It is responsible for ensuring that the particle tends to move to the best position found by the algorithm, the value of the coefficient $C_2$ can be between 0 and 2, with 2 being the most recommended 2, $r_2$ is a vector that is between 0 and 1 that provides stochastic behavior to the particles.

## Conclusion

In this chapter, is divided into two parts. First, we have attempted to highlight the various materials, experimental conditions and procedures used for the deposition of single layers and multilayers of pure and doped ZnO. In the second part, we explained the metaheuristic methods utilized in this study.

## References

*[1] Abdel-Basset, M., Abdel-Fatah, L., & Sangaiah, A. K. (2018). Metaheuristic algorithms: A comprehensive review. Computational intelligence for multimedia big data on the cloud with engineering applications, 185-231.*

*[2] Yang, X. S. (2010). Engineering optimization: an introduction with metaheuristic applications. John Wiley & Sons.*

*[3] Sorensen, K., Sevaux, M., & Glover, F. (2017). A history of metaheuristics. arXiv preprint arXiv:1704.00853.*

*[4] Martí, R., Sevaux, M., & Sörensen, K. (2025). Fifty years of metaheuristics. European journal of operational research.-Amsterdam, 321(2), 345-362.*

*[5] Zäpfel, G., Braune, R., & Bögl, M. (2010). Metaheuristic search concepts: A tutorial with applications to production and logistics.*

*[6] Agrawal, P., Abutarboush, H. F., Ganesh, T., & Mohamed, A. W. (2021). Metaheuristic algorithms on feature selection: A survey of one decade of research (2009-2019). Ieee Access, 9, 26766-26791.*

*[7] Blum, C., & Roli, A. (2003). Metaheuristics in combinatorial optimization: Overview and conceptual comparison. ACM computing surveys (CSUR), 35(3), 268-308.*

*[8] Boussaïd, I., Lepagnot, J., & Siarry, P. (2013). A survey on optimization metaheuristics. Information sciences, 237, 82-117.*

*[9] Bandaru, S., & Deb, K. (2016). Metaheuristic techniques. In Decision sciences (pp. 709-766). CRC Press.*

*[10] Pham, D., & Karaboga, D. (2012). Intelligent optimisation techniques: genetic algorithms, tabu search, simulated annealing and neural networks. Springer Science & Business Media.*

*[11] Das, S., Abraham, A., & Konar, A. (2008). Particle swarm optimization and differential evolution algorithms: technical analysis, applications and hybridization perspectives. Advances of computational intelligence in industrial systems, 1-38.*

*[12] Mirjalili, S. (2016). Dragonfly algorithm: a new meta-heuristic optimization technique for solving single-objective, discrete, and multi-objective problems. Neural computing and applications, 27, 1053-1073.*

*[13] Filali, W., Amrani, R., Garoudja, E., Oussalah, S., Lekoui, F., Oukerimi, Z., ... & Henini, M. (2021). Optimal identification of Be-doped Al0. 29Ga0. 71As Schottky diode parameters using Dragonfly Algorithm: a thermal effect study. Superlattices and Microstructures, 160, 107085.*

*[14] Meraihi, Y., Ramdane-Cherif, A., Acheli, D., & Mahseur, M. (2020). Dragonfly algorithm: a comprehensive review and applications. Neural Computing and Applications, 32(21), 16625-16646.*

*[15] Settara, K., Lekoui, F., Akkari, H., Garoudja, E., Amrani, R., Filali, W., ... & Hassani, S. (2024). Optical parameters extraction of zinc oxide thin films doped with manganese using an innovative technique based on the dragonfly algorithm and their correlation to the structural properties. Journal of Ovonic Research, 20(3).*

*[16] Wang, D., Tan, D., & Liu, L. (2018). Particle swarm optimization algorithm: an overview. Soft computing, 22(2), 387-408.*

*[17] Garcia-Gonzalo, E., & Fernandez-Martinez, J. L. (2012). A brief historical review of particle swarm optimization (PSO). Journal of Bioinformatics and Intelligent Control, 1(1), 3-16.*

*[18] Shami, T. M., El-Saleh, A. A., Alswaitti, M., Al-Tashi, Q., Summakieh, M. A., & Mirjalili, S. (2022). Particle swarm optimization: A comprehensive survey. Ieee Access, 10, 10031-10061.*

*[19] Marini, F., & Walczak, B. (2015). Particle swarm optimization (PSO). A tutorial. Chemometrics and Intelligent Laboratory Systems, 149, 153-165.*

# Results and discussion

## Introduction

Transparent Conductive Oxides (TCOs) are the most interesting materials from a property perspective compared to other materials [1]. Their dual properties, electrical conductivity, and transparency in the visible range make them ideal materials for applications in photovoltaics and optoelectronics [2,3]. However, combining these two properties is a priori contradictory; a transparent material is not conductive, and a conductive material can not be transparent. To overcome this problem, we doped ZnO thin films with low percentages of Mn. Another problem is the optical and electrical losses in thin films. To solve this, a sandwich structure of oxide/metal/oxide multilayer structure (ZnO/Ag/ZnO and Mn:ZnO/Ag/ZnO:Mn) is introduced. In this chapter, we have two parts:

*Part I:* Where we will investigate the effect of Mn on the structure, morphology, and optical properties of a single layer of ZnO thin film.

*Part II:* In this part, we investigate the impact of multilayering on the electrical properties of our multilayers as well as its effect on the structure, optical properties, and wettability.

# Part I

## Studying the effect of doping on ZnO thin films

### IV.I.1. X-ray diffraction (DRX)

X-ray diffraction patterns of ZnO and Mn-doped ZnO are shown in **Figure IV.1**. It is evident from the XRD data that our samples exhibit a singular phase. For the non-annealed sample (as deposited sample), we notice five peaks that belong to Zn metal (ICCD No.001-1238) corresponding to the plans (002), (100), (101), (102), and (110), respectively. No additional peaks indicate the presence of ZnO, suggesting that the oxidation of Zn occurs after the thermal annealing. The absence of the zinc oxide phase can be explained by the fact that ZnO molecules disperse during evaporation, which results in the formation of zinc atoms and oxygen gas. These two gases will be carried out primarily by the pumping system, thereby preventing the development of the ZnO phase [4]. As for the annealed samples, according to the powder diffraction standard card (ICCD No.001-1136), the peaks with high intensities corresponding to the planes (100), (002), and (101) and the peaks with lower intensities (102), (110), (103) and (112) indicate the hexagonal Wurtzite structure of ZnO. This observation suggests that the ZnO mesh was disturbed when the Mn concentration was raised. It's likely that throughout the annealing process, Mn atoms operate as barriers (traps or dispersion centers) that prevent ZnO from developing, causing the film's crystallinity to deteriorate and the peak's intensity to drop. Many research works [5, 6] have reported on this fact. In addition, the examination of the XRD patterns reveals that the peaks of Mn-doped films are somewhat displaced to a lower angle than those of the undoped ZnO films. The structure's micro-strain from vacancies, stacking faults, and interstitials may have caused this shift [7]. However, there are no peaks that identify Mn. This suggests that the Mn has substituted the Zn site without changing the Wurtzite structure.

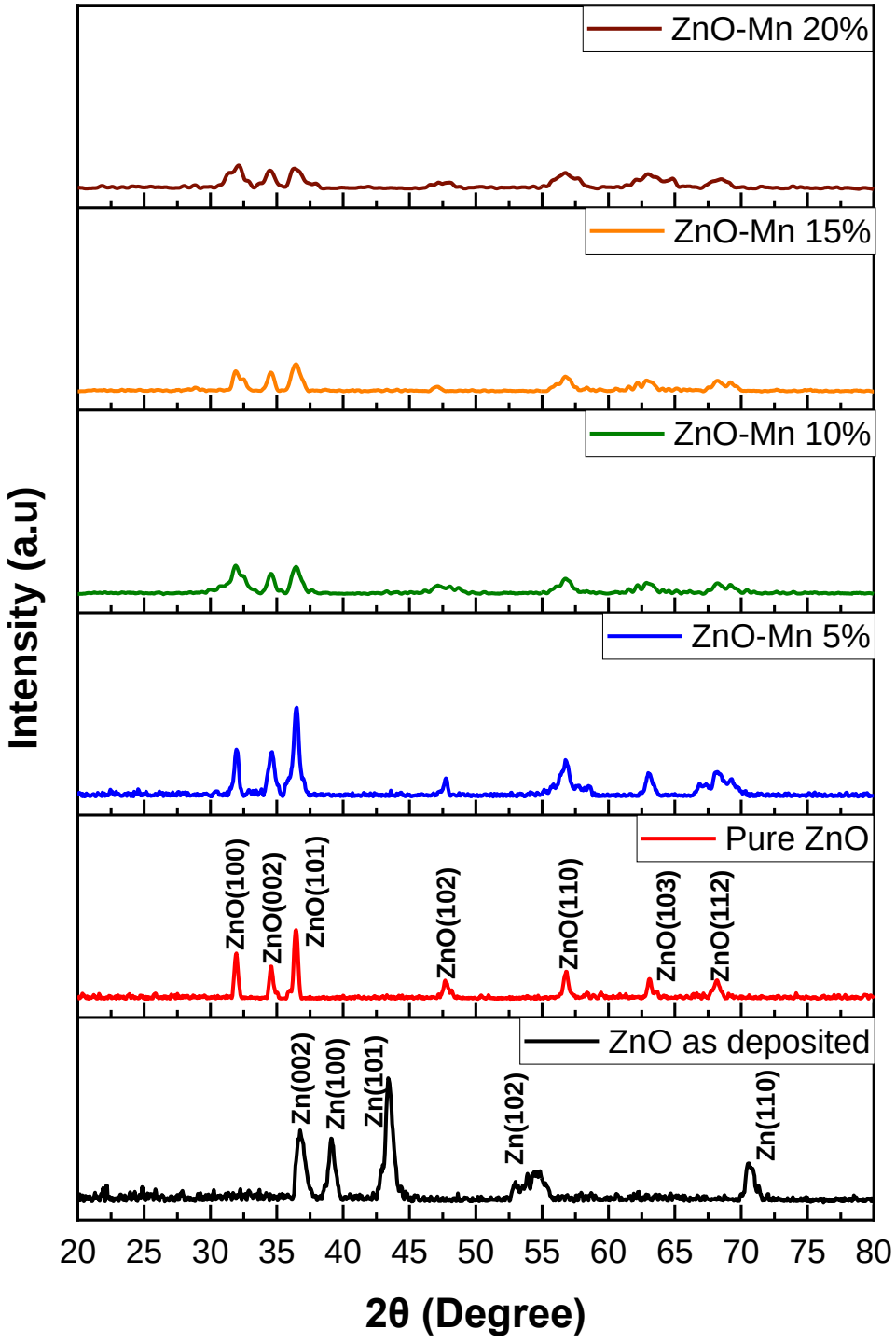


***Figure IV.1.*** *XRD patterns of ZnO and Mn-doped ZnO thin films.*

To understand the change in the physical properties of our layers, it is better to identify the modification of these structural aspects. The values of the lattice parameters a and c were calculated using [8]:

$$a = \frac{\lambda}{sin\theta_{hkl}\sqrt{3}} \quad \text{(IV.1)}$$

$$c = \frac{\lambda}{sin\theta_{hkl}} \quad \text{(IV.2)}$$

Where λ: the x-ray wavelength, $\theta_{hkl}$: the diffraction angle, and hkl: are Miller indices.

The crystallite size D, microstrain τ, and dislocation density δ (**Table IV.1**)were determined by using the following formulas [9]:

$$D = \frac{0.9\lambda}{FWHMcos\theta_{hkl}} \quad \text{(IV.3)}$$

$$\tau = \frac{FWHM}{4tan\theta_{hkl}} \quad \text{(IV.4)}$$

$$\delta = \frac{1}{D^2} \quad \text{(IV.5)}$$

***Table IV.1.*** *Crystallites size D, FWHM, microstrain τ, dislocation density δ, and lattice parameters.*

| | *D (nm)* | *FWHM (deg)* | *T* | *δ ($nm^{-2}$)* | *a (nm)* | *c (nm)* |
|---|---|---|---|---|---|---|
| *Pure ZnO* | 24.26 | 0.3447 | 0.0046 | 0.0017 | 0.3214 | 0.5247 |
| *Mn:ZnO(5 wt.-%)* | 15.61 | 0.5359 | 0.0071 | 0.0041 | 0.3213 | 0.5249 |
| *Mn:ZnO(10 wt.-%)* | 10.64 | 0.7855 | 0.0104 | 0.0088 | 0.3220 | 0.5256 |
| *Mn:ZnO(15 wt.-%)* | 10.08 | 0.8290 | 0.0110 | 0.0098 | 0.3224 | 0.5259 |
| *Mn:ZnO(20 wt.-%)* | 8.93 | 0.9361 | 0.0125 | 0.0125 | 0.3228 | 0.5265 |

The lattice parameters of our samples exhibited minimal variation upon incorporating various amounts of Mn. This can be attributed to the proximity in radius between the Mn ion (0.66 Å) and the Zn ion (0.60 Å), facilitating the substitution of Zn atoms with Mn atoms. The variation in 'c' axis values starts with an insignificant increase at a doping level of 5 wt.-% Mn, then slightly rises with the addition of Mn to reach 0.5265 nm (**Figure IV.2a**). This value is greater than the theoretical pure ZnO (0.5205 nm), meaning that ZnO sheets undergo compressive forces in the c-axis direction [10].

According to **Figure IV.2b**, adding Mn to the thin films leads to an increase in the full width at half-maximum (FWHM) due to the reduction in crystallite size produced by doping. The pure ZnO films exhibit the lowest FWHM value, suggesting the highest level of crystallinity. The widening of the diffraction peaks is caused by the increase in strain, an increase in lattice defects, and dislocation density, which leads to a reduction in crystallite size, illustrating the impact of the Mn addition [11].

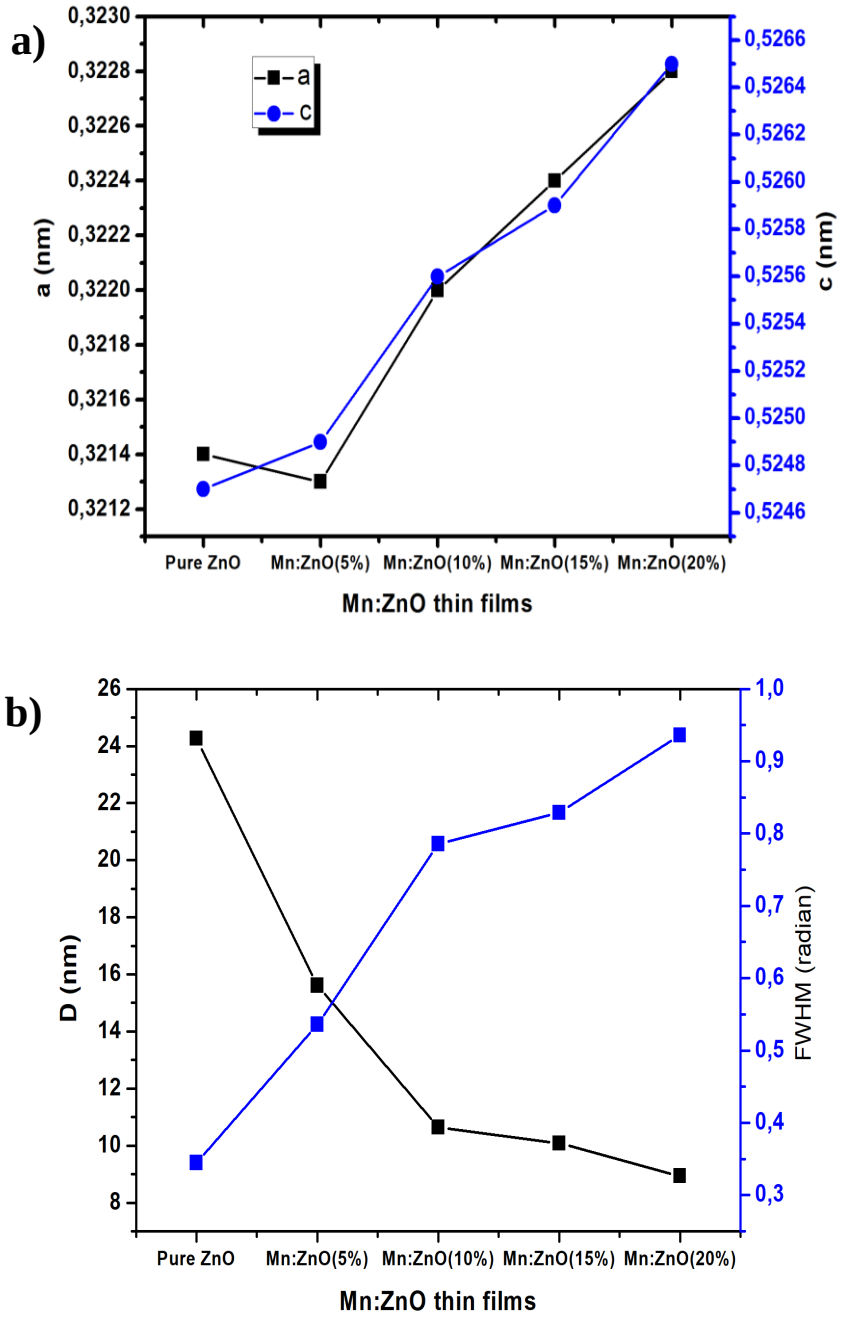


***Figure IV.2.*** *Variation of* ***a)*** *lattice parameters 'a' and 'c'* ***b)*** *FWHM, crystallites size D of ZnO mesh as a function of Mn content.*

### IV.I.2. Raman analysis

The vibration properties of the hexagonal wurtzite structure of the undoped and doped ZnO layers were investigated using the Raman scattering technique; the results are shown in **Figure IV.3**. As one can see, all the samples have the $A_1$(LO) vibration mode at ≈572 $cm^{-1}$ for Mn:ZnO films and 569 $cm^{-1}$ for pure ZnO. The $A_1$ longitudinal optical phonon in the wurtzite structure of ZnO is polarised parallel to the c-axis; this vibration mode gives the oxidation state of the films. In doped films, Mn atoms are incorporated into the ZnO host lattice, whereas in pure ZnO films, incomplete oxidation results in the incorporation of Zn atoms into the ZnO mesh, creating self-doping [12].

Local vibration modes (LVM) in the Raman spectra may appear as the dopant is added to the mesh. The disruption of the crystal's translational symmetry by impurity-induced defects is one proposed physical basis for understanding LVM. Due to the wave vector's loss of conservation, phonon scattering with wave vectors far from the Brillouin zone occurs [13]. Due to the abundance of Mn atoms in the ZnO, LVM modes can be found clearly for Mn:ZnO (15 wt.-% and 20 wt.-% Mn) samples. However, the disappearance of this vibration mode can be noticed in pure ZnO films. The rest of the detected peaks for the Mn:ZnO films (887 and 847 $cm^{-1}$) may be attributed to the molecules with Mn [14]. $A_1$(LO)+$E_2$(Low) mode for the high-doped films is related to poly-phonon scattering [15]. Vibration modes at 706 $cm^{-1}$ and 900 $cm^{-1}$ for pure ZnO samples are given the $A_1$ symmetry of ZnO processes that combine LA+TO phonons [16].

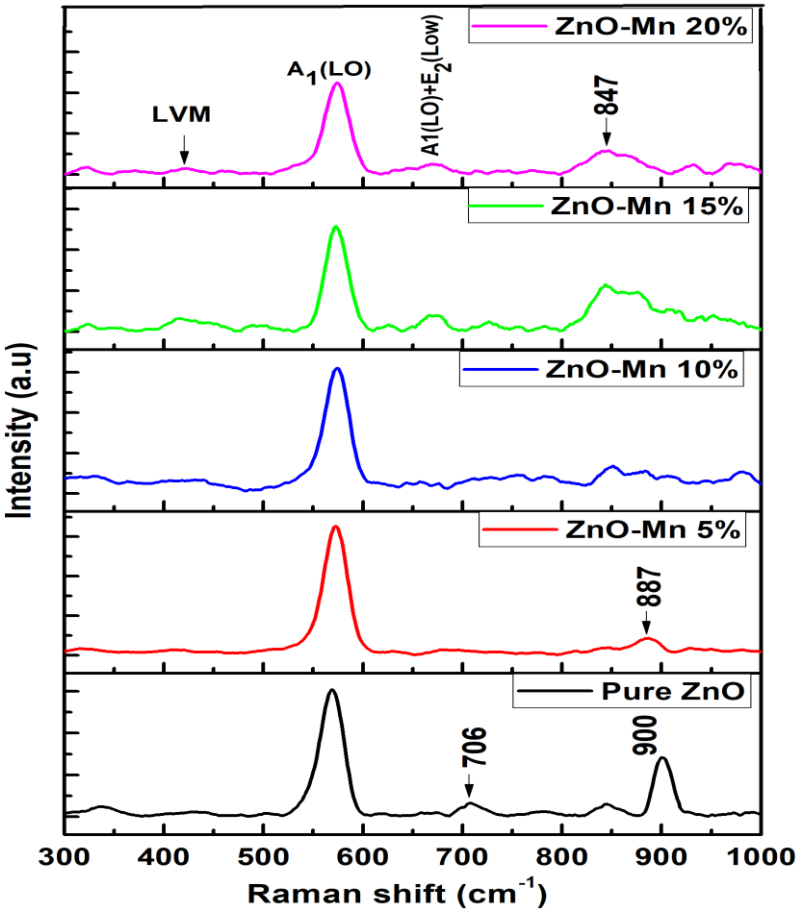


***Figure IV.3.*** *Raman spectra for the ZnO and Mn-doped ZnO thin films.*

### IV.I.3. Surface morphology

The SEM analysis was used to characterize the surface morphology of the non-doped and doped layers. The results are presented in **Figure IV.4 (a-e)**. The electron micrographs indicate that all substrates are completely coated with a thin layer, exhibiting a non-uniform surface morphology. The ZnO film exhibits unevenly distributed spherical particle agglomerations over the substrate, with an average diameter of 5.36 µm. Mn doping modifies the morphology, resulting in a more uniform structure. The agglomerations are closely packed, with a grain size significantly smaller than that of the non-doped films.

Observations revealed the presence of pits and holes in ZnO clusters, indicating the release of gases during heat evaporation due to their impactful nature. The chemical composition was examined utilizing Energy Dispersive X-ray Spectroscopy (EDX). It confirms the presence of Zn, Mn, and O atoms. There are pics indicating the Si corresponding to the glass substrate.

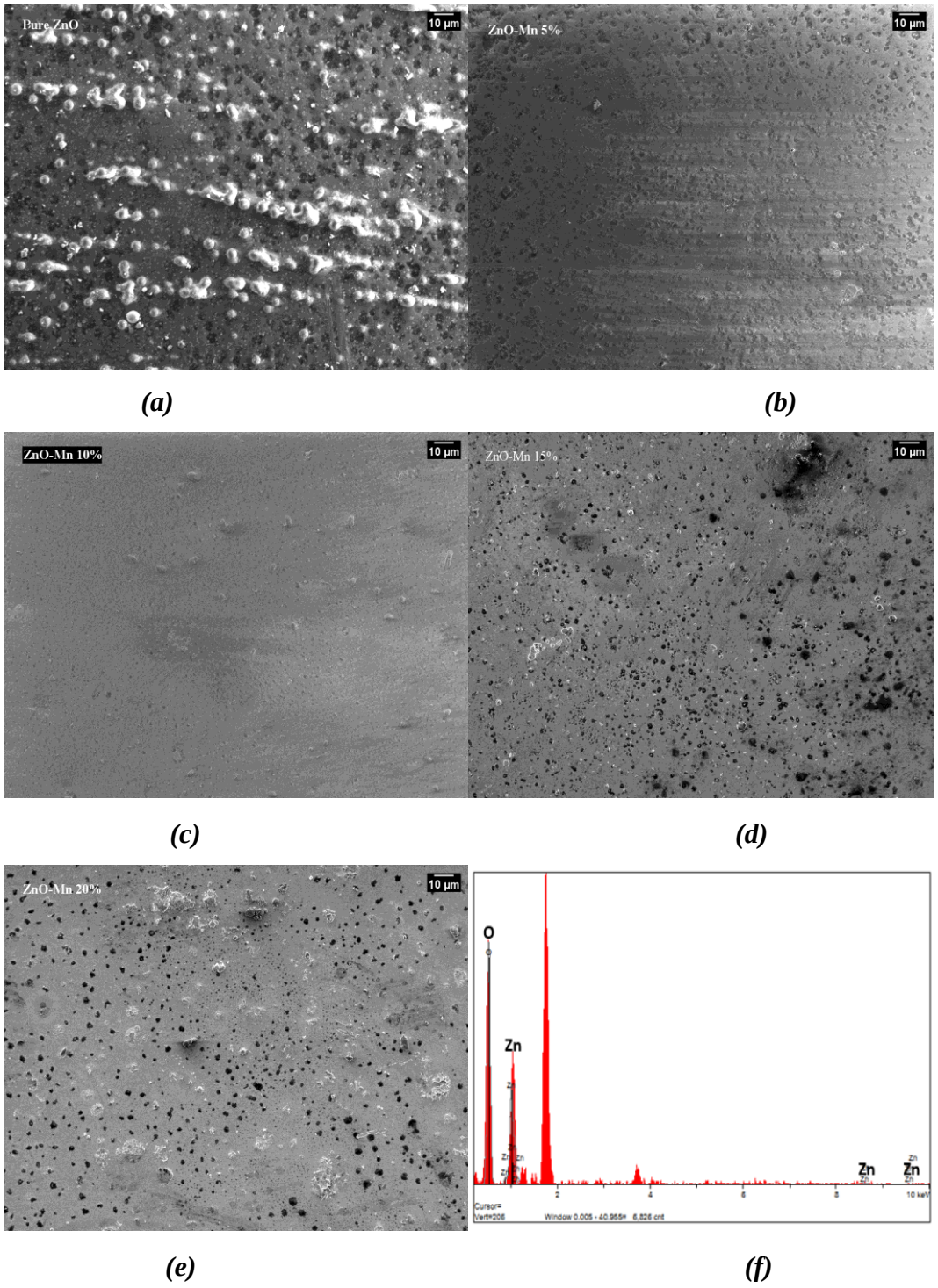


***Figure IV.4.*** *SEM images of ZnO and Mn-doped ZnO thin films, (a) pure ZnO, (b) ZnO-Mn 5%, (c) ZnO-Mn 10%, (d) ZnO-Mn 15%, (e) ZnO-Mn 20% and (f) EDX results for 20% doping.*

### IV.I.4. Optical properties

**Figure IV.5** shows the optical transmission spectra of our samples recorded in the wavelength region of 250-800 nm. The thickness of the layers is calculated using the DA algorithm, around 120 nm. All samples are transparent in the visible range, with the highest transmission of 83.1% for pure ZnO film. Adding more Mn leads to a decrease in the optical transmission, down to 69.5% for Mn:ZnO (20 wt.-%Mn), possibly due to the light loss induced by oxygen vacancies and diffusion at grain boundaries [17]. Another factor contributing to this phenomenon is the reduction in optical diffusion [6], which is linked to a decrease in grain size and an increase in grain boundary density. The results align perfectly with the XRD analysis section, and the grain size decreases as the Mn content increases.

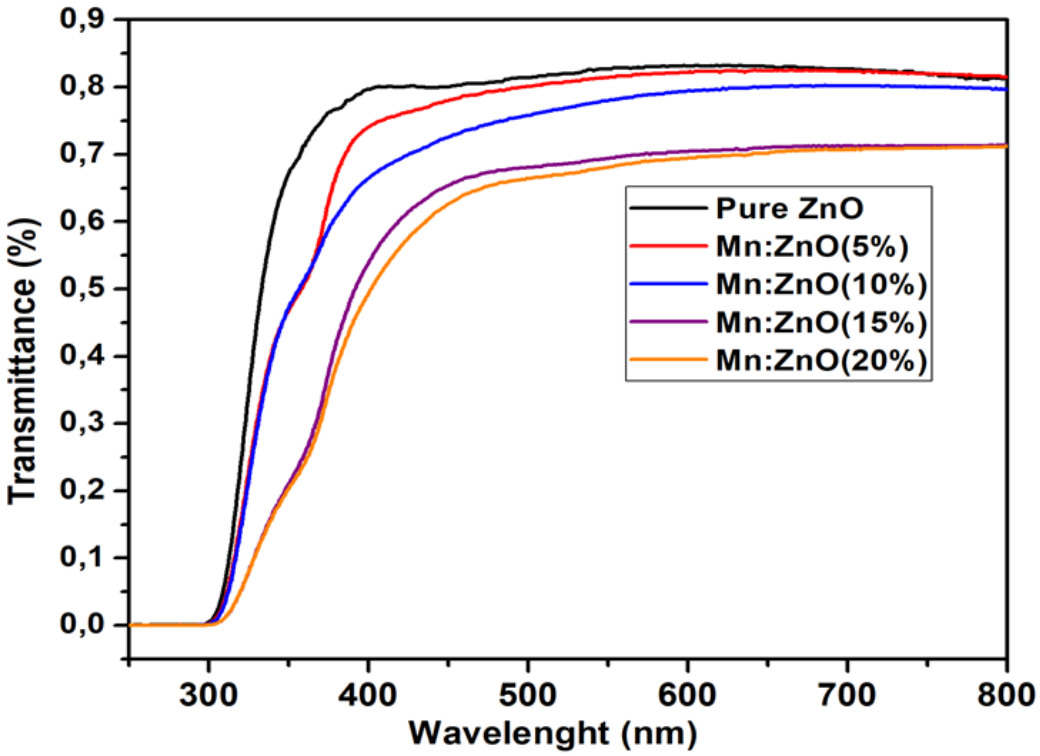


***Figure IV.5.*** *Optical transmittance spectra of ZnO and Mn-doped ZnO thin films.*

The consistency between the measured and estimated transmittance is apparent for all samples. **Figure IV.6** presents the case of the sample with 20 wt.-% Mn doping as an example. It confirms that the Dragonfly algorithm successfully determined the optical parameters of our films. The measured transmittance and the estimated one are almost identical, and the estimated root mean square is around 0.00145.

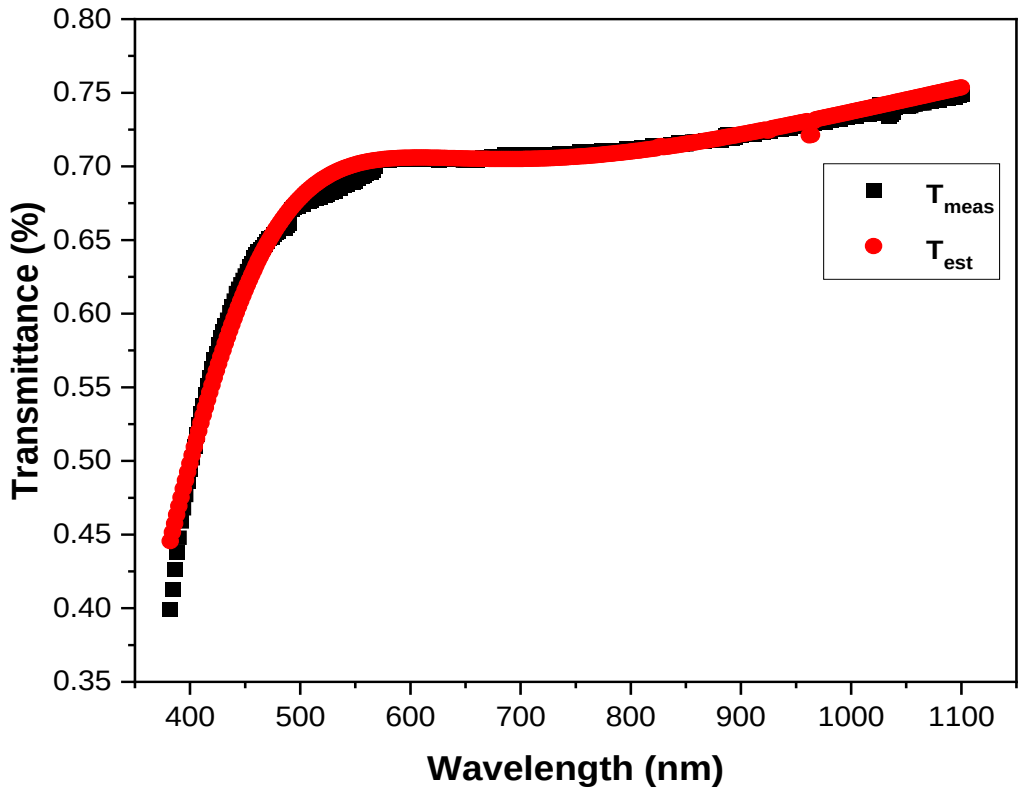


***Figure IV.6.*** *Measured and estimated transmittance for 20wt.-% Mn-doped ZnO.*

The efficiency of the DA method in analyzing the transmittance spectrum of Mn-doped ZnO thin films has been demonstrated. A comprehensive explanation, accompanied by illustrations, will be provided for the sample that contains a 20 wt.-% Mn doping concentration. Furthermore, as stated in Chapter 2, the user can modify a number of control settings for the DA algorithm. The parameters for this study were chosen based on empirical evidence utilizing a trial-and-error approach. This suggests that the efficacy of the DA algorithm has been assessed across several values, and only the most optimal ones are selected. **Table IV.2** presents a comprehensive summary of the configuration parameters of the Dragonfly Algorithm. The variation ranges of each parameter are depicted in **Table IV.3**.

***Table IV.2.*** *The setting parameters of DA.*

| ***Parameter*** | ***Value*** |
|---|---|
| *Population size* | 80 |
| *Number of iterations* | 200 |
| *Dimension* | 5 |
| *Separation weight* | 0.1 |
| *Alignment weight* | 0.1 |
| *Cohesion weight* | 0.7 |
| *Food factor* | 1 |
| *Enemies factor* | 1 |

***Table IV.3.*** *Variation ranges of each parameter.*

| ***Parameter*** | ***Variation range*** |
|---|---|
| $\alpha_1$ | [1 – 3] |
| $\beta_1$ | [$10^4$ – $10^6$] |
| $\alpha_2$ | [$10^{-5}$ – $10^{-2}$] |
| $\beta_2$ | [$10^3$ – $10^5$] |
| *D* | [60 – 400] |

For instance, the obtained optimal parameters and reached RMSE for the Mn:ZnO (20wt.-%) are given in **Table IV.4**.

***Table IV.4.*** *The obtained results for Mn:ZnO (20wt.-%).*

| *Parameters* | $\alpha_1^*$ | $\beta_1^*$ | $\alpha_2^*$ | $\beta_2^*$ | $d^*$ | $RMSE$ |
|---|---|---|---|---|---|---|
| *Value* | 2.05 | $7.17\times10^{+04}$ | $3.77\times10^{-4}$ | $1.64\times10^{+4}$ | 105 | $1.45\times10^{-03}$ |

In addition, the results presented in **Table IV.4** clearly show the remarkable efficiency of the DA algorithm in reliably determining both the optical film thickness and Cauchy dispersion parameters. The low value of RMSE ($1.45\times10^{-03}$) shows the excellent precision achieved by the approach.

The refractive index can be rewritten as follows using the **Table IV.4** parameters:

$$n(\lambda) = 2.05 + \frac{7.17 \times 10^{+4}}{\lambda^2} \quad \text{(IV.6)}$$

This equation can be used to extrapolate the complete range of wavelengths and obtain the value of n. The estimated values of n are shown in **Figure IV.7**.

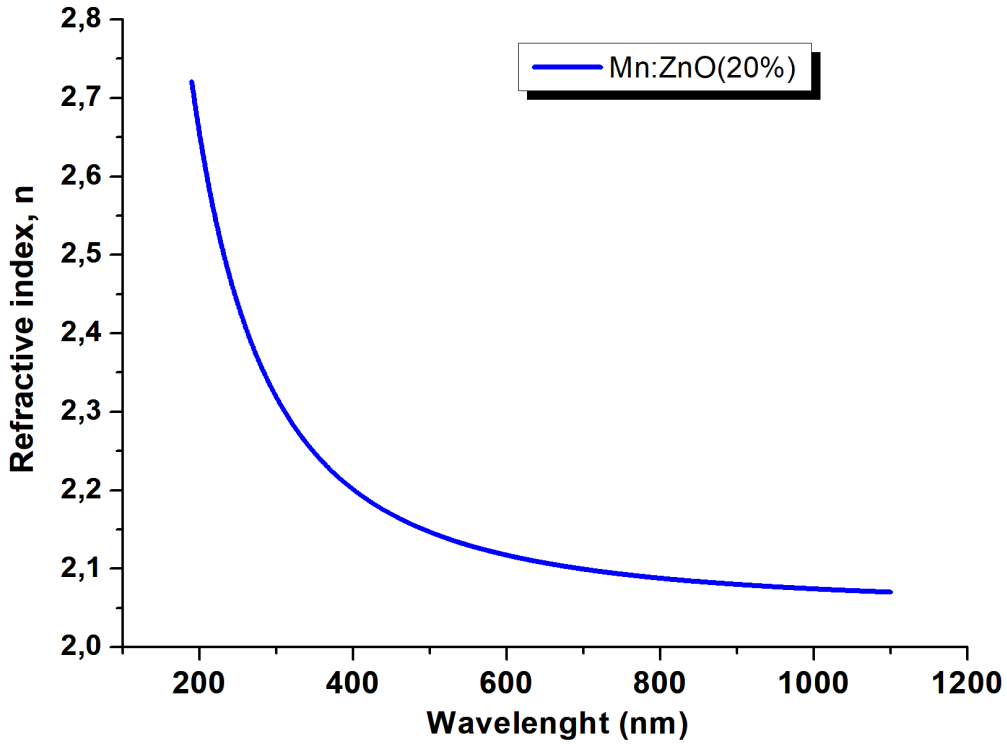


***Figure IV.7.*** *The dispersion of refractive index n for the whole wavelength range.*

The static refractive index can be calculated by setting the Cauchy relation model's variable to "tends towards infinity" in equation IV.7. The measured values for pure ZnO and Mn:ZnO samples with (5, 10, 15 and 20 wt.-%) Mn are 1.76, 1.90, 1.92, 2.112 and 2.17, respectively. With a rise in Mn doping, the refractive index at λ= 600 nm is found to be 1.785, 1.925, 1.952, 2.142, and 2.197. An increase in the refractive index with the increase of Mn amount was recorded.

Not many studies are reported in the literature on the effect of Mn percentage on the refractive index of ZnO. However, the same results were reported by Shaaban et al. [18]. The result of Mn incorporation explains the increase in polarisation. P. Singh and R. Kumar [19] reported similar results for Er-doped ZnO films. They found that erbium concentration increases the material's refractive index because of its polarizability power. Erbium ions ($Er^{3+}$) with the emptiest outer orbital will bring the material back toward linear

polarizability. The same can be said for Mn and its influence on Mn:ZnO thin films. For the calculated extinction coefficient based on the values of the absorption coefficient α. The values in **Table IV.5** are practically the same for the layers not doped and doped at 5 and 10 wt.-%. However, the value of k increases when the doping becomes important (15 and 20 wt.-%).

**Figure IV.8** shows plots of $(\alpha h\upsilon)^2$ versus $(h\upsilon)$. The thin films' optical band gap was extracted by extrapolating the linear region of the resulting curve to $(\alpha h\nu)^2 = 0$. It is calculated using the following formula [20, 21]:

$$\alpha h\upsilon = A\sqrt{h\upsilon - Eg} \qquad \text{(IV.7)}$$

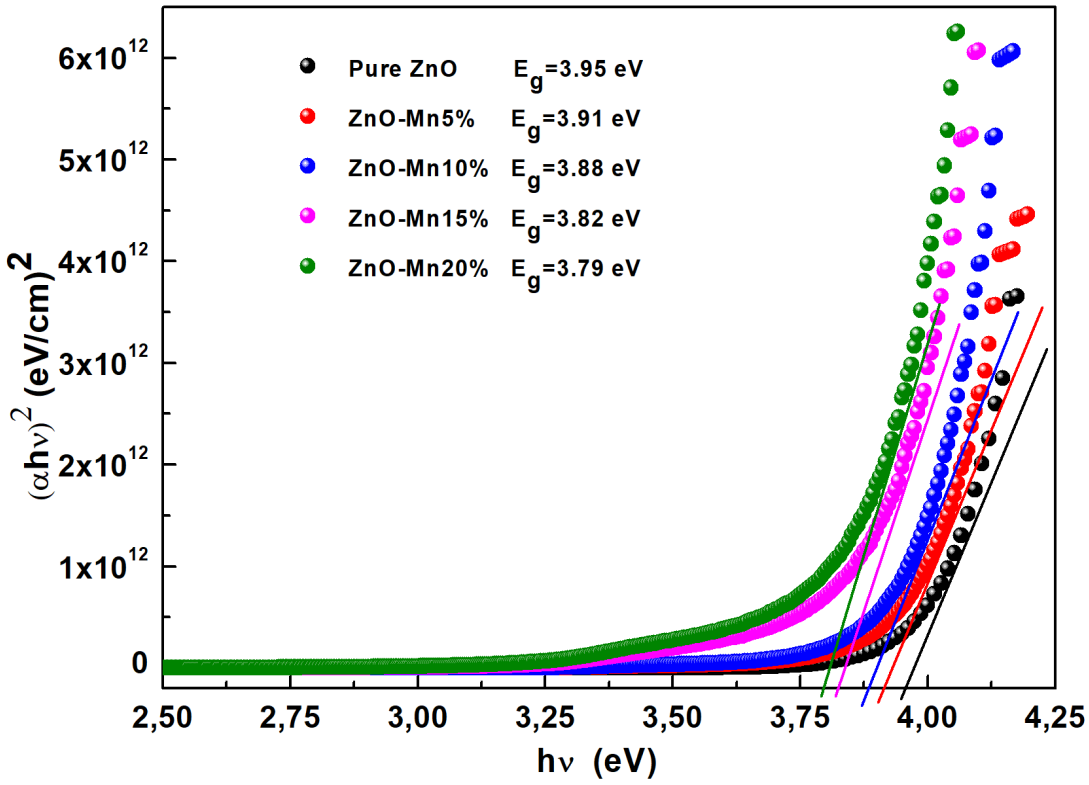


***Figure IV.8.*** *The plots of $(\alpha h\nu)^2$ as function of photon energy of non-doped and Mn-doped ZnO thin films.*

The optical band gap of ZnO film is 3.95 eV; it slightly decreases after doping with Mn to reach 3.79 eV at 20 wt.-% Mn. Doping ZnO with different percentages of Mn lowers the band gap. This has been theoretically attributed to the exchange interaction between the electrons of the sp orbital of ZnO and Mn d orbital [22].On the other hand, many researchers

explain the change in band gap $E_g$ by the strains in semiconductor films. It can be explained by the following empirical expression [23]:

$$E_g = 3.28 - 0.045\varepsilon_z \quad \text{(IV.8)}$$

The strains ($\varepsilon_z$) values can be calculated based on c-axis values determined in XRD section and using this formula [24]:

$$\varepsilon_z = \left(\frac{c - c_0}{c_c}\right) \quad \text{(IV.9)}$$

According to equation IV.8, the film's band gap will increase for negative strain and decrease for positive strain. The *εz* values are +0.0080, +0.0084, +0.0098, 0.0103, and 0.0115 for pure ZnO and Mn:ZnO films (5, 10, 15, and 20 wt.-%), respectively. Since *εz* has positive values in our case, the Eg rises (**Figure IV.9**). All the results are summarised in **Table IV.5**.

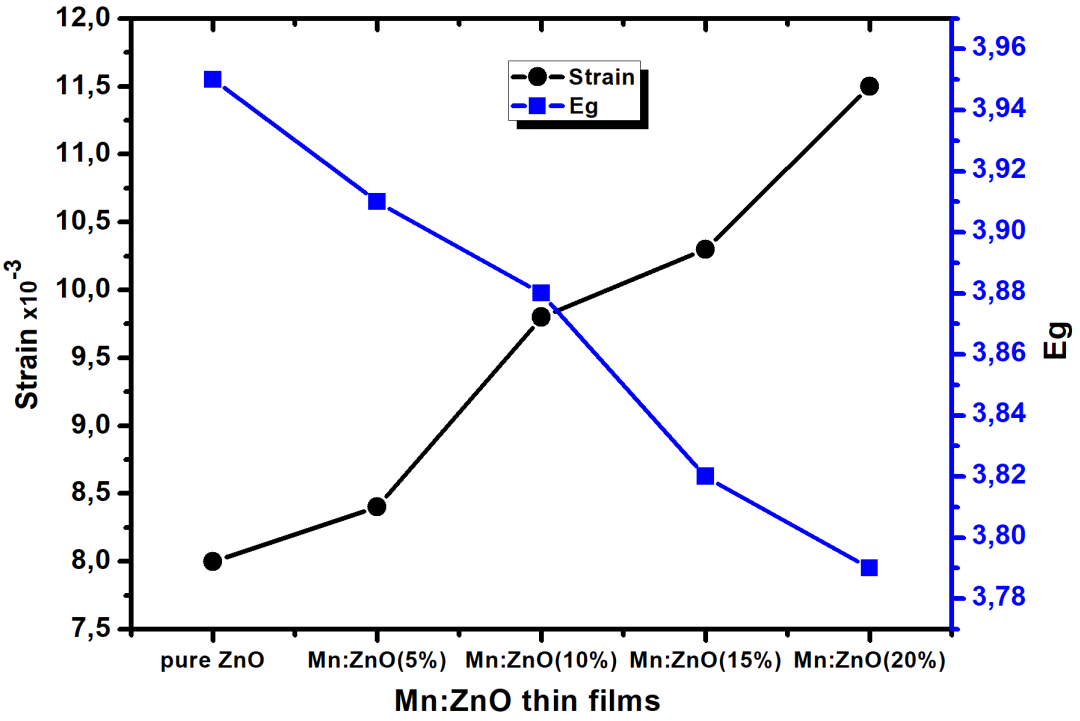


***Figure IV.9.*** *Band gap $E_g$ and strain $\varepsilon_z$ variation as a function of Mn doping concentration.*

***Table IV.5.*** *Band gap (Eg), Transmittance (T), refractive index (n), and extinction coefficient (k) of the non-doped and doped samples.*

| | $Eg$ (eV) | $T$ (%) ($\lambda$=600) | $N$ ($\lambda$=600) | $n_0$ (static) | $k$ ($\lambda$=600) | $k_0$ (static) |
|---|---|---|---|---|---|---|
| *Pure ZnO* | 3.95 | 83.1 | 1.785 | 1.760 | 0.013 | 0.039 |
| *Mn:ZnO (5wt.-%)* | 3.91 | 82.2 | 1.925 | 1.900 | 0.018 | 0.040 |
| *Mn:ZnO (10wt.-%)* | 3.88 | 79.5 | 1.952 | 1.920 | 0.015 | 0.035 |
| *Mn:ZnO (15wt.-%)* | 3.82 | 70.4 | 2.142 | 2.112 | 0.072 | 0.084 |
| *Mn:ZnO (20wt.-%)* | 3.79 | 69.5 | 2.197 | 2.170 | 0.064 | 0.057 |

# Part II

## Studying the effect of multilayering

### IV.II.1. X-Ray Diffraction (XRD)

Grazing diffraction patterns of ZnO/Ag/ZnO and Mn:ZnO/Ag/ZnO:Mn (5, 10, 15 and 20 wt.-% Mn) are presented in (**Figure IV.10**). We notice five peaks corresponding to the planes (100), (002), (101), (110), and (103) that indicate the hexagonal Wurtzite structure of ZnO according to the powder diffraction standard card No.01-079-2205. Three peaks correspond to the cubic structure of Ag with the planes respectively (111), (200), and (220) (standard card No.00-001-1164). The diffraction spectra of all samples exhibit a high peak at an angle of approximately 30.45°, corresponding to the (100) crystal plane. This peak indicates the preferred orientation of the fabricated ZnO thin films. Similar to the single layers, no peak indicates the existence of Mn. Lattice parameters barely changed with the incorporation of Mn from a=3.3340 Å and c=5.5454 Å to a=3.3354 Å and c=5.547 Å. It is clear that it increases after multilayering from a=3.214 Å and c=5.247 Å to a=3.340 Å and c=5.545 Å

The Full Width at Half-Maximum (FWHM) of the most intense peak (2θ=30.45°) increases after adding a layer of Ag and a second layer from 0.3447° to the highest value 0.9923° for Mn:ZnO/Ag/ZnO: Mn (5 wt.-% Mn) than decreases after adding more Mn to reach a minimum value of 0.2082°. The XRD patterns show a drop in peak intensities, particularly the intensity of the (101) peak, at the lowest doping concentrations (5 wt-. % Mn). Yet, the intensity of the same peak increases at other Mn percentages. This is due to the variance in crystallite size, which can be measured by employing the Scherrer formula (equation IV.3) in part I. For 5 wt-. % Mn:ZnO/Ag/ZnO:Mn, the drop in the size of the crystallite (as shown in **Table IV.6**) is a result of strain generated by the inclusion of manganese ions into zinc ion sites, leading to a decrease in the intensity of diffraction peaks. This phenomenon has also been seen in previous research [25,26]. However, it is evident that with the increase of Mn amount, the opposite phenomenon takes place. The observed Changes in peak intensity demonstrate the influence of doping concentration on the surface texture of our samples [27] as well as the effect of the surface morphology of the Ag layer [28]; in other words, the Ag crystallite size (**Table IV.7**).

The dislocation density (δ) indicates the quality of our multilayers and the presence of defects in certain areas. The dislocation density can be estimated using Williamson and Smallman's formula (equation 5) for the (100) plane by obtaining knowledge of the crystallite size. The microstrain (ε) of the films is determined using the **equation IV.4**.

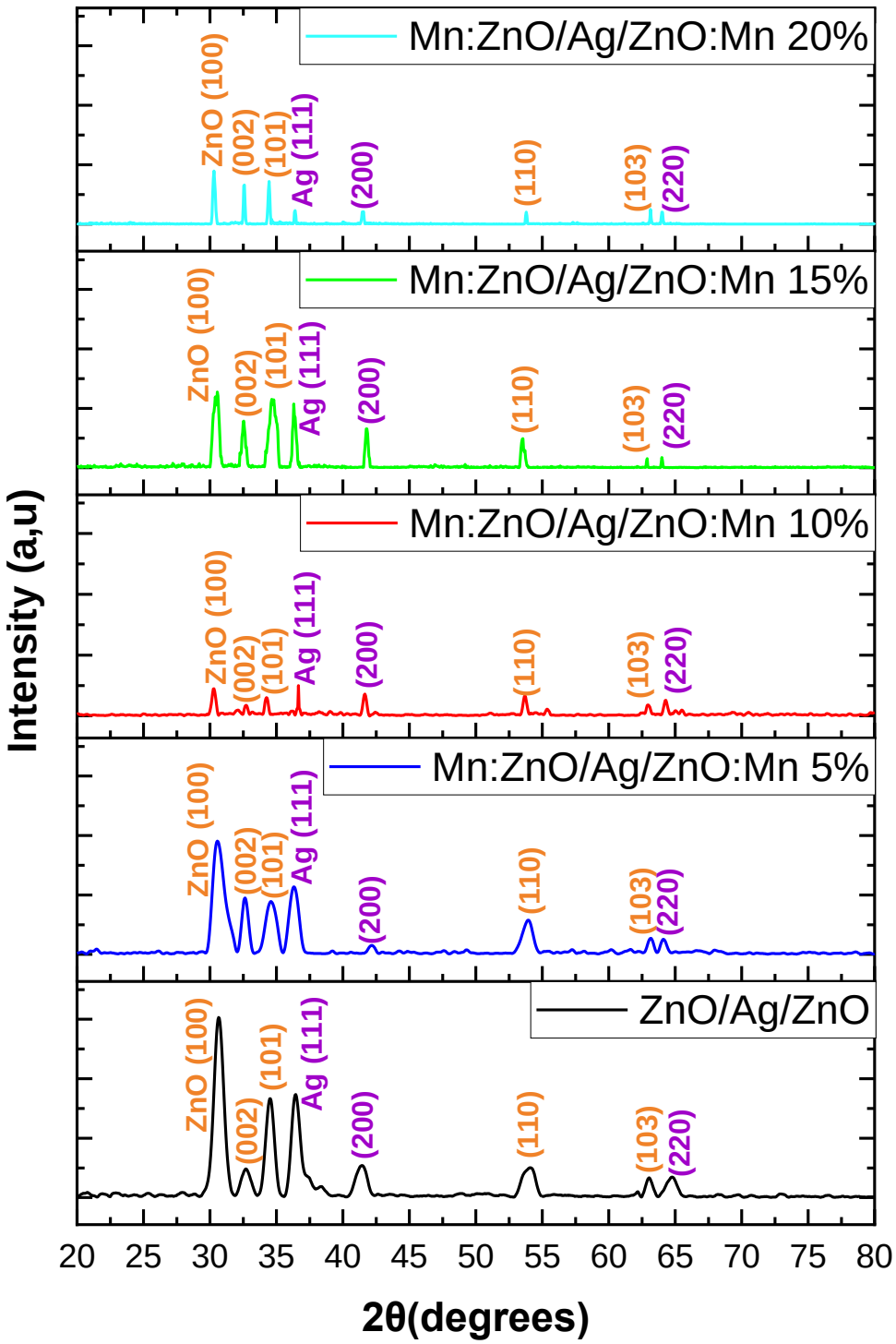


***Figure IV.10.*** *XRD patterns of ZnO/Ag/ZnO and Mn:ZnO/Ag/ZnO:Mn multilayers.*

***Table. IV.6.*** *Crystallites size D, FWHM, microstrain τ, dislocation density δ, and lattice parameters.*

| | *D (nm)* | *FWHM (deg)* | *τ* | *δ ($nm^{-2}$)* | *a (nm)* | *c (nm)* |
|---|---|---|---|---|---|---|
| *Pure ZnO* | 24.26 | 0.3447 | 0.0046 | 0.0017 | 0.3214 | 0.5247 |
| *ZnO/Ag/ZnO* | 9.83 | 0.8378 | 0.0082 | 0.0103 | 0.3340 | 0.5454 |
| *Mn:ZnO/Ag/ZnO:Mn (5 wt.-%)* | 8.30 | 0.9923 | 0.0109 | 0.0145 | 0.3343 | 0.5459 |
| *Mn:ZnO/Ag/ZnO:Mn (10 wt.-%)* | 25.32 | 0.3251 | 0.0112 | 0.0016 | 0.3359 | 0.5485 |
| *Mn:ZnO/Ag/ZnO:Mn (15 wt.-%)* | 16.54 | 0.4980 | 0.0116 | 0.0037 | 0.3351 | 0.5472 |
| *Mn:ZnO/Ag/ZnO:Mn (20 wt.-%)* | 39.52 | 0.2082 | 0.0127 | 0.0006 | 0.3354 | 0.5477 |

***Table. IV.7.*** *Crystallites size D and lattice parameters of Ag for all samples*

| | *D (nm)* | *a (nm)* |
|---|---|---|
| *ZnO/Ag/ZnO* | 11.79 | 0.423 |
| *Mn:ZnO/Ag/ZnO:Mn (5 wt.-%)* | 10.47 | 0.423 |
| *Mn:ZnO/Ag/ZnO:Mn (10 wt.-%)* | 134.67 | 0.423 |
| *Mn:ZnO/Ag/ZnO:Mn (15 wt.-%)* | 27.82 | 0.424 |
| *Mn:ZnO/Ag/ZnO:Mn (20 wt.-%)* | 73.34 | 0.425 |

### IV.II.2. Optical properties

**Figure IV.11** presents the transmission spectra of the ZnO:Mn/Ag/ZnO:Mn multilayer as a function of wavelength in the range of 200 to 1200 nm. The transmission of the multilayers in the visible range from 600 nm increases with the addition of 5 wt.-% Mn from 54.5% to 76.9%, then decrease with the increase of Mn weight percentage to reach a lower value of 58% for 20 wt.-% Mn. As with the single layers, all multilayered samples show a high transmission in UV-Vis. In addition, tiny peaks between 200 and 400 nm indicate the excitonic properties of the ZnO thin films. The ZnO/Ag/ZnO sample's transmission spectra exhibit an apparent extinction peak at around 500 nm, which is caused by the Localized Surface Plasmon Resonance (LSPR) phenomenon induced by the Ag layer [29,30]. We could notice that this peak has shifted due to the Mn doping, however the peak wildly broadened for the 10 wt-. % Mn sample. This could be explained by the high grain size of the Ag recorded in the X-ray diffraction part.

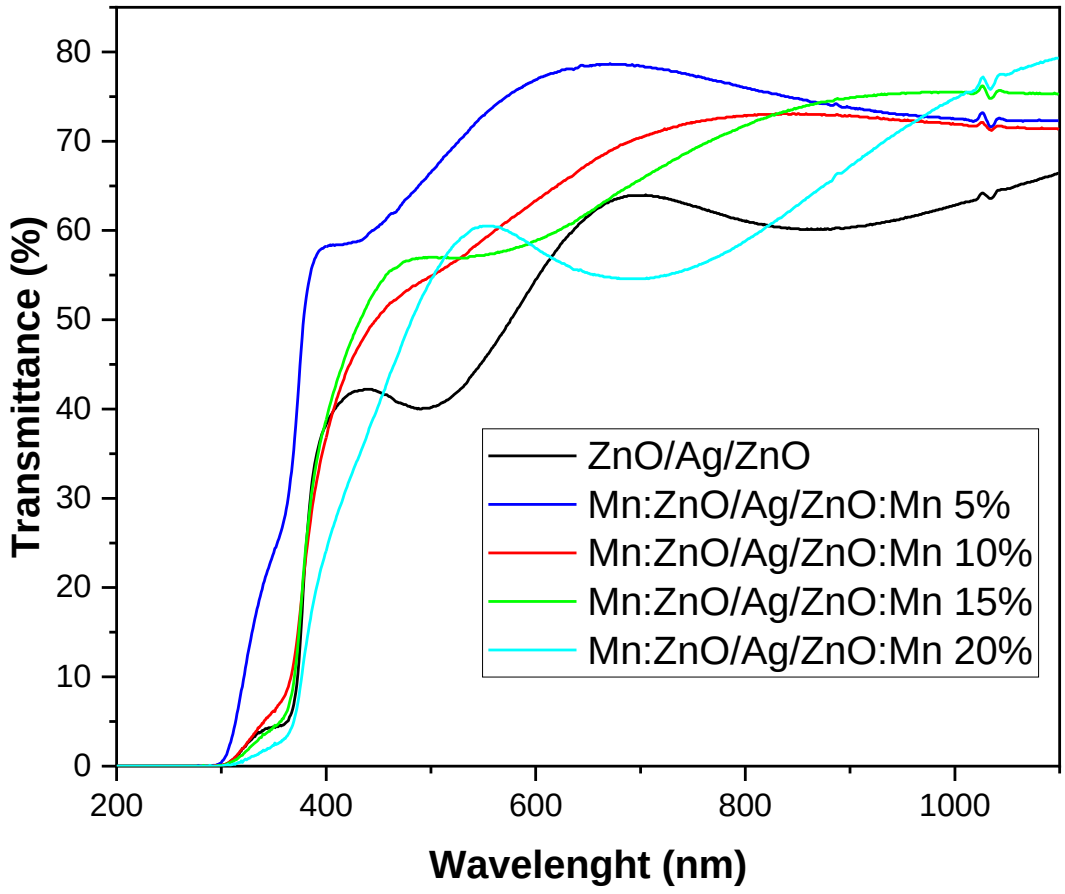


***Figure IV.11.*** *The transmittance spectra of ZnO/Ag/ZnO and Mn:ZnO/Ag/ZnO:Mn multilayers.*

The DA algorithm was not suitable for multilayers, for this reason we used the PSO algorithm, which shows great results. We calculated the optical parameters, thickness, refractive index (n), extinction coefficient (k), and RMSE from the transmission spectrum; the results are presented in **Table IV.8**.

It should be noted that the method used to extract optical constants is designed for a monolayer on a glass substrate. In this work, the approximation is made that the ZnO/Ag/ZnO and Mn:ZnO/Ag/ZnO:Mn (5, 10, 15, and 20 wt.-% Mn) multilayers behave optically as a single layer. Thus, the successfully obtained parameters will be considered to be effective constants. **Figure IV.12** confirms the efficiency of the PSO algorithm used.

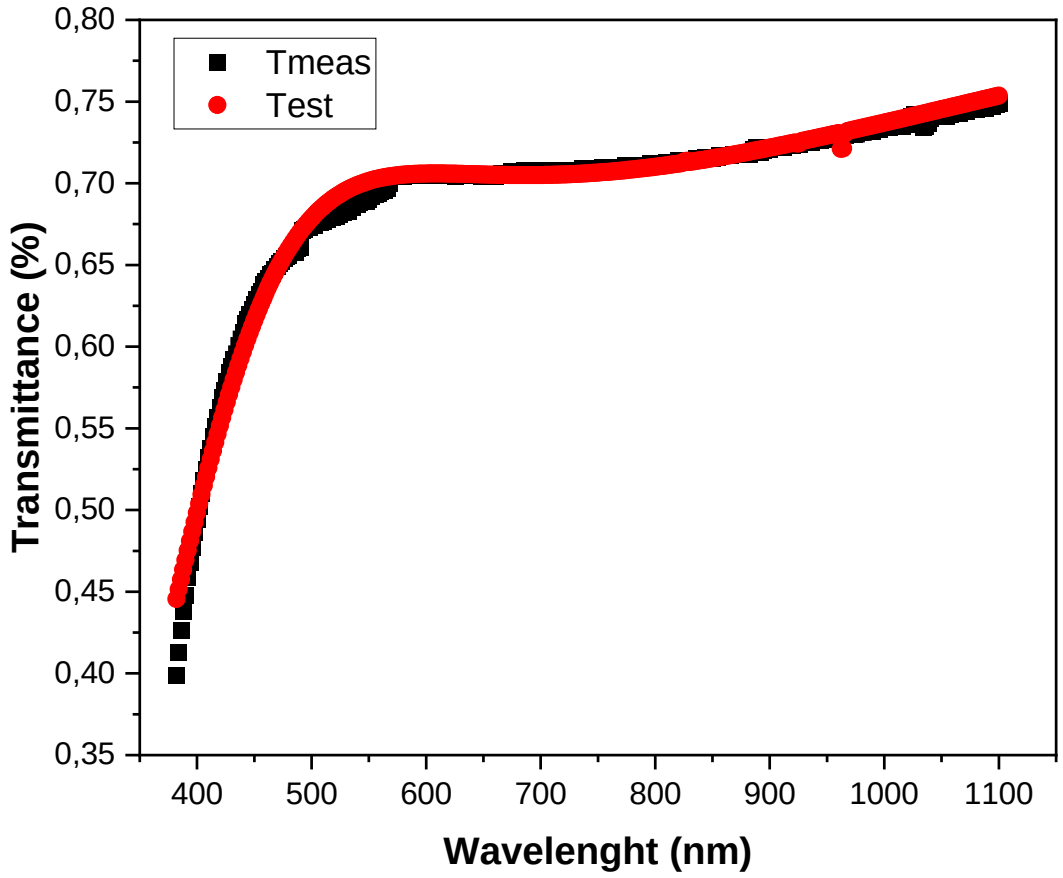


***Figure IV.12.*** *Measured and estimated transmittance for 20wt.-% Mn:ZnO/Ag/ZnO:Mn.*

***Table IV.8.*** *Band gap (Eg), Transmittance (T), Estimated and Measured Thicknesses, refractive index (N), extinction coefficient (k) and RMSE of the multilayers.*

| | ***Eg*** **(eV)** | ***T (%)*** **(λ=600)** | ***Thickness*** *(nm)* **est** | **mes** | ***N*** **( λ=600)** | ***$n_0$*** **(static)** | ***k*** **(λ=600)** | ***RMSE*** |
|---|---|---|---|---|---|---|---|---|
| ***ZnO/Ag/ZnO*** | 3.80 | 54.5 | 425 | 425 | 1.88 | 1.89 | 0.0429 | 0.056 |
| ***Mn:ZnO/Ag/ Mn:ZnO (5wt.-%)*** | 3.92 | 76.9 | 390 | 391 | 1.89 | 1.89 | 0.0127 | 0.06 |
| ***Mn:ZnO /Ag/ Mn:ZnO (10wt.-%)*** | 3.84 | 63.3 | 363 | 365 | 1.91 | 1.91 | 0.0383 | 0.52 |
| ***Mn:ZnO/Ag/ Mn:ZnO (15wt.-%)*** | 3.83 | 58.8 | 452 | 450 | 1.76 | 1.76 | 0.0416 | 0.061 |
| ***Mn:ZnO /Ag/ Mn:ZnO (20wt.-%)*** | 3.82 | 58 | 488 | 489 | 2.1 | 2.09 | 0.0340 | 0.069 |

By assuming that the transition between the valence and the conduction bands in ZnO is direct, we could calculate the energy gap (Eg) from the following equation for direct allowed transition [31]:

$$\alpha h\nu = A\,(h\nu - Eg)^{1/2} \qquad \text{(IV.10)}$$

Where α is the absorption coefficient, A is a constant, hυ is the photon energy, and $E_g$ is the optical band. The variation of the absorption coefficient as a function of energy (hυ) is shown in **Figure IV.13**.

**Figure IV.14** shows plots of $(\alpha h\upsilon)^2$ versus (hυ). The optical band gap of samples was calculated from these plots by extrapolating the linear region of the resulting curve to $(\alpha h\nu)^2 = 0$. The values of $E_g$ for ZnO/Ag/ZnO and Mn:ZnO/Ag/Mn:ZnO (5, 10, 15 and 20 wt.-% Mn) are respectively 3.8 eV, 3.92 eV, 3.84 eV, 3.83 eV and 3.82 eV. The incorporation of Mn decreases the wavelength and, therefore, increases the optical gap. However, due to the multilayering and the enhancement of the electrical properties with the Mn addition, it decreases slightly to reach 3.83 eV.

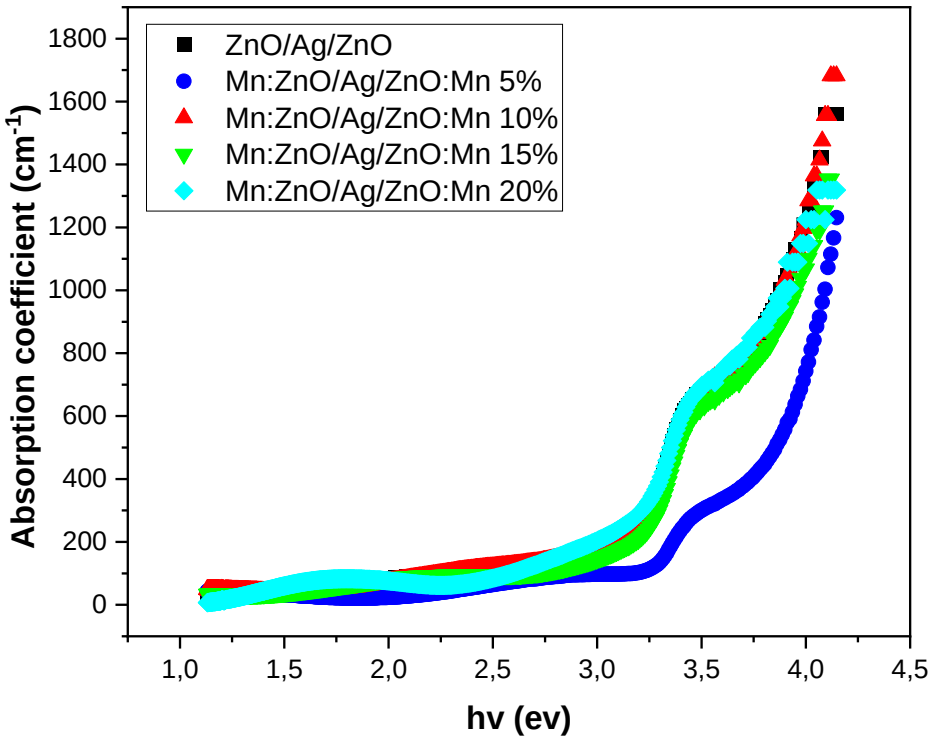


***Figure IV.13.*** *The variation of the absorption coefficient as a function of energy (hυ).*

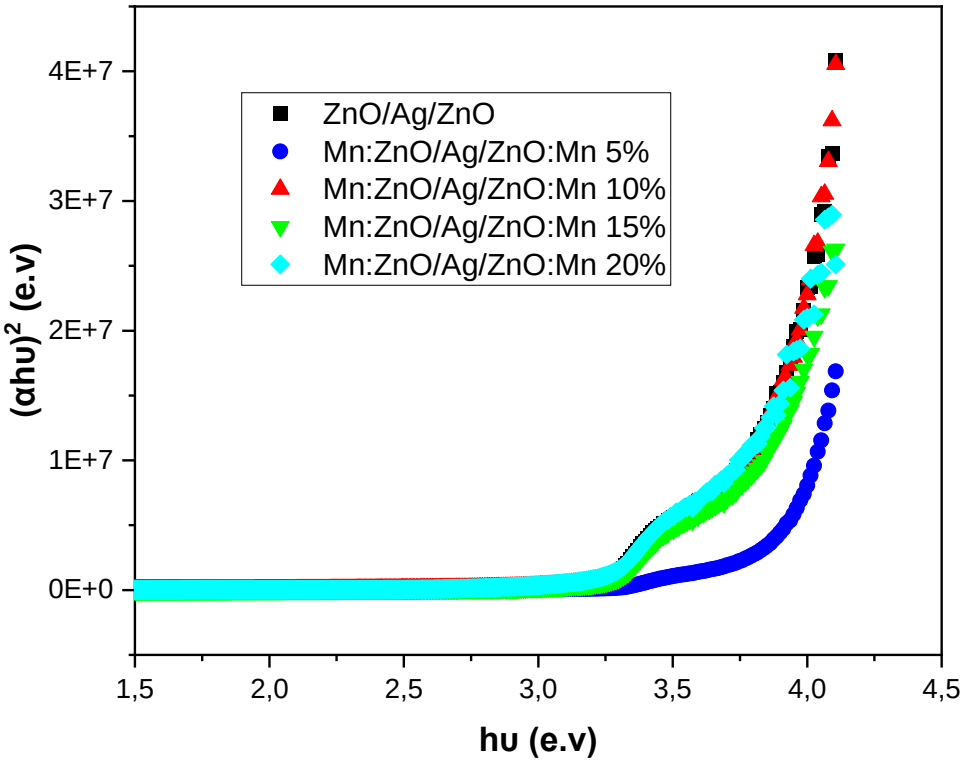


***Figure IV.14.*** *The plots of $(\alpha h\upsilon)^2$ as a function of photon energy.*

### IV.II.3. Electrical properties

The sheet resistance and resistivity of the multilayer films were obtained by the four-point technique, as shown in **Table IV.9**. They both decreased after the incorporation of Mn from 271.8 Ω to 99.63 Ω and from 11.55. $10^5$ Ω.m to 4.86. $10^5$ Ω.m, respectively, due to the increase in mobility and carrier concentration of charges according to Schottky theory [16-18]. As a result, the conductivity increases. These results are great compared to ZnO single-layer sheet resistance (180 kΩ) reported by Hong et al. [19], which confirms that the Ag layer plays an essential role in increasing charge carriers to produce conductivity.

***Table IV.9.*** *Sheet resistance, Resistivity, Conductivity, and Figure of merit of the non-doped and doped multilayers.*

| | Thickness nm | Sheet resistance Rs (Ω) | Resistivity ρ. $10^5$ (Ω.m) | Conductivity σ ($Ω^{-1}$.m-1) |
|---|---|---|---|---|
| ZnO/Ag/ZnO | 425 | 271.8 | 11.55 | 8656,88 |
| Mn:ZnO/Ag/ Mn:ZnO (5wt.-%) | 390 | 163.08 | 6.36 | 15722,97 |
| Mn:ZnO/Ag/ Mn:ZnO (10wt.-%) | 363 | 154.01 | 5.59 | 17887,29 |
| Mn:ZnO/Ag/ Mn:ZnO (15wt.-%) | 452 | 107.26 | 4.85 | 20626,42 |
| Mn:ZnO/Ag/ Mn:ZnO (20wt.-%) | 488 | 99.63 | 4.86 | 20567,90 |

The conductivity of the multilayers is mainly due to the silver interlayer sandwiched between the two dielectric zinc oxide layers [17, 20]. In 1976, G. Haacke [21] proposed a factor called the figure of merit (Φ), which is a correlation between the optical properties and the electrical properties; this factor is defined as the ratio between the transmission in the visible (400 – 800 nm ) and the sheet resistance:

$$Q_H = \frac{T_{600\,nm}}{R_s} \qquad \text{(IV.11)}$$

This factor gives us an idea about the quality and effectiveness of our multilayers as a TCO designed for optoelectrical applications. The figure of merit is very low for the non-doped multilayers compared to the doped ones. This is mainly attributed to the decrease in sheet resistance resulted from the increase in Mn percentage. The high reached value is for Mn:ZnO/Ag/ Mn:ZnO 20wt.-% Mn, making this layer the best candidate as a TCO according to Heeck's law.

It is important to mention that Heeck's law has the disadvantage of not considering the film's thickness. For this reason, we used the following equation suggested by Gordon [38] to investigate the efficiency of our samples:

$$Q_G = \frac{\sigma}{\alpha} = -[(R_s \ln(T+R))]^{-1} = T.\sigma.t \qquad \text{(IV.12)}$$

Where σ is conductivity; α is absorption coefficient (average value in the visible range); $R_s$ is sheet resistance; T and R are the total transmittance and reflectance (in the visible range); t is the thickness. **Table IV.10** summarizes the results and presents results from other researchers.

***Table IV.10.*** *Thickness, Transmittance and figure of merit*

| | Thickness nm | Transmittance T % (wavelength) | $Q_H$ $.10^3$ ($\Omega^{-1}$) | $Q_G$ ($\Omega^{-1}$) |
|---|---|---|---|---|
| Al doped ZnO [39] | - | 94 | 0.53 | - |
| Al doped ZnO [40] | 178 | 65 | 0.0413 | - |
| Mn doped ZnO [40] | 192 | 58 | $7.62 .10^{-6}$ | - |
| Pure ZnO [40] | 210 | 75 | $3.23 .10^{-5}$ | - |
| ZnO/Ag/ZnO | 425 | 44.5 | 2.01 | 0.82 |
| Mn:ZnO/Ag/ Mn:ZnO (5wt.-%) | 390 | 76.9 | 4.72 | 2.96 |
| Mn:ZnO/Ag/ Mn:ZnO (10wt.-%) | 363 | 63.3 | 4.11 | 1.56 |
| Mn:ZnO/Ag/ Mn:ZnO (15wt.-%) | 452 | 58.8 | 5.48 | 2.03 |
| Mn:ZnO/Ag/ Mn:ZnO (20wt.-%) | 488 | 58 | 5.82 | 2.05 |

Comparing the values of the figure of merit for our samples calculated by Heeck's law and those obtained by Gordon's law, we observe a similar variation caused by Mn doping. According to both laws. The highest value of figure of merit is 5.82 $.10^{-3}$ $\Omega^{-1}$, for Mn:ZnO/Ag/ZnO:Mn 20wt.-% Mn making it the most suitable option as a TCO film, this value is higher than the results obtained for other films (**Table IV.10**).

### IV.II.4. Contact angle

The wettability properties of TCOs play a crucial role in understanding the self-cleaning mechanism of dust and dirt particles accumulated on the surface, which will directly affect the surface's performance in the case of photocatalytically active thin films. To ascertain the water contact angles of the acquired thin films, three measurements were conducted for each examined sample, and the mean value was calculated (**Figure IV.15**) for different times (0s, 3s, and 5s). The measurements were conducted at room temperature. **Figure IV.16** displays photographs of the water droplets on the surface of the thin films. The contact angle of the ordinary glass substrate is around 46°, and it increases to 84.5°after deposition with multilayer of ZnO/Ag/ZnO. Thus, after doping with Mn, it decreases to reach the lowest value of 32° for 10 wt-s% Mn. However, we can see in Figure 3 that the contact angle increases again after adding more Mn.

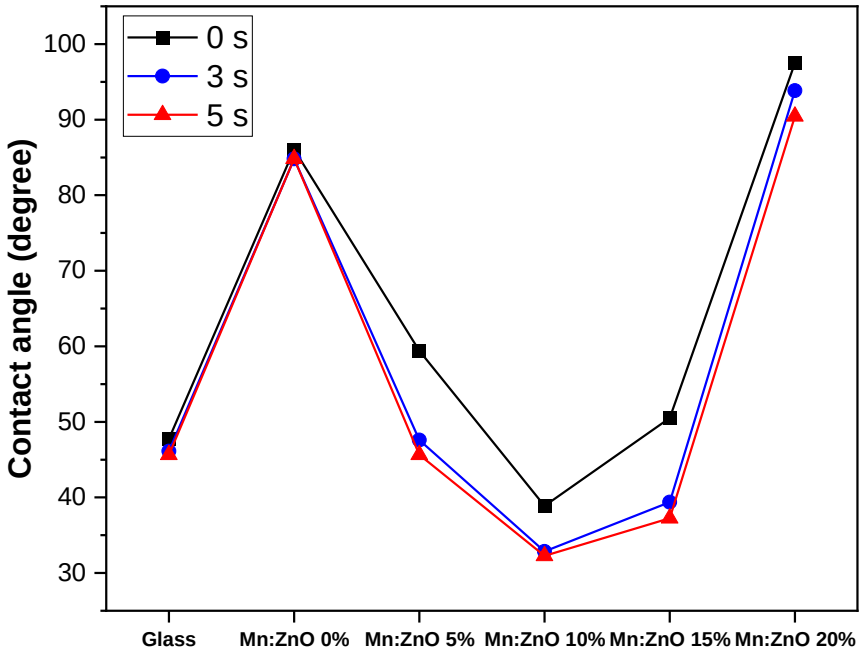


***Figure IV.15.*** *The variation of contact angle of a glass substrate, non-doped and doped multilayers.*

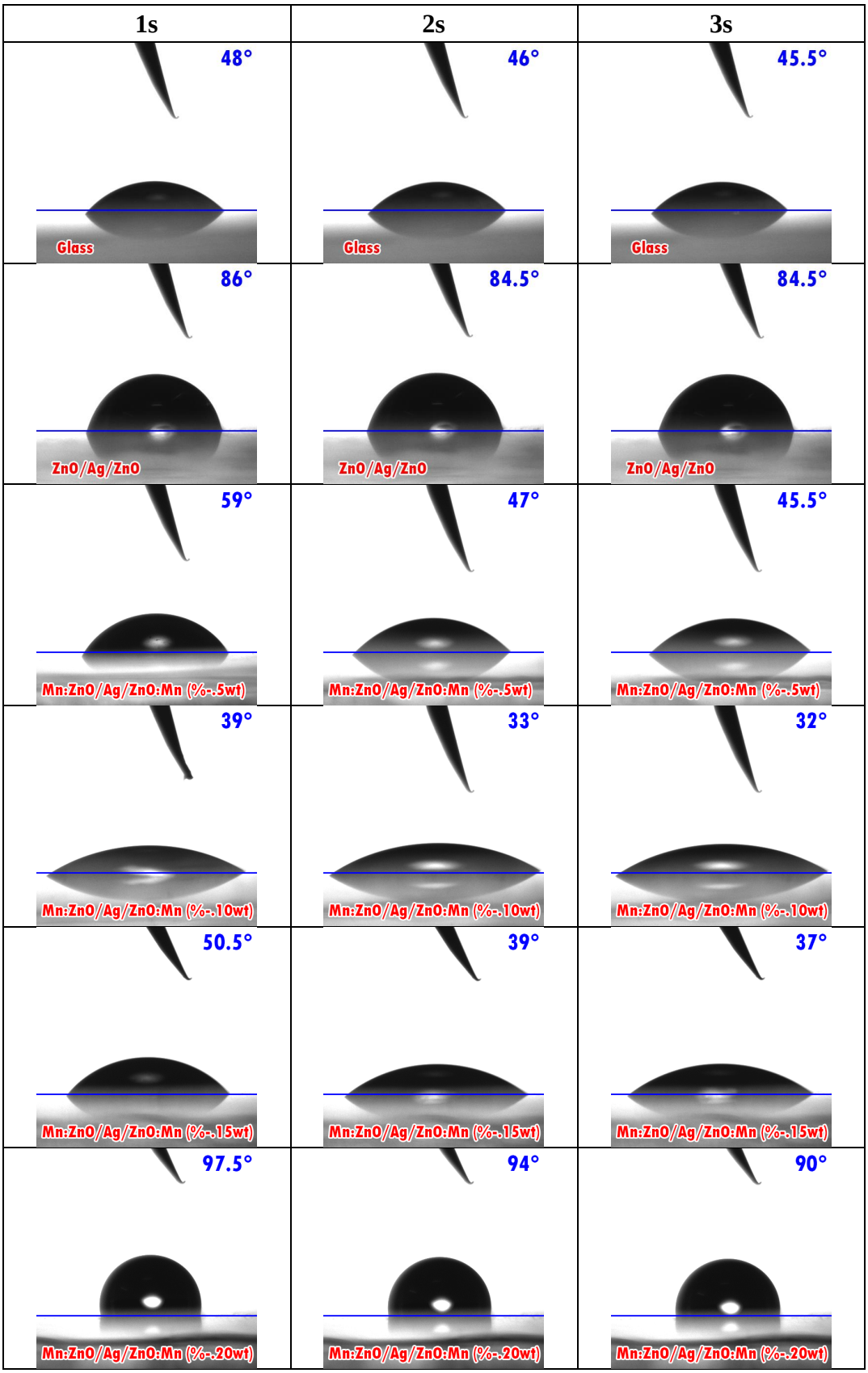


***Figure IV.16.*** *Photographs of the contact angle of water droplets on a glass substrate, non-doped, and doped multilayers at different times (0s, 3s, and 5s).*

The incorporation of transition metals, such as Mn, in the ZnO structure can lower the surface energy of the grains. This is accomplished by the introduction of more transition metal dopant carriers [41,42]. Doping ZnO thin films with slight concentrations of Mn (5 and 10 wt-. %) enhance their hydrophilic characteristics. Alternatively, when highly Mn amounts (15 and 20 wt-. %) are used, the contact angle decreases, and the surface becomes hydrophobic, reaching 90° for the greatest Mn percentage.

From the results presented in part I of the SEM images, it is clear that 15 wt-. % and 20 wt-. % of Mn samples present holes in the surface, which indeed capture air and inhibit water from spreading on the surface. According to the Cassie-Baxter model [43,44], in this particular case, the liquid droplet sits on the maximum of the crest, so the hydrophobicity increases.

## Conclusion

Our work is devided into two main parts, first we studied the effect of Mn on single layer of ZnO thin film and the second part we investigated the structure and properties of ZnO/Ag/ZnO and Mn:ZnO/Ag/ZnO: Mn multilayers.

In the first part, after doping ZnO thin films with Mn, we observed the appearance of the hexagonal Wurtzite phase, accompanied by an increase in the c-axis and a reduction in crystallite size, according to XRD studies Raman spectroscopy has revealed the absence of the combined vibrational modes LA+TO following the introduction of Mn as a dopant and the emergence of the A1(LO)+E2(Low) mode in the heavily doped samples (15 and 20%). The average optical transmittance of the annealed doped layers dropped as the concentration of Mn doping increased, ranging from 83.1% to 69.5%. By analysing the transmittance spectra using the Dragonfly Algorithm, accurately determine and calculate the optical constants n, α, k, and the thickness d. In addition, the energy band gap Eg was calculated for all samples, and it reduces from 3.95 eV to 3.79 eV as Mn doping concentration increases from 0 to 20 wt.-%.

In the second part, similar to the results of the previous part, we notice the appearance of the hexagonal Wurtzite structure, as All the samples are transparent in the visible range. The values of Eg for ZnO/Ag/ZnO and Mn:ZnO/Ag/Mn:ZnO (5, 10, 15 and 20 wt.-% Mn) are respectively 3.8 eV, 3.92 eV, 3.84 eV, 3.83 eV and 3.82 eV. The high reched value is for Mn:ZnO/Ag/ Mn:ZnO 20wt.-% Mn, making this layer the best candidate as a TCO. Incorporating small amounts of Mn into ZnO thin films improves their hydrophobic properties. On the other hand, the contact angle drops, and the surface becomes hydrophilic when higher levels of Mn are used.

## References

*[1] Habis, C., Zaraket, J., & Aillerie, M. (2022, July). Transparent Conductive Oxides. Part I. General Review of Structural, Electrical and Optical Properties of TCOs Related to the Growth Techniques, Materials and Dopants. In Defect and Diffusion Forum (Vol. 417, pp. 243-256). Trans Tech Publications Ltd.*

*[2] Fortunato, E., Ginley, D., Hosono, H., & Paine, D. C. (2007). Transparent conducting oxides for photovoltaics. MRS bulletin, 32(3), 242-247.*

*[3] Afre, R. A., Sharma, N., Sharon, M., & Sharon, M. (2018). Transparent conducting oxide films for various applications: A review. Reviews on advanced materials science, 53(1), 79-89.*

*[4] Hassani, S., Garoudja, E., Amrani, R., Filali, W., Sifi, O., & Oussalah, S. (2023). Elaboration and characterization of pure ZnO, Ag: ZnO and Ag-Fe: ZnO thin films: Effect of Ag and Ag-Fe doping on ZnO physical properties. Revista Mexicana de Física, 69(5 Sep-Oct), 051005-1.*

*[5] Ahmed, S. A. (2017). Structural, optical, and magnetic properties of Mn-doped ZnO samples. Results in physics, 7, 604-610.*

*[6] López-Suárez, A., Acosta, D., Magaña, C., & Hernández, F. (2020). Optical, structural and electrical properties of ZnO thin films doped with Mn. Journal of Materials Science: Materials in Electronics, 31(10), 7389-7397.*

*[7] Baghdad, R., Kharroubi, B., Abdiche, A., Bousmaha, M., Bezzerrouk, M. A., Zeinert, A., ... & Zellama, K. (2012). Mn doped ZnO nanostructured thin films prepared by ultrasonic spray pyrolysis method. Superlattices and Microstructures, 52(4), 711-721.*

*[8] Boshta, M., Abou-Helal, M. O., Ghoneim, D., Mohsen, N. A., & Zaghlool, R. A. (2010). The photocatalytic activity of sprayed Zn1− xMgxO thin films. Surface and Coatings Technology, 205(2), 271-274.*

*[9] Li, J., Yang, D., Zhu, X., Sun, H., Gao, X., Wangyang, P., & Tian, H. (2017). Structural and optical properties of nano-crystalline ZnO thin films synthesized by sol–gel method. Journal of Sol-Gel Science and Technology, 82, 563-568.*

*[10] Mekhnache, M., Drici, A., Hamideche, L. S., Benzarouk, H., Amara, A., Cattin, L., ... & Guerioune, M. (2011). Properties of ZnO thin films deposited on (glass, ITO and ZnO: Al) substrates. Superlattices and Microstructures, 49(5), 510-518.*

*[11] Hemathangam, S., Thanapathy, G., & Muthukumaran, S. (2016). Influence of Mn doping on structural, optical and photoluminescence properties of Cd 0.98 Co 0.02 S thin films by chemical bath deposition method. Journal of Materials Science: Materials in Electronics, 27, 1791-1798.*

*[12] Khosravi-Gandomani, S., Yousefi, R., Jamali-Sheini, F., & Huang, N. M. (2014). Optical and electrical properties of p-type Ag-doped ZnO nanostructures. Ceramics international, 40(6), 7957-7963.*

*[13] Li, J., Yang, D., & Zhu, X. (2017). Effects of aging time and annealing temperature on structural and optical properties of sol-gel ZnO thin films. Aip Advances, 7(6).*

*[14] Wang, J. B., Huang, G. J., Zhong, X. L., Sun, L. Z., Zhou, Y. C., & Liu, E. H. (2006). Raman scattering and high temperature ferromagnetism of Mn-doped ZnO nanoparticles. Applied Physics Letters, 88(25).*

*[15] Hamidian, K., Sarani, M., Barani, M., & Khakbaz, F. (2022). Cytotoxic performance of green synthesized Ag and Mg dual doped ZnO NPs using Salvadora persica extract against MDA-MB-231 and MCF-10 cells. Arabian Journal of Chemistry, 15(5), 103792.*

*[16] Cuscó, R., Alarcón-Lladó, E., Ibáñez, J., Artús, L., Jiménez, J., Wang, B., & Callahan, M. J. (2007). Temperature dependence of Raman scattering in ZnO. Physical Review B—Condensed Matter and Materials Physics, 75(16), 165202.*

*[17] Yadav, H. K., Sreenivas, K., & Gupta, V. (2006). Influence of postdeposition annealing on the structural and optical properties of cosputtered Mn doped ZnO thin films. Journal of Applied Physics, 99(8).*

*[18] Shaaban, E. R., El-Hagary, M., Emam-Ismail, M., Matar, A., & Yahia, I. S. (2013). Spectroscopic ellipsometry and magneto-transport investigations of Mn-doped ZnO nanocrystalline films deposited by a non-vacuum sol–gel spin-coating method. Materials Science and Engineering: B, 178(3), 183-189.*

*[19] Singh, P., & Kumar, R. (2021). Investigation of refractive index dispersion parameters of Er doped ZnO thin films by WDD model. Optik, 246, 167829.*

*[20] Amrani, R., Garoudja, E., Lekoui, F., Filali, W., Neggaz, H., Djebeli, Y. A., ... & Henini, M. (2023). Investigation of structural and electrical properties of ITO thin films and correlation to optical parameters extracted using novel method based on PSO algorithm. Bulletin of Materials Science, 46(1), 8.*

*[21] Grine, D., Akkari, H., Fernández, P., Mekhalif, T., Hassani, S., & Lekoui, F. (2022). Synthesis, characterization, and antibacterial activity of Ag–TiO2–Fe composite thin films. physica status solidi (a), 219(11), 2200036.*

*[22] Shatnawi, M., Alsmadi, A. M., Bsoul, I., Salameh, B., Mathai, M., Alnawashi, G., ... & Bawa'aneh, M. S. (2016). Influence of Mn doping on the magnetic and optical properties of ZnO nanocrystalline particles. Results in Physics, 6, 1064-1071.*

*[23] Peng, L. P., Fang, L., Yang, X. F., Li, Y. J., Huang, Q. L., Wu, F., & Kong, C. Y. (2009). Effect of annealing temperature on the structure and optical properties of In-doped ZnO thin films. Journal of Alloys and Compounds, 484(1-2), 575-579.*

*[24] Chen, H., Ding, J., Guo, W., Shi, F., & Li, Y. (2012). Violet–blue–green emission and shift in Mg-doped ZnO films with different ratios of oxygen to argon gas flow. Applied surface science, 258(24), 9913-9917.*

*[25] S. Vallejo, W., Cantillo, A., & Díaz-Uribe, C. (2023). Improvement of the photocatalytic activity of ZnO thin films doped with manganese. Heliyon, 9(10). [26] Belamri, Z., N. Mermoul, and D. Hamana, Acta Physica Polonica: A, 145, 6, 2024.*

*[27] Derri, A., Mokadem, A., Ouerdane, A., Bensassi, K. B., Bouslama, M. H., Kharoubi, B., & Hameurlaine, E. (2023). Insight into the photoluminescence and morphological characteristics of transition metals (TM= Mn, Ni, Co, Cu)-doped ZnO semiconductor: a comparative study. Optical Materials, 145, 114467.*

*[28] Yoshino, Y., Inoue, K., Takeuchi, M., Makino, T., Katayama, Y., & Hata, T. (2000). Effect of substrate surface morphology and interface microstructure in ZnO thin films formed on various substrates. Vacuum, 59(2-3), 403-410.*

*[29] Lim, S. K., Chung, K. J., Kim, C. K., Shin, D. W., Kim, Y. H., & Yoon, C. S. (2005). Surface-plasmon resonance of Ag nanoparticles in polyimide. Journal of applied physics, 98(8).*

*[30] Venugopal, N., & Mitra, A. (2013). Influence of temperature dependent morphology on localized surface plasmon resonance in ultra-thin silver island films. Applied surface science, 285, 357-372.*

*[31] Tauc, J. (Ed.). (2012). Amorphous and liquid semiconductors. Springer Science & Business Media.*

*[32] Kultayeva, S., Ha, J. H., Malik, R., Kim, Y. W., & Kim, K. J. (2020). Effects of porosity on electrical and thermal conductivities of porous SiC ceramics. Journal of the European Ceramic Society, 40(4), 996-1004.*

*[33] Lee, J. Y., Yang, J. W., Chae, J. H., Park, J. H., Choi, J. I., Park, H. J., & Kim, D. (2009). Dependence of intermediated noble metals on the optical and electrical properties of ITO/metal/ITO multilayers. Optics Communications, 282(12), 2362-2366.*

*[34] Sahu, D. R., Lin, S. Y., & Huang, J. L. (2006). ZnO/Ag/ZnO multilayer films for the application of a very low resistance transparent electrode. Applied surface science, 252(20), 7509-7514.*

*[35] Hong, C. S., Park, H. H., Moon, J., & Park, H. H. (2006). Effect of metal (Al, Ga, and In)-dopants and/or Ag-nanoparticles on the optical and electrical properties of ZnO thin films. Thin Solid Films, 515(3), 957-960. [36] V. Sharma, et al., Solar Energy Materials and Solar Cells, 169, 2017.*

*[37] Haacke, G. (1976). New figure of merit for transparent conductors. Journal of Applied physics, 47(9), 4086-4089.*

*[38] Gordon, R. G. (2000). Criteria for choosing transparent conductors. MRS bulletin, 25(8), 52-57.*

*[39] Joseph, B., Manoj, P. K., & Vaidyan, V. K. (2006). Studies on the structural, electrical and optical properties of Al-doped ZnO thin films prepared by chemical spray deposition. Ceramics International, 32(5), 487-493.*

*[40] Amroun, M. N., Salim, K., Kacha, A. H., & Khadraoui, M. (2020). Effect of TM (TM= Sn, Mn, Al) doping on the physical properties of ZnO thin films grown by spray pyrolysis technique: a comparative study. Int. J. Thin. Film. Sci. Tec, 9(1), 7-19.*

*[41] Tyona, M. D., Osuji, R. U., Asogwa, P. U., Jambure, S. B., & Ezema, F. I. (2017). Structural modification and band gap tailoring of zinc oxide thin films using copper impurities. Journal of Solid State Electrochemistry, 21, 2629-2638.*

*[42] Sun, H., Luo, M., Weng, W., Cheng, K., Du, P., Shen, G., & Han, G. (2008). Room-temperature preparation of ZnO nanosheets grown on Si substrates by a seed-layer assisted solution route. Nanotechnology, 19(12), 125603.*

*[43] Cassie, A. B. D., & Baxter, S. (1944). Wettability of porous surfaces. Transactions of the Faraday society, 40, 546-551.*

*[44] Cassie, A. B. D. (1948). Contact angles. Discussions of the Faraday society, 3, 11-16.*

# General Conclusion

# General Conclusion

This thesis work allowed us to gain a good understanding of the behavior of the materials used; Mn-doped ZnO and Mn:ZnO/Ag/ZnO: Mn (0, 5, 10, 15, and 20 wt.-% Mn) transparent conductive oxides. We were also able to investigate the evolution of the structural, morphology, wettability, optical and electrical properties of the thin films. All the films were deposited by thermal evaporation on an ordinary glass substrate and then annealed at 500°C for 2h. The use of this deposition technique leads to multilayers with good homogeneity; moreover, it has the advantage of being a simple and easy-to-implement technique, as well as being low-cost compared to other techniques.

The X-ray diffraction analysis of the prepared samples shows that Zn oxidation occurs after annealing. ZnO crystallizes in a hexagonal Wurtzite structure, and Ag in a cubic crystalline structure without any peak, indicating the existence of Mn, which means Mn replaced Zn atoms in the structure.

Unlike XRD results, we noticed an appearance of LVM modes in Raman that belongs to the Mn atoms, which confirms the existence of Mn in our doped films.

The SEM analysis was used to characterize the surface morphology of our thin films. The electron micrographs indicate that all substrates are completely coated. Mn doping modifies the morphology, resulting in a more uniform structure. The films exhibit unevenly distributed spherical particle agglomerations over the substrate, with an average diameter of 5.36 μm.

The dragonfly algorithm (DA) and particle swarm optimization (PSO) were successfully used to determine the optical parameters of the single layers and multilayers, respectively. The optical band gap of ZnO film is 3.95 eV; it slightly decreases after doping with Mn and multilayering, this could be explained by the strains in semiconductor films.

The electrical characterization using the four-point technique indicates that doping with manganese has an opposite effect on the shit resistance. This means that doping increases conductivity.

To better understand the efficiency of our TCOs for photovoltaic application we measured the figure of merit. The results are great compared to the values found in previous

works. The Mn:ZnO/Ag/ Mn:ZnO 20wt.-% Mn sample has the highest value of figure of merit, making this layer the best candidate as a TCO.

Wettability is an important factor in determining the application of the TCO. Adding small amounts of Mn to ZnO thin films enhance their hydrophobic properties, while adding it in higher quantities decreases the contact angle making the surface hydrophilic.

In conclusion, the deposition process we used has produced significant results and requires additional investigation. All the layers have major potential for application as transparent conductive oxides (TCOs) due to their impressive transparency and perfect conductivity. In order to complete this study and with a view to improving the performance of the Mn:ZnO/Ag/ZnO:Mn thin films, we plan to carry out the following:

- Incorporating novel doping strategies or adding more layers could enhance the material properties for specific applications. For example, enhancing the magnetic or catalytic properties of the samples opens up new application areas, such as spintronics or advanced sensors.
- Conduct more electrical characterizations, particularly Hall effect measurements, which allow us to determine resistivity and especially to ascertain the density and mobility of carriers in the films, enabling us to connect structural and electrical properties.
- Integrating ZnO/Ag/ZnO multilayers into flexible and transparent electronic devices, the mechanical flexibility of the films will ensure their performance under bending or stretching conditions, which is crucial for the development of next-generation wearable electronics and flexible displays.
- Exploring different metal interlayers other than silver could offer valuable insights into obtaining even lower electrical resistance or improved stability, especially under challenging conditions or at decreased expenses.

Addressing these areas will not only refine the existing technologies but also pave the way for innovative applications and more cost-effective production methods.

## Abstract

In this work, our objective is to produce transparent electrodes destined for applications in photovoltaic systems. These electrodes are based on Mn:ZnO/Ag/ZnO:Mn transparent conductive oxide (TCO) multilayers deposited on a glass substrate by the thermal evaporation technique, with the Mn percentage varying from 5 wt.-% to 20 wt.-%. We investigated the effect of Mn doping on the structure and properties of single-layer and multilayer thin films. All the samples are transparent in the visible range and exhibit a hexagonal Wurtzite structure according to the x-ray diffraction (XRD) results. Mn was incorporated without changing the structure. For ZnO and Mn-doped ZnO films, Raman spectroscopy revealed the presence of A 1 (LO) and LVM vibration modes. However, we noticed the absence of LVM mode for the non-doped sample and the appearance of LA + TO combined phonons. The extracted optical parameters using a new approach based on the Dragonfly Algorithm show that the optical bandgap of the films decreases from 3.95 to 3.79 eV. For ZnO/Ag/ZnO and Mn:ZnO/Ag/ZnO:Mn (with 5, 10, 15, and 20 wt.-% Mn), the energy band gap values are 3.8 eV, 3.92 eV, 3.84 eV, 3.83 eV, and 3.82 eV, respectively. The addition of low percentages of Mn enhances the hydrophobic characteristics of the multilayers. In reverse, the contact angle decreases for higher percentages, and the surface becomes more hydrophilic. To better understand the efficiency of our films in optoelectronic applications, we calculated the figure of merit; the layer with the highest achieved value is Mn:ZnO/Ag/Mn:ZnO (20wt.-% Mn). This layer is considered the most suitable choice as a Transparent Conductive Oxide (TCO).



***Keywords:*** TCO, Mn:ZnO/Ag/ZnO:Mn, thin films, thermal evaporation, XRD, Raman, Dragonfly algorithm, contact angle, figure of merit, optoelectronic.

## Résumé

Dans ce travail, notre objectif est de produire des électrodes transparentes destinées à des applications dans les systèmes photovoltaïques. Ces électrodes sont basées sur des couches minces de Mn:ZnO/Ag/ZnO:Mn en oxyde conducteur transparent (TCO) déposées sur un substrat en verre par la technique d'évaporation thermique, avec un pourcentage de Mn variant de 5 % en poids à 20 % en poids. Nous avons étudié l'effet du dopage au Mn sur la structure et les propriétés des films minces monocouches et multicouches. Tous les échantillons sont transparents dans la région visible et présentent une structure hexagonale de Wurtzite selon les résultats de diffraction des rayons X (XRD) Le Mn a été incorporé sans modifier la structure. Pour les films de ZnO et de ZnO dopé au Mn, la spectroscopie Raman a révélé la présence des modes de vibration A1 (LO) et LVM. Cependant, nous avons remarqué l'absence du mode LVM pour l'échantillon non dopé et l'apparition de phonons combinés LA + TO. Les paramètres optiques extraits à l'aide d'une nouvelle approche basée sur l'algorithme de la libellule montrent que le gap optique des films diminue de 3,95 à 3,79 eV. Pour ZnO/Ag/ZnO et Mn:ZnO/Ag/ZnO:Mn (avec 5, 10, 15 et 20 % en poids de Mn), les valeurs de la bande interdite d'énergie sont respectivement de 3,8 eV, 3,92 eV, 3,84 eV, 3,83 eV et 3,82 eV. L'ajout de faibles pourcentages de Mn améliore les caractéristiques hydrophobes des multicouches. À l'inverse, l'angle de contact diminue pour des pourcentages plus élevés, et la surface devient plus hydrophile. Pour mieux comprendre l'efficacité de nos films dans les applications optoélectroniques, nous avons calculé le facteur de mérite ; la couche avec la valeur la plus élevée atteinte est Mn:ZnO/Ag/Mn:ZnO (20 % en poids de Mn). Cette couche est considérée comme le choix le plus approprié en tant qu'oxyde conducteur transparent (TCO).



***Mots-clés :*** TCO, Mn:ZnO/Ag/ZnO:Mn, films minces, évaporation thermique, DRX, Raman, algorithme Dragonfly, angle de contact, figure de mérite, optoélectronique.

## ملخص

في هذا العمل، هدفنا هو إنتاج أقطاب شفافة مخصصة للاستخدام في أنظمة الطاقة الشمسية. تستند هذه الأقطاب الكهربائية إلى أكسيد الزنك الشفاف الموصلMn:ZnO/Ag/ZnO:Mn ، والذي يتكون من طبقات متعددة تم ترسيبها على ركيزة زجاجية باستخدام تقنية التبخر الحراري، مع نسبة المنغنيز المتغيرة من 5% إلى 20%. قمنا بدراسة تأثير إضافة المنغنيز على التركيب وخصائص الأفلام الرقيقة ذات الطبقة الواحدة والطبقات المتعددة. جميع العينات شفافة في النطاق المرئي وتظهر هيكل وورتزيت السداسي hexagonal Wurtzite وفقًا لنتائج حيود الأشعة السينية. تم دمج المنغنيز دون تغيير الهيكل. بالنسبة لأفلامZnO النقية و ZnOالمضاف إليها المنغنيز، كشفت مطيافية رامان عن وجود أوضاع اهتزاز A1 (LO) و .LVM ومع ذلك، لاحظنا غياب وضع LVM للعينة غير المشوبة وظهور الفونونات المدمجةLA + TO . تظهر المعلمات البصرية المستخرجة باستخدام نهج جديد يعتمد على خوارزمية اليعسوب أن فجوة الطاقة البصرية للأفلام تنخفض من 3.95 إلى 3.79 إلكترون فولت. بالنسبة لـ ZnO/Ag/ZnO و Mn:ZnO/Ag/ZnO:Mn مع 5 و 10 و 15 و 20 وزن-% من المنغنيز، فإن قيم فجوة الطاقة هي 3.8 إلكترون فولت، 3.92 إلكترون فولت، 3.84 إلكترون فولت، 3.83 إلكترون فولت، و 3.82 إلكترون فولت، على التوالي. إن إضافة نسب منخفضة من المنغنيز تعزز الخصائص الكارهة للماء للطبقات المتعددة. عكس ذلك، زاوية الاتصال تقل مع زيادة النسب، وتصبح السطح أكثر محبة للماء. لفهم كفاءة أفلامنا بشكل أفضل في التطبيقات البصرية الإلكترونية، قمنا بحساب معامل الاستحقاق؛ حيث كانت الطبقة التي حققت أعلى قيمة هي Mn:ZnO/Ag/Mn:ZnO مع نسبة 20 % من المنغنيز تعتبر هذه الطبقة الخيار الأنسب كأكسيد موصل شفاف . (TCO).



***الكلمات المفتاحية:*** TCO، Mn:ZnO/Ag/ZnO:Mn، الأفلام الرقيقة، التبخر الحراري، حيود الأشعة السينية، رامان، خوارزمية اليعسوب، زاوية الاتصال، معامل الاستحقاق، البصرية الإلكترونية.

# Conferences and Publications

## Conferences

1) 24-25 November 2024, Algiers- Algeria: 1st international seminar on materials, processes and microfabrication MPM'24
2) 09-10 May 2023, Algiers- Algeria: The 3rd International Conference on Electrical Engineering CEE'2023.
3) 13-15 December 2022, Khenchela- Algeria: 1st International Conference On Materials Sciences and Technology.
4) 15-17 November 2022, Khenchela- Algeria: The Fifth International Conference on Electrical Engineering Control Applications.
5) 03-04 July 2022, Sidi Bel-Abbès – Alegria : Conférence Internationale sur les Sciences et Génie des Matériaux et leurs Impacts sur L'Environnement.
6) 28-29 June 2022, Khenchela- Algeria: 1st National Conference on Materials Science and Engineering.
7) 17-18 Septembre 2021, Oran- Alegria : Séminaire International sur Les Sciences de la Matière (Physique et Chimie).
8) 16-20 May 2021, Boumerdes- Algeria: 2nd International Symposium on Materials Chemistry.

## Publications

1) Journal of Ovonic Research, Vol 20, Issue 3, p365, ISSN: 1842-2403 "Optical parameters extraction of zinc oxide thin films doped with manganese using an innovative technique based on the dragonfly algorithm and their correlation to the structural properties" DOI: 10.15251/JOR.2024.203.365
2) Lecture Notes in Electrical Engineering series Springer; ISSN: 2773-3106 "Studying the effect of Mn doping on the electrical and optical properties of ZnO/Ag/ZnO multilayer"
3) Proceedings Book of the 2nd International Symposium. ISBN 978-9931- 9091-1-7; DOCID 338194; "Influence of Mn doping on the optical property of ZnO thin films" 342

Journal of Ovonic Research Vol. 20, No. 3, May - June 2024, p. 365 - 380

# Optical parameters extraction of zinc oxide thin films doped with manganese using an innovative technique based on the dragonfly algorithm and their correlation to the structural properties

K. Settara[a,b,*], F. Lekoui[c], H. Akkari[d], E. Garoudja[e], R. Amrani[f], W. Filali[e], S. Oussalah[g], S. Hassani[c]

[a]*Laboratory of Research on Physico-Chemistry of Surface and Interface (LRPCSI), University of 20 August 1955 Skikda, BP 26, Road El Hadaiek, Skikda, 21000, Algeria*

[b]*Laboratory of Mechanical and Materials Engineering (LGMM), University of 20 August 1955 Skikda, BP 26, Road El Hadaiek, Skikda, 21000, Algeria*

[c]*Ionized Media & Laser Division (IMLD), Center for Development of Advanced Technologies (CDTA), Cité 20 Août 1956, Baba Hassen, Algiers, 16081, Algeria*

[d]*Department of Industrial Engineering, Faculty of Technology, University Batna 2 Chahid Mostefa Ben Boulaid, Rue Chahid Boukhlouf M. El Hadi, Batna, 05001, Algeria*

[e]*Micro-manufacturing Technology Platform, Center for Development of Advanced Technologies (CDTA), Cité 20 Août 1956, Baba Hassen, Algiers, 16081, Algeria*

[f]*Department of Material Sciences, University of Algiers Ben Youssef Ben Khadda, 2 Rue Didouche Mourad, Algiers, 16000, Algeria*

[g]*Microelectronic & Nanotechnology Division, Center for Development of Advanced Technologies (CDTA), Cité 20 Août 1956, Baba Hassen, Algiers, 16081, Algeria*

Pure zinc oxide (ZnO) thin films, along with manganese (Mn) doped counterparts, were produced using rapid thermal evaporation technique on ordinary glass substrates. Post-annealing treatments resulted in the formation of hexagonal wurtzite structures in the deposited layers. The Raman results unveiled the presence of A1(LO) and LVM vibration modes in each sample that were doped. Interestingly, the undoped sample lacked the LVM mode while showcasing the emergence of LA + TO combined phonons. Employing a novel approach reliant on the Dragonfly Algorithm, optical parameters were extracted, revealing a drop in the bandgap energy of the films from 3.95 eV to 3.79 eV.

(Received March 17, 2024; Accepted June 4, 2024)

*Keywords:* Dragonfly algorithm, Mn-doped ZnO, Optical parameters, Rapid thermal evaporation, Thin films

## 1. Introduction

Thanks to its properties such as wide bandgap (~3.37 eV), abundance on earth, non-toxicity, stability, and low cost, zinc oxide (ZnO) has become a promising candidate as a replacement to reduce the use of indium tin oxide (ITO) [1, 2] as well as titanium dioxide ($TiO_2$) [3] and stannic oxide ($SnO_2$) [4] in thin-film photovoltaic panels. Zinc oxide (ZnO) thin films possess transparency within the visible spectrum, rendering them suitable for applications like optical windows and solar cell electrodes [5-7]. Nevertheless, their conductivity tends to be weak due to their transparent nature. To address this limitation, doping with small percentages of transition metals like silver (Ag), aluminum (Al), iron (Fe), nickel (Ni), and manganese (Mn), among others, is commonly employed. This doping technique enhances electrical conductivity while preserving the transparency of the films.

* Corresponding author: kh.settara@univ-skikda.dz
https://doi.org/10.15251/JOR.2024.203.365

Manganese (Mn) has been widely used as a metal for ZnO doping. Mn-doped ZnO (Mn:ZnO) films exhibit a significant homogeneity as a result of the strong ability of both materials to dissolve in each other [8]. The $Mn^{2+}$ radii (0.80 Å) and $Zn^{2+}$ (0.74 Å) are close, allowing Mn atoms to substitute Zn atoms easily. This behavior will alter the lattice parameters of ZnO without modifying the structure nature and subsequently cause changes in terms of physical properties, in particular the optical ones [9]. ZnO films can be synthesized on different substrates with several methods, such as pulsed laser deposition [10], sol-gel [11], spray pyrolysis [12, 13], chemical vapor deposition [14], magnetron sputtering [15-16], spin coating [17] and vacuum thermal evaporation [18].

This study examines the structural and optical features of Mn-doped ZnO thin films prepared via rapid thermal evaporation (RTE), focusing on the effect of Mn concentration. Structural properties were investigated using X-ray diffraction (XRD), Raman analysis, energy dispersive spectroscopy (EDS) analysis, and scanning electron microscopy (SEM). Optical characteristics were assessed through the optical transmission spectra obtained using an ultraviolet/visible/near-infrared (UV-Vis-NIR) spectrophotometer. Additionally, optical constants such as thickness, refractive index, extinction coefficient, and absorption coefficient were extracted from the transmission spectra using a novel approach based on the Dragonfly Algorithm (DA) [19], marking the first application of this technique in this context. The relationship between these optical constants and the Mn content will subsequently be studied.

In our previous works [8, 20], we succeeded in developing two methods of optical parameter extraction based on particle swarm optimization (PSO) and artificial bee colony (ABC) algorithm, respectively. Here, for the purpose of optimizing and enhancing research, we adopted a new technique that offers high efficiency in calculating the optical parameters of the deposited films, giving better results and understanding of the effect of doping. The novel method utilized in this study draws inspiration from the natural behaviors of dragonflies, known as the dragonfly algorithm. By emulating both the static and dynamic characteristics exhibited by dragonflies in their environment, this approach is employed to ascertain the optical parameters under investigation.

## 2. Experimental details

### 2.1. Preparing samples

Utilizing the rapid thermal evaporation (RTE) technique, both undoped and Mn-doped ZnO thin films were effectively fabricated on standard glass substrates, incorporating various weight percentages of the dopant (0, 5, 10, 15, and 20 wt.-%). High-purity ZnO and Mn powders sourced from Sigma-Aldrich (with a purity of 99.99%) were employed in the process. The substrate preparation involved a meticulous cleaning procedure, beginning with washing the glass substrates using distilled water and detergent. Subsequently, the substrates underwent a sequential immersion in an ultrasonic acetone bath for 5 minutes, followed by ethanol for an additional 5 minutes. The deposition technique was executed at a low pressure of $10^{-6}$ mbar by heating a crucible to a temperature of 1600 °C, at which the ZnO powder sublimates. The deposition was done quickly, lasting only 15 seconds. After being deposited, the films were subjected to air thermal annealing at a temperature of 500 °C for a period of 2 hours.

### 2.2. Characterization

The XRD technique was used to analyze the structure and morphology of the layers. This analysis was conducted by a Philips X'Pert-MPD diffractometer equipped with a Cu-Kα cathode source that emitted radiation with a wavelength of 1.54 Å. Raman spectroscopy recorded by Lab Ram H-Resolution and SEM coupled with EDX spectroscopy using a Hitachi S4800 cold field-emission. The optical characteristics were examined using a Shimadzu UV-1280 spectrophotometer.

### 2.3. Dragonfly algorithm

In 2016, an efficient optimization method known as the Dragonfly Algorithm was developed by S. Mirjalili [19]. It is chiefly originated from hunting and migrating behaviors of real dragonflies. Dragonfly hunting activity is referred to as static swarm, whereas migration behavior is referred to as dynamic swarm. In nature, dragonflies exhibit distinct behaviors depending on their context. In static swarms, they gather in small groups, navigating their surroundings in search of sustenance. Conversely, dynamic swarms involve a larger congregation of dragonflies migrating together in a unified direction. Analogously, in optimization algorithms, the exploration and exploitation stages closely resemble the behaviors observed in static and dynamic swarms, respectively. Every dragonfly represents a potential solution inside the search space. In this algorithm, six weights are employed to steer the dragonflies to their destinations: separation weight (s), alignment weight (a), cohesion weight (c), food factor (f), enemy factor (e), and inertia weight (w). It is recommended to employ high alignment and low cohesion weights to achieve optimal exploration of the search space. Conversely, high cohesion, and low alignment weights are favored for effective exploitation. Therefore, it becomes crucial to adaptively adjust these weights to strike a balance between exploration and exploitation [21, 22].

Five types of performances are assigned to the artificial dragonflies, and they are listed as follows [19, 21, 22]:

1- Separation: It is defined as the way used by dragonflies to keep themselves apart from other agents. Equation (1) is used to represent this behavior.

$$S_i = -\sum_{j=1}^{N}(X - X_j) \tag{1}$$

where $X$: is the present individual position, $X_j$: the jth nearby dragonfly's position, $N$: is the neighborhood's size.

2- Alignment: It is about figuring out how an agent (dragonfly) may determine its velocity (speed) in relation to the velocity vectors of nearby dragonflies. Equation (2) is used to represent the alignment process.

$$A_i = \frac{\sum_{j=1}^{N} V_j}{N} \tag{2}$$

where$V_j$: is the speed vector of the jth neighbor.

3- Cohesion refers to the dragonflies' tendency toward the herd center. Equation (3) defines the cohesion stage.

$$C_i = \frac{\sum_{j=1}^{N} X_j}{N} - X \tag{3}$$

4- Attraction refers to agents' desire to migrate towards food sources. Equation (4) is used to describe the *ith* agent's tendency attraction to the food source.

$$F_i = X^+ - X \tag{4}$$

where$X^+$: denotes the location of the food source.

5- Distraction: it is stated as a dragonfly's instinct to avoid predators. Equation (5) provides ith dragonfly distraction from predator.

$$E_i = X^- + X \tag{5}$$

with$X^-$: refers to the location of the predator.

Within the Dragonfly Algorithm (DA), the strategy involves utilizing the best-performing agent to update position vectors and assess the fitness of food sources. Conversely, the least effective dragonfly is tasked with updating information regarding potential threats or enemies.

This approach ensures that the algorithm converges towards the most fruitful regions of the search space while actively steering clear of less favorable areas [19].

To update the positions of dragonflies, two vectors are employed: the step vector (ΔX) and the position vector (X). The step vector, outlined in Equation (6), dictates the direction of movement for the dragonflies [19].

$$\Delta_{X_{t+1}} = (sS_i + aA_i + cC_i + fF_i + eE_i) + wX_t \quad (6)$$

where, $a$, $c$, $f$, and $e$ are the weighting vectors described above.

After computing the step vector, the position vector is determined using Equation (7) [19].

$$X_{t+1} = X_t + \Delta_{X_{t+1}} \quad (7)$$

with *t:* the number of iterations.

The Dragonfly Algorithm (DA) has demonstrated effectiveness across various optimization problems, encompassing continuous, discrete, single-objective, and multi-objective scenarios [19]. Furthermore, it has found application among numerous researchers in addressing real-world challenges spanning diverse fields, including physics, chemistry, medicine, engineering, signal processing, and robotics [23-26].

### 2.4. Optical properties determination

For a normal irradiance, Equation (8) gives the optical transmittance (T) of the thin layer that has been placed onto a transparent surface [27].

$$T = \frac{A_1 x}{A_2 - A_3 x + A_4 x^2} \quad (8)$$

where:

$$A_1 = 16\, n_s(n^2 + k^2) \quad (9)$$

$$A_2 = [(n+1)^2 + k^2][(n+1)(n + {n_s}^2) + k^2] \quad (10)$$

$$A_3 = [(n^2 - 1 + k^2)(n^2 - {n_s}^2 + k^2) - 2k^2({n_s}^2 + 1)]2\cos\varphi - k[2(n^2 - {n_s}^2 + k^2) + ({n_s}^2 + 1)(k^2 - 1 + k^2)]2\,sin\,\varphi \quad (11)$$

$$A_4 = [(n-1)^2 + k^2][(n-1)(n - {n_s}^2) + k^2] \quad (12)$$

$$\varphi = \frac{4\pi n d}{\lambda} \quad (13)$$

$$x = \exp(-\alpha\, d) \quad (14)$$

$$\alpha = \frac{4\pi k}{\lambda} \quad (15)$$

where $n_s\ and\ n$ are the substrate and the film refractive index, respectively. $d$ **:** is the thin film thickness, $k$**:** extinction coefficient, $\alpha$**:** absorption coefficients, $\lambda$: Wavelength, $\varphi$**:** phase, and $x$: absorbance.

Furthermore, dispersion refers to the fluctuation in the refractive index of a transparent material with respect to the wavelength of light. In this scenario, the refractive index of the film rises as the wavelength decreases. Several mathematical equations have been suggested for expressing dispersion formulas. Among these, the Cauchy dispersion model is widely utilized, expressed as [27]:

$$n(\lambda) = a_1 + \frac{b_1}{\lambda^2} \quad (16)$$

where$a_1, a_2, b_1$and $b_2$are Cauchy dispersion model's fitting parameters.

To ascertain the thickness (d) and the optical constants (n, k, α) of the thin layer, solving complex and nonlinear equations becomes imperative. In this method, the pivotal step involves treating the task of determining the optical constants and thin film thickness as an optimization (minimization) challenge. The objective is to minimize the Root Mean Square Error (RMSE) within the measured and estimated transmittance spectra, with the cost function represented as follows:

$$RMSE = Min\ (G) \tag{17}$$

where:

$$G = \sqrt{\sum_{i=1}^{m}[T_{meas}(i) - T_{est}\ (i, \xi)]^2/\Psi} \tag{18}$$

$T_{meas}$ and $T_{est}$ are, respectively, experimental and estimated transmittance spectra. $\xi$ is a vector containing the list of parameters that must be identified ($\xi = [a_1, b_1, d]$).

The transmittance vector's size is given by $\Psi$. This stage aims to determine the best elements of $\xi$ in such a manner that the RMSE be as lower as feasible. The effective heuristic approach of the dragonfly algorithm [19] is used to achieve this goal.

It's important to highlight that this method delivers favorable results by splitting the transmittance spectrum into two segments. The thin film thickness is determined using the transmittance data within weak and moderate absorption ranges. Furthermore, the refractive index variation, denoted as n(λ), is estimated across the entire wavelength spectrum using the obtained values of $a_1$ and $b_1$ within this interval, applied to Equation (16) for the complete wavelength spectrum. Conversely, the second segment of the spectrum addresses the high absorption region. Here, the absorption coefficient variation (α(λ)) is determined utilizing the Swanepoel approximation [28] after substituting the previously calculated values of n and d, as follows:

$$T_\alpha = \sqrt{T_M T_m} \tag{19}$$

$$G = \frac{128n^4{n_s}^2}{T_\alpha^2} + n^2(n^2-1)^2({n_s}^2-1)^2 + (n^2-1)^2(n^2-{n_s}^2)^2 \tag{20}$$

$$x = \frac{\left\{G - \left[G^2 - (n^2-1)^6(n^2-{n_s}^4)^2\right]^{1/2}\right\}^{1/2}}{(n-1)^3(n-{n_s}^2)} \tag{21}$$

$$\alpha = \frac{-\log(x)}{d} \tag{22}$$

Upper and lower tangent envelopes are represented by $T_M$ and $T_m$ in Equation (19). Following that, an extrapolation step will be established to compute the absorption coefficient variation $\alpha(\lambda)$ throughout the whole wavelength range. Finally, using Equation (15), the extinction coefficient variation $k(\lambda)$ is calculated.

## 3. Results and discussion

### 3.1. XRD analysis

X-ray diffraction patterns of ZnO and Mn-doped ZnO are shown in Figure 1. One can see from the XRD data that our samples have a single phase. For the non-annealed one, five peaks that belong to Zn metal (ICCD No.001-1238) were noticed; the corresponding planes of those peaks are (002), (100), (101), (102), and (110), respectively. No other peaks indicate the existence of ZnO, which means the oxidation of Zn occurs after the heat treatment. The main reason for the ZnO oxide phase's disappearance is the subdivision of ZnO molecules during the evaporation process, giving Zn atoms and oxygen gas. This last will be pumped majoritively by the pumping group, which prevents the ZnO phase creation [29]. Concerning the annealed samples, analysis based on the powder diffraction standard card (ICCD No.001-1136) reveals distinct peaks. Those

with higher intensities, such as those corresponding to the planes (100), (002), and (101), as well as peaks with lower intensities like (102), (110), (103), and (112), collectively signify the presence of the hexagonal wurtzite structure characteristic of ZnO. This observation suggests that the ZnO mesh was disturbed when the Mn concentration was raised. It's likely that throughout the annealing process, Mn atoms operate as barriers (traps or dispersion centers) that prevent ZnO from developing, causing the film's crystallinity to deteriorate and the peak's intensity to drop. Many research works [30, 31] have reported on this fact. In addition, the examination of the XRD patterns reveals that the peaks of Mn-doped films are somewhat displaced to a lower angle than those of the undoped ZnO films. The structure's micro-strain from vacancies, stacking faults, and interstitials may have caused this shift [32]. Nevertheless, the absence of peaks characteristic of manganese (Mn) indicates that Mn has likely replaced zinc (Zn) sites within the wurtzite structure without altering its fundamental characteristics.

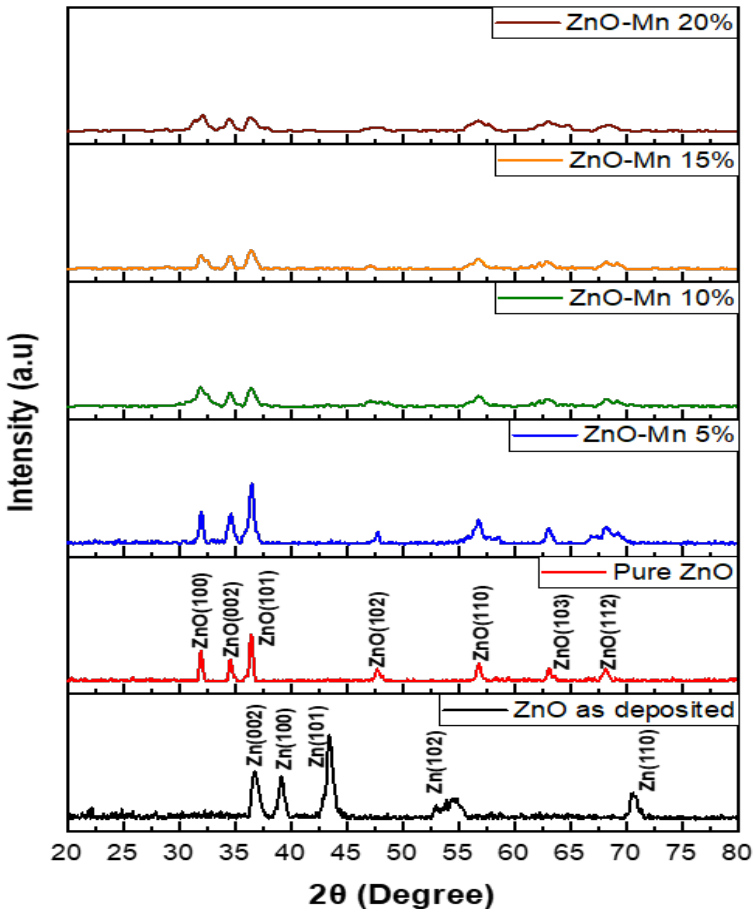


*Fig. 1. X- ray diffraction patterns of pure and doped zinc oxide films.*

Identifying any modifications in these structural characteristics is advantageous to gain insights into the alterations in the physical properties of our layers. The lattice parameters were established using [33]:

$$a = \frac{\lambda}{sin\theta_{hkl}\sqrt{3}} \tag{23}$$

$$c = \frac{\lambda}{sin\theta_{hkl}} \tag{24}$$

In this equation, λ represents the wavelength of the X-ray, $\theta_{hkl}$ denotes the diffraction angle, and hkl refers to the Miller indices.

The formulas used to calculate the crystallite size D, microstrain τ, and dislocation density δ are as follows [34]:

$$D = \frac{0.9\lambda}{FWHM cos\theta_{hkl}} \tag{25}$$

$$\tau = \frac{FWHM}{4tan\theta_{hkl}} \tag{26}$$

$$\delta = \frac{1}{D^2} \tag{27}$$

The lattice parameters of our samples barely changed after adding different amounts of Mn; this phenomenon can be explained by the similarity in the radii of manganese (Mn) ions (0.66 Å) and zinc (Zn) ions (0.60 Å), facilitating the straightforward substitution of Zn atoms with Mn atoms. The 'c' axes values variation began with an unnoticed increase at 5 wt.-% Mn doping, then it increases with Mn concentration rise (Figure 2a). All 'c' values exceed the value of theoretical pure zinc oxide ($c_0$= 0.5205 nm). This implies that ZnO sheets experience compressive forces along the c-axis [35]. In Figure 2b, the full width at half-maximum (FWHM) of the thin films increases as the quantity of Mn incorporated rises. This augmentation in FWHM is ascribed to the reduction in crystallite size induced by doping. The lowest FWHM value is observed for pure ZnO films, suggesting the highest level of crystallinity. The widening of the diffraction peaks is a results of the increase of strain, lattice defects, and dislocation density, which leads to a reduction in crystallite size. This highlights the influence of the incorporation of Mn atoms [36].

*Table 1. Crystallites size D, FWHM, micro strain τ, dislocation density δ and lattice parameters.*

| | D (nm) | FWHM (rad) | τ | δ ($nm^{-2}$) | a (nm) | c (nm) |
|---|---|---|---|---|---|---|
| Pure ZnO | 24.26 | 0.3447 | 0.0046 | 0.0017 | 0.3214 | 0.5247 |
| Mn:ZnO(5 wt.-%) | 15.61 | 0.5359 | 0.0071 | 0.0041 | 0.3213 | 0.5249 |
| Mn:ZnO(10 wt.-%) | 10.64 | 0.7855 | 0.0104 | 0.0088 | 0.3220 | 0.5256 |
| Mn:ZnO(15 wt.-%) | 10.08 | 0.8290 | 0.0110 | 0.0098 | 0.3224 | 0.5259 |
| Mn:ZnO(20 wt.-%) | 8.93 | 0.9361 | 0.0125 | 0.0125 | 0.3228 | 0.5265 |

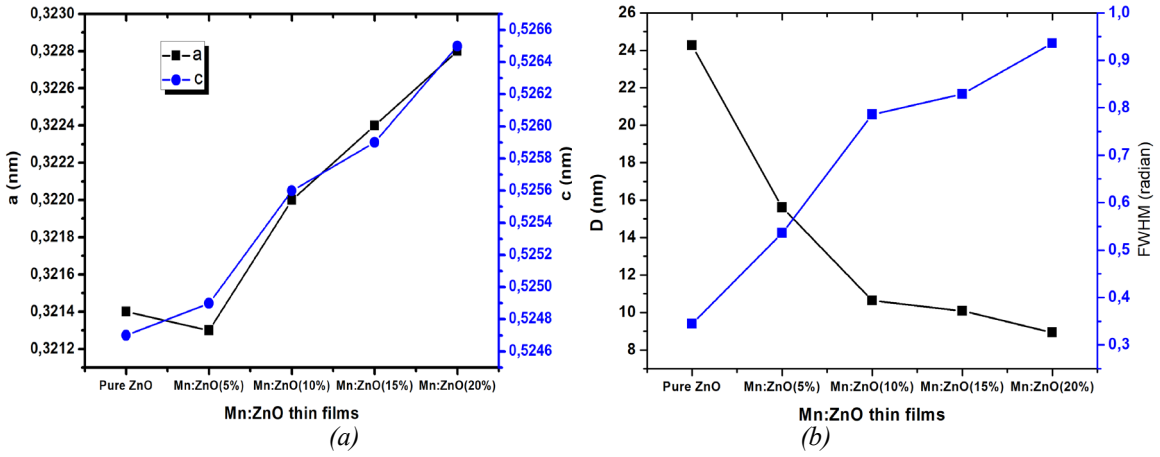


*Fig. 2. Variation of a) lattice parameters 'a' and 'c' b) FWHM, crystallites size D of ZnO mesh as a function of Mn content.*

### 3.2. Raman analysis

The Raman scattering technique was employed to analyze the vibrational characteristics of the hexagonal wurtzite structure present in both pure and doped zinc oxide layers. The findings are illustrated in Figure 3. It is evident that all samples exhibit the $A_1$(LO) vibration mode, with frequencies around Σ 572 $cm^{-1}$ for Mn:ZnO films and 569 $cm^{-1}$ for pure zinc oxide. The $A_1$ longitudinal optical phonon in the wurtzite structure of zinc oxide is polarized parallel to the c-axis; this vibration mode gives the oxidation state of the films. Within doped films, the introduction of manganese atoms occurs within the zinc oxide host lattice. Conversely, in pure zinc oxide films, the process of incomplete oxidation leads to the integration of zinc atoms into the zinc oxide lattice, thereby inducing self-doping [37].

The incorporation of a dopant into the mesh may result in the appearance of local vibration modes (LVM) in the Raman spectra. The disruption of the crystal's translational symmetry by impurity-induced defects is one proposed physical basis for understanding LVM. Due to the wave vector's loss of conservation, phonon scattering with wave vectors far from the Brillouin zone occurs [38]. Because of the surplus of Mn atoms within the ZnO matrix, LVM modes can be found clearly for Mn:ZnO (15 wt.-% and 20 wt.-% Mn) samples. However, for the pure ZnO films, the disappearance of this vibration mode can be noticed. The rest of the detected peaks for the Mn:ZnO films (887 and 847 $cm^{-1}$) may be attributed to the molecules with Mn [39]. $A_1$(LO)+$E_2$(Low) mode for the high doped films is related to poly-phonon scattering [40]. Vibration modes at 706 $cm^{-1}$ and 900 $cm^{-1}$ for pure ZnO samples are given $A_1$ symmetry of ZnO processes that combine LA+TO phonons [41].

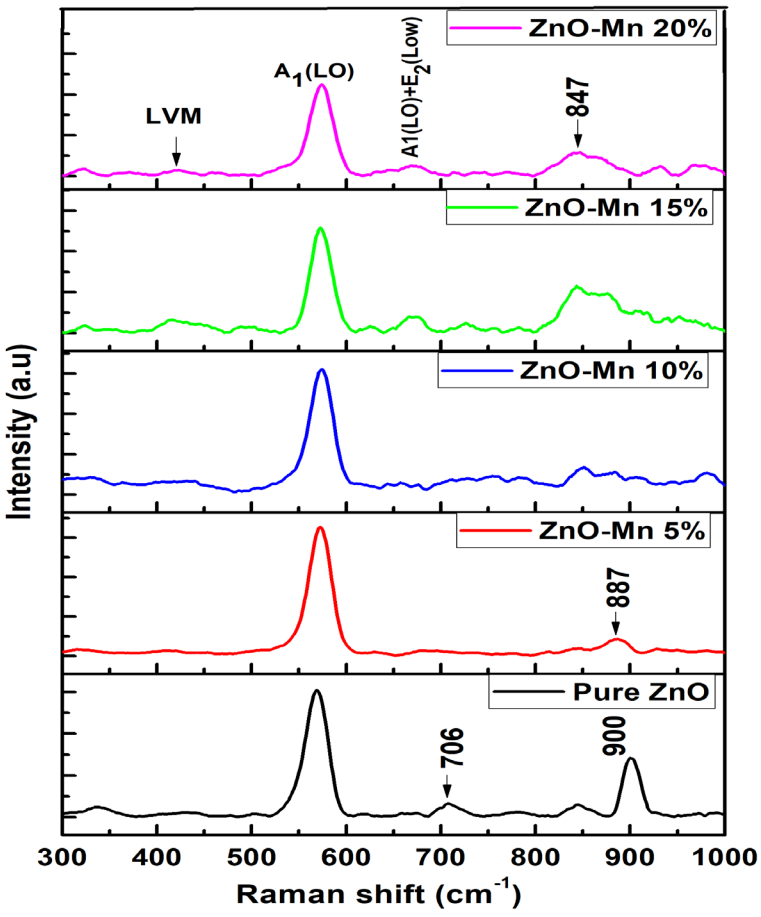


*Fig. 3. Raman shift for pure and doped zinc oxide films.*

### 3.3. Surface morphology

SEM was utilized to analyze the surface morphology of the non-doped and doped layers. The outcomes are depicted in Figure 4 (a-e). It is clear from the electron micrographs that all substrates are well covered with the thin layer, showing a non-uniform surface morphology. Pure ZnO film shows spherical particles agglomerations spread unevenly onto the substrate with an average size of 5.36 µm. It is apparent that Mn doping modified the morphology to become more homogenous; the agglomerations are closely packed, with grain size noticeably smaller than the non-doped films. Due to the impact nature of ZnO clusters, pits and holes that signify the escape of gases during thermal evaporation were observed. The chemical composition was analyzed using EDX. It confirms the existence of Zn, Mn, and O atoms. There are pics indicating the Si corresponding to the glass substrate.

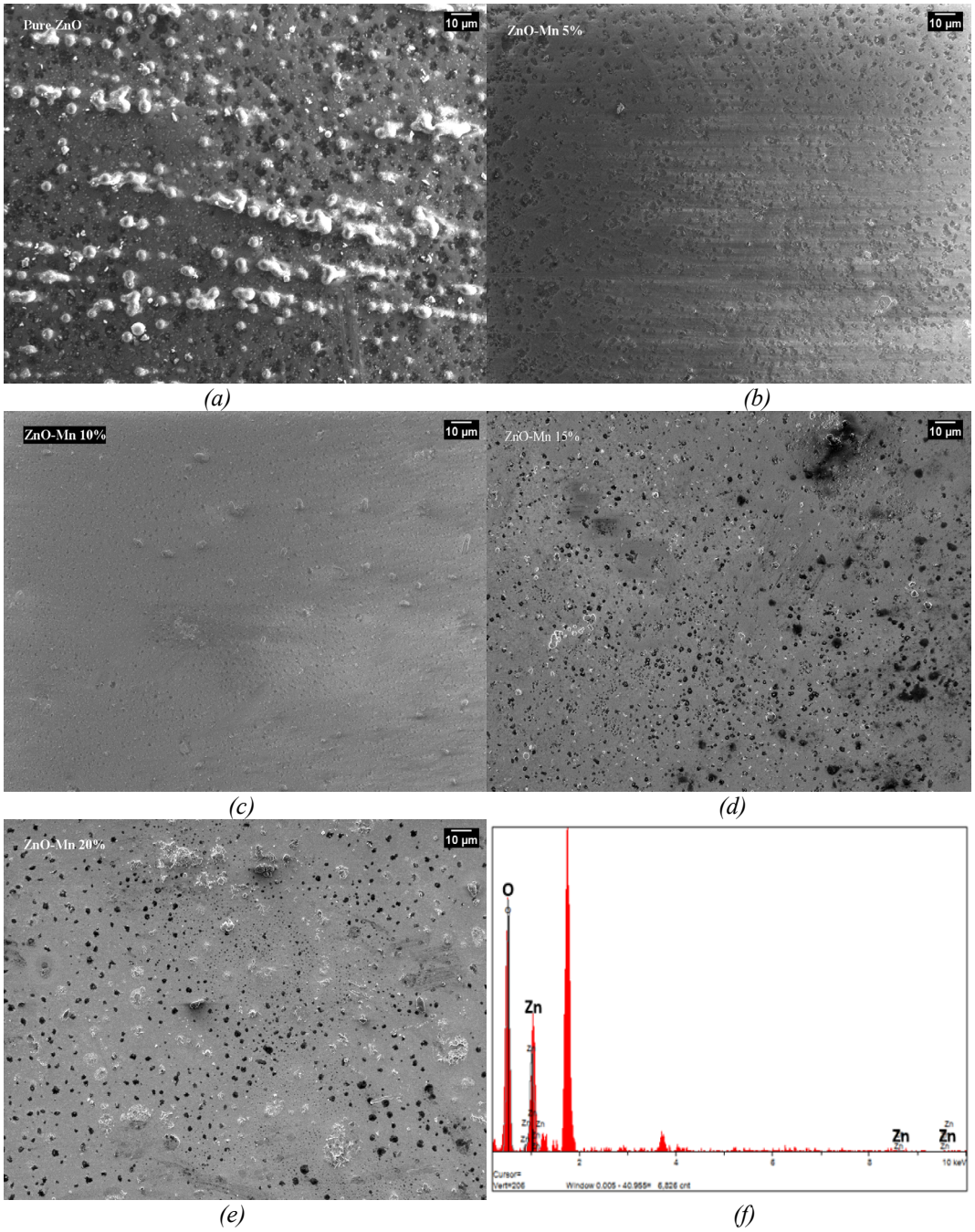


*Fig. 4. SEM images of layers: (a) pure ZnO, (b) ZnO-Mn 5%, (c) ZnO-Mn 10%, (d) ZnO-Mn 15%, (e) ZnO-Mn 20% and (f) EDX results for 20% doping.*

### 3.4. Optical properties

The optical transmission spectra of our samples were recorded in the wavelength region of 250-800 nm in Figure 5. The thickness of the layers is calculated using the DA algorithm, which is about 120 nm. Each sample demonstrates transparency within the visible spectrum, with the pure ZnO film exhibiting the highest transmission at 83.1%.

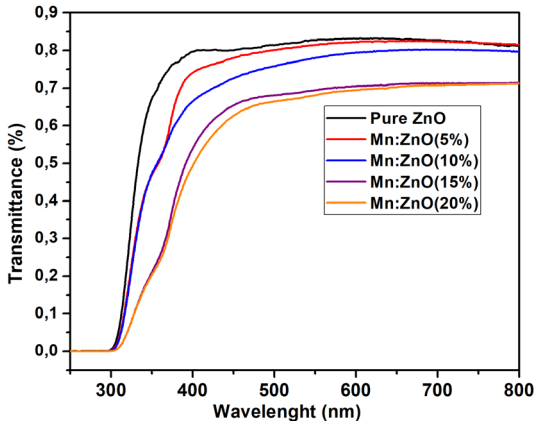


*Fig. 5. Spectra depicting the optical transmittance of both pure and doped zinc oxide films.*

The increase in Mn percentage causes a decrease in optical transmission, up to 69.5% for Mn:ZnO (20 wt.-%Mn), and this might be due to the light loss caused by oxygen vacancies and diffusion at grain boundaries [42]. The decline in transmittance observed as the percentage of Mn increases is attributed to the reduction in optical diffusion [31], which is linked to a decrease in the grain size and to the increase in the density of grain boundaries. These results are in perfect adequation with the XRD analysis section, and the grain size decreases with the manganese amount increase.

The consistency between the measured and estimated transmittance is apparent for all samples. As an example, the case of the sample with 20 wt.-% Mn doping is detailed. Figure 6 confirms that the dragonfly algorithm successfully determined the optical parameters of our films, the measured transmittance and the estimated one are almost identical, and the root mean square estimated by Equation (18) is around 0.00145.

The transmittance spectrum of Mn-doped ZnO thin films has been analyzed using the DA algorithm to showcase the efficacy of this methodology, for the sample containing a 20 wt.-% Mn doping concentrate, a thorough explanation will be provided with illustrations. Additionally, as mentioned in Section (2-4), the user can adjust several control settings for the DA algorithm. These parameters were empirically selected for this study using a trial-and-error methodology. This indicates that the DA algorithm's effectiveness has been evaluated for a number of values, and only the best ones are chosen. Table 2 in this paper provides an overview of the Dragonfly Algorithm's configuration parameters.

*Table 2. Setting parameters of DA.*

| **Parameter** | **Value** |
|---|---|
| Population size | 80 |
| Number of iterations | 200 |
| Dimension | 5 |
| Separation weight | 0.1 |
| Alignment weight | 0.1 |
| Cohesion weight | 0.7 |
| Food factor | 1 |
| Enemies factor | 1 |

The variation ranges of each parameter are depicted in Table 3.

*Table 3. The variation ranges of every parameter.*

| Parameter | variation range |
|---|---|
| $\alpha_1$ | [1 – 3] |
| $\beta_1$ | [$10^4$ – $10^6$] |
| $\alpha_2$ | [$10^{-5}$ – $10^{-2}$] |
| $\beta_2$ | [$10^3$ – $10^5$] |
| D | [60 – 400] |

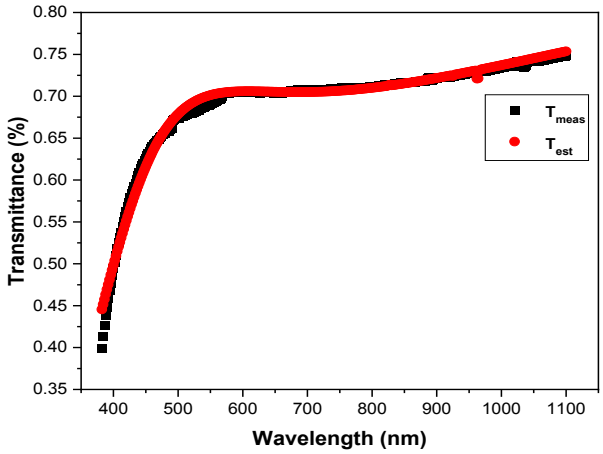


*Fig. 6. Measured and estimated transmittance for 20wt.-% Mn doped ZnO.*

For instance, the obtained optimal parameters and reached RMSE for the Mn:ZnO (20wt.-%) are given in Table 4.

*Table 4. The obtained results for Mn:ZnO (20wt.-%).*

| Parameters | $\alpha_1^*$ | $\beta_1^*$ | $\alpha_2^*$ | $\beta_2^*$ | $d^*$ | $RMSE$ |
|---|---|---|---|---|---|---|
| Value | 2.05 | $7.17\times10^{+04}$ | $3.77\times10^{-4}$ | $1.64\times10^{+4}$ | 105 | $1.45\times10^{-03}$ |

Additionally, the results in Table 4 clearly illustrate the DA algorithm's outstanding performance in precisely determining the optical film thickness and Cauchy dispersion parameters. The low RMSE value of $1.45\times10^{-03}$ confirms the high accuracy of the approach.

The refractive index can be rewritten as follows using the Table 4 parameters:

$$n(\lambda) = 2.05 + \frac{7.17\times10^{+4}}{\lambda^2} \tag{28}$$

The entire wavelength range can be extrapolated using this equation to determine n. The estimated values of n are shown in Figure 7.

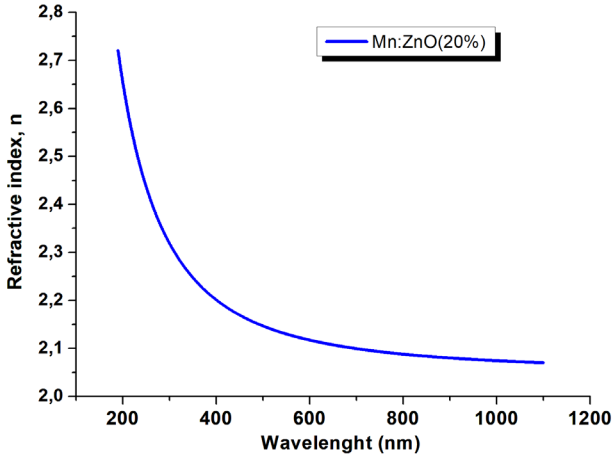


*Fig. 7. The dispersion of refractive index n for the whole wavelength range.*

The determination of the static refractive index involves setting the variable of the Cauchy relation model in Equation (28) to "approaches infinity". The measured values for pure and manganese doped zinc oxide samples (5, 10, 15 and 20 wt.-%) are 1.76, 1.90, 1.92, 2.112 and 2.17, respectively. With a rise in Mn doping, the refractive index at a wavelength of 600 nm is determined to be 1.785, 1.925, 1.952, 2.142, and 2.197. A rise in the refractive index was observed with an increase in the amount of manganese. Few studies in the existing literature have investigated the impact of manganese concentration on the refractive index of zinc oxide. However, the same results were reported by Shaaban et al. [43], which was explained by the increase of polarization resulting from Mn incorporation. P. Singh and R. Kumar [44] reported similar results, but for Er-doped ZnO films, they found that the concentration of erbium increases the refractive index of the material and because of its power of polarizability. Erbium ions ($Er^{3+}$) have the most empty outer orbital will bring the material back towards linear polarizability, which increases the refractive index of the material. The same can be said for Mn and its influence on Mn:ZnO thin films. For the calculated extinction coefficient based on the values of the absorption coefficient α, using Equation (22). The values depicted in Table 5 are practically the same for the layers not doped and doped at 5 and 10 wt.-%. However, the value of k increases when the doping becomes important (15 and 20 wt.-%).

As depicted in Figure 8, the graphs illustrate plots of $(\alpha h\upsilon)^2$ against $(h\upsilon)$. The optical band gap of the thin films was determined by extrapolating the linear portion of the curve to reach $(\alpha h\nu)^2 = 0$. This calculation is performed using the following formula [45, 46]:

$$\alpha h\upsilon = A\sqrt{h\upsilon - Eg} \tag{29}$$

The optical band gap of the zinc oxide film measures 3.95 eV, showing a slight reduction to 3.79 eV after Mn doping, reaching this value at 20 wt.-% Mn. The decrease in band gap upon doping ZnO with varying concentrations of Mn is theoretically linked to the exchange interaction between the electrons of the sp orbital of ZnO and the Mn d orbital [47]. On the other hand, many researchers explain the change in band gap $E_g$ by the strains in semiconductor films, it can be explained by the following empirical expression [48]:

$$E_g = 3.28 - 0.045\varepsilon_z \tag{30}$$

The strains ($\varepsilon_z$ ) values can be calculated based on c-axis values determined in the XRD section and using this formula [49]:

$$\varepsilon_z = \left(\frac{c - c_0}{c_c}\right) \tag{31}$$

The films band gap will increase for negative strain and decrease for positive strain; according to Equation (32), $\varepsilon z$values are +0.0080, +0.0084, +0.0098,, 0.0103 and 0.0115 for pure ZnO and Mn:ZnO films (5, 10, 15 and 20 wt.-%), respectively. Since$\varepsilon_z$ has positive values in our situation, which conduct to the Eg rising (Figure 9).

*Table 5. The parameters examined include the band gap (Eg), transmittance (T), refractive index (n), and extinction coefficient (k) of both the non-doped and doped samples.*

| | Eg (eV) | T (%) (λ=600) | N ( λ=600) | $n_0$(static) | k (λ=600) | $k_0$(static) |
|---|---|---|---|---|---|---|
| Pure ZnO | 3.95 | 83.1 | 1.785 | 1.760 | 0.013 | 0.039 |
| Mn:ZnO (5wt.-%) | 3.91 | 82.2 | 1.925 | 1.900 | 0.018 | 0.040 |
| Mn:ZnO(10wt.-%) | 3.88 | 79.5 | 1.952 | 1.920 | 0.015 | 0.035 |
| Mn:ZnO (15wt.-%) | 3.82 | 70.4 | 2.142 | 2.112 | 0.072 | 0.084 |
| Mn:ZnO (20wt.-%) | 3.79 | 69.5 | 2.197 | 2.170 | 0.064 | 0.057 |

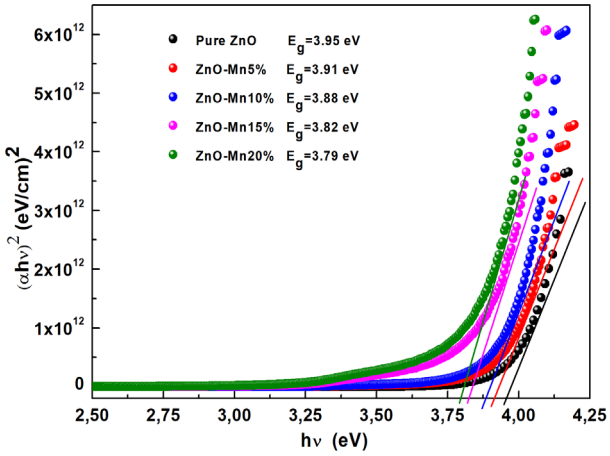


*Fig. 8. The plots of $(\alpha h\nu)^2$ as function of photon energy of non-doped and Mn-doped zinc oxide thin films.*

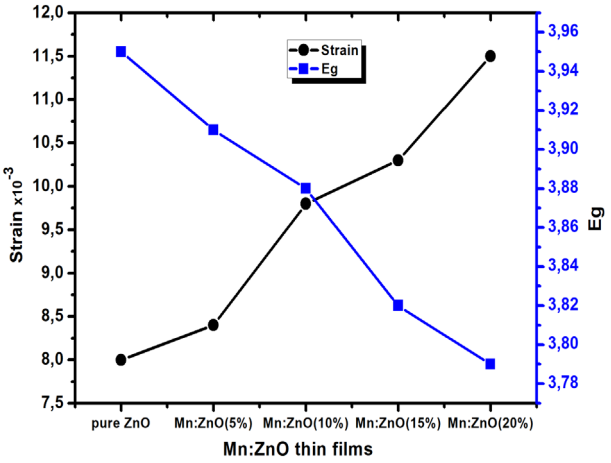


*Fig. 9. The changes in band gap (Eg) and strain ($\varepsilon_z$) with respect to the concentration of Mn doping are examined in this study.*

## 4. Conclusion

This study meticulously explores the structural and optical characteristics of Mn-doped ZnO thin films across varying concentrations of Mn doping. The samples were made using the rapid thermal evaporation of ZnO and Mn particles in combination. Following annealing, Mn:ZnO layers form in the hexagonal wurtzite phase with an increase in c-axis and crystallite size decrease, according to XRD studies. Raman measurements have shown the desapearance of the combined vibrations modes LA+TO after doping with Mn and the appearance of $A_1(LO)+E_2(Low)$ mode for the high doping samples (15 and 20 %).

The average optical transmittance for the annealed Mn:ZnO layers was decreased with Mn doping concentration increase from 83.1 to 69.5%. For the first time, the Dragonfly Algorithm was used to correctly identify and calculate the optical constants n, α, k and the thickness d using only the transmittance spectra. Furthermore, the energy band gap Eg was calculated for various Mn doping levels. According to the obtained data, Eg reduces from 3.95 to 3.79 eV as Mn doping concentration increases from 0 to 20 wt.-%.

## References

[1] H. Kim, A. C. Gilmore, A. Pique, J. Horwitz, H. Mattoussi, H. Murata et al., " Journal of applied physics, vol. 86, pp. 6451-6461, 1999; https://doi.org/10.1063/1.371708

[2] Z. Chen, W. Li, R. Li, Y. Zhang, G. Xu, H. Cheng, Langmuir, vol. 29, pp. 13836-13842, 2013; https://doi.org/10.1021/la4033282

[3] S. K. Kim, K. M. Kim, D. S. Jeong, W. Jeon, K. J. Yoon, C. S. Hwang, Journal of Materials Research, vol. 28, pp. 313-325, 2013; https://doi.org/10.1557/jmr.2012.231

[4] M. Becker, R. Hamann, A. Polity, B. K. Meyer, Thin Solid Films, vol. 553, pp. 26-29, 2014; https://doi.org/10.1016/j.tsf.2013.11.030

[5] F. Lekoui, R. Amrani, S. Hassani, E. Garoudja, W. Filali, S. Oussalah et al., Zeitschrift für Naturforschung A, 2023; https://doi.org/10.1515/zna-2023-0046

[6] F. Lekoui, R. Amrani, S. Hassani, Elyes Garoudja, Walid Filali, M. Ouchabane et al, Optical Materials, vol. 150, p. 115151, 2024; https://doi.org/10.1016/j.optmat.2024.115151

[7] A. Mallick, S. Ghosh, D. Basak, Materials Science in Semiconductor Processing, vol. 119, p. 105240, 2020; https://doi.org/10.1016/j.mssp.2020.105240

[8] F. Lekoui, R. Amrani, W. Filali, E. Garoudja, L. Sebih, I. E. Bakouk et al., Optical Materials, vol. 118, p. 111236, 2021; https://doi.org/10.1016/j.optmat.2021.111236

[9] S. V. Bhat, F. Deepak, Solid State Communications, vol. 135, pp. 345-347, 2005; https://doi.org/10.1016/j.ssc.2005.05.051

[10] A. Vincze, J. Bruncko, M. Michalka, D. Figura, Open Physics, vol. 5, pp. 385-397, 2007; https://doi.org/10.2478/s11534-007-0027-4

[11] Kamil, A. A., Bakr, N. A., Mubarak, T. H., Al-Zanganawee, Journal of Ovonic Research, 18(3), 431-442, 2022; https://doi.org/10.15251/JOR.2022.183.431

[12] Zaouche, C., Dahbi, L., Benramache, S., Harouache, A., Derouiche, Y., Kharroubi, M., Alkhojah, H. M., Journal of Ovonic Research, 19(2), 2023; https://doi.org/10.15251/JOR.2023.192.197

[13] A. Ashour, M. Kaid, N. El-Sayed, A. Ibrahim, Applied Surface Science, vol. 252, pp. 7844-7848, 2006; https://doi.org/10.1016/j.apsusc.2005.09.048

[14] S. Faÿ, J. Steinhauser, S. Nicolay, C. Ballif, Thin Solid Films, vol. 518, pp. 2961-2966, 2010; https://doi.org/10.1016/j.tsf.2009.09.189

[15] J. Elanchezhiyan, P. Bhuvana, N. Gopalakrishnan, A. Thamizhavel, T. Balasubramanian, Zeitschrift für Naturforschung A, 63 (9), PP. 585-590, 2008; https://doi.org/10.1515/zna-2008-0909

[16] X. Liu, R. Hao, Q. Zhao, F. Chang, Y. Li, K. Gu et al., (2018), Zeitschrift für Naturforschung

A, 73 (10), pp. 957-964, 2018; https://doi.org/10.1515/zna-2018-0177
[17] S. Baturay, O. Bicer, S. Yigit Gezgin, I. Candan, H. Budak Gumgum, H. Kilic, Zeitschrift für Naturforschung A, 78(6), pp. 563-578, 2023; https://doi.org/10.1515/zna-2023-0015
[18] A. Zaier, A. Meftah, A. Jaber, A. Abdelaziz, M. Aida, Journal of King Saud University-Science, vol. 27, pp. 356-360, 2015; https://doi.org/10.1016/j.jksus.2015.04.007
[19] S. Mirjalili, Neural computing and applications, vol. 27, pp. 1053-1073, 2016; https://doi.org/10.1007/s00521-015-1920-1
[20] E. Garoudja, R. Amrani, W. Filali, F. Lekoui, S. Oussalah, Y. Cuminal et al., Optik, vol. 241, p. 167030, 2021; https://doi.org/10.1016/j.ijleo.2021.167030
[21] W. Filali, R. Amrani, E. Garoudja, S. Oussalah, F. Lekoui, Z. Oukerimi et al., Superlattices and Microstructures, vol. 160, p. 107085, 2021; https://doi.org/10.1016/j.spmi.2021.107085
[22] Y. Meraihi, A. Ramdane-Cherif, D. Acheli, M. Mahseur, Neural Computing and Applications, vol. 32, pp. 16625-16646, 2020; https://doi.org/10.1007/s00521-020-04866-y
[23] D. Poelman, P. F. Smet, Journal of Physics D: Applied Physics, vol. 36, p. 1850, 2003; https://doi.org/10.1088/0022-3727/36/15/316
[24] C. M. Rahman, T. A. Rashid, A. Alsadoon, N. Bacanin, P. Fattah, S. Mirjalili, Evolutionary Intelligence, vol. 16, pp. 1-21, 2023; https://doi.org/10.36227/techrxiv.11811768.v4
[25] M. Mafarja, A. A. Heidari, H. Faris, S. Mirjalili, I. Aljarah, Nature-Inspired Optimizers: Theories, Literature Reviews and Applications, pp. 47-67, 2020; https://doi.org/10.1007/978-3-030-12127-3_4
[26] Yıldız, Betül Sultan, Yıldız, Ali Rıza, Materials Testing, vol. 61, no. 8, pp. 744-748, 2019; https://doi.org/10.3139/120.111379
[27] Z.-H. Ruan, Y. Yuan, X.-X. Zhang, Y. Shuai, H.-P. Tan, Solar Energy, vol. 127, pp. 147-158, 2016; https://doi.org/10.1016/j.solener.2016.01.027
[28] R. Swanepoel, Journal of Physics E: Scientific Instruments, vol. 16, p. 1214, 1983; https://doi.org/10.1088/0022-3735/16/12/023
[29] F. Lekoui, S. Hassani, E. Garoudja, R. Amrani, W. Filali, O. Sifi, S. Oussalah, Rev. Mex. Fís., vol. 69, p. 051005, 2023; https://doi.org/10.31349/RevMexFis.69.051005
[30] S. Ahmed, Results in physics, vol. 7, pp. 604-610, 2017; https://doi.org/10.1016/j.rinp.2017.01.018
[31] A. López-Suárez, D. Acosta, C. Magaña, F. Hernández, Journal of Materials Science: Materials in Electronics, vol. 31, pp. 7389-7397, 2020; https://doi.org/10.1007/s10854-019-02830-8
[32] R. Baghdad, B. Kharroubi, A. Abdiche, M. Bousmaha, M. Bezzerrouk, A. Zeinert et al., Superlattices and Microstructures, vol. 52, pp. 711-721, 2012; https://doi.org/10.1016/j.spmi.2012.06.023
[33] M. Boshta, M. Abou-Helal, D. Ghoneim, N. Mohsen, R. Zaghlool, Surface and Coatings Technology, vol. 205, pp. 271-274, 2010; https://doi.org/10.1016/j.surfcoat.2010.06.039
[34] J. Li, D. Yang, X. Zhu, H. Sun, X. Gao, P. Wangyang et al., Journal of Sol-Gel Science and Technology, vol. 82, pp. 563-568, 2017; https://doi.org/10.1007/s10971-017-4335-x
[35] M. Mekhnache, A. Drici, L. S. Hamideche, H. Benzarouk, A. Amara, L. Cattin et al., Superlattices and Microstructures, vol. 49, pp. 510-518, 2011; https://doi.org/10.1016/j.spmi.2011.02.002
[36] S. Hemathangam, G. Thanapathy, S. Muthukumaran, Journal of Materials Science: Materials in Electronics, vol. 27, pp. 1791-1798, 2016; https://doi.org/10.1007/s10854-015-3955-6

[37] S. Khosravi-Gandomani, R. Yousefi, F. Jamali-Sheini, N. M. Huang, Ceramics international, vol. 40, pp. 7957-7963, 2014; https://doi.org/10.1016/j.ceramint.2013.12.145
[38] J. Li, D. Yang, X. Zhu, Aip Advances, vol. 7, 2017; https://doi.org/10.1063/1.4985753
[39] J. Wang, G. Huang, X. Zhong, L. Sun, Y. Zhou, E. Liu, Applied Physics Letters, vol. 88, 2006; https://doi.org/10.1063/1.2208564
[40] K. Hamidian, M. Sarani, M. Barani, F. Khakbaz, Arabian Journal of Chemistry, vol. 15, p. 103792, 2022; https://doi.org/10.1016/j.arabjc.2022.103792
[41] R. Cuscó, E. Alarcón-Lladó, J. Ibáñez, L. Artús, J. Jiménez, B. Wang et al., Physical Review B, vol. 75, p. 165202, 2007; https://doi.org/10.1103/PhysRevB.75.165202
[42] H. K. Yadav, K. Sreenivas, V. Gupta, Journal of Applied Physics, vol. 99, 2006; https://doi.org/10.1063/1.2188083
[43] E. Shaaban, M. El-Hagary, M. Emam-Ismail, A. Matar, I. Yahia, Materials Science and Engineering: B, vol. 178, pp. 183-189, 2013; https://doi.org/10.1016/j.mseb.2012.11.005
[44] P. Singh, R. Kumar, Optik, vol. 246, p. 167829, 2021; https://doi.org/10.1016/j.ijleo.2021.167829
[45] R. Amrani, E. Garoudja, F. Lekoui, W. Filali, H. Neggaz, Y. A. Djebeli et al., Bulletin of Materials Science, vol. 46, p. 8, 2023; https://doi.org/10.1007/s12034-022-02845-8
[46] D. Grine, H. Akkari, P. Fernández, T. Mekhalif, S. Hassani, F. Lekoui, Physica Status Solidi A, vol. 219, p. 2200036, 2022; https://doi.org/10.1002/pssa.202200036
[47] M. Shatnawi, A. Alsmadi, I. Bsoul, B. Salameh, M. Mathai, G. Alnawashi et al., Results in Physics, vol. 6, pp. 1064-1071, 2016; https://doi.org/10.1016/j.rinp.2016.11.041
[48] L. Peng, L. Fang, X. Yang, Y. Li, Q. Huang, F. Wu et al., Journal of Alloys and Compounds, vol. 484, pp. 575-579, 2009; https://doi.org/10.1016/j.jallcom.2009.04.139
[49] H. Chen, J. Ding, W. Guo, F. Shi and Y. Li, Applied surface science, vol. 258, pp. 9913-9917, 2012; https://doi.org/10.1016/j.apsusc.2012.06.050

# Studying the Effect of Mn Doping on the Electrical and Optical Properties of ZnO/Ag/ZnO Multilayer

**Khaoula Settara, Fouaz Lekoui, Rachid Amrani, Elyes Garoudja, Ouissam Bouacha, Hadjer Asmaa Zerini, Walid Filali, and Hocine Akkari**

**Abstract** In this work, we investigated the effect of Mn doping on the optical and electrical properties of ZnO/Ag/ZnO transparent conductive oxide (TCO) multilayers deposited on a glass substrate using a rapid thermal evaporation technique. The structure and optoelectronic properties were studied using X-ray diffraction (XRD), UV–Vis spectroscopy, and a Four-point probe. XRD patterns show the existence of five peaks indicating the hexagonal structure of ZnO with lattice parameters: a = 3.27–3.35 Å and c = 5.34–5.47 Å and three peaks of the Ag deposited as the interlayer. It was observed that Mn was incorporated without changing the hexagonal structure of ZnO. The results show an increase in band gap energy from 3.38 to 3.81 eV by doping. Compared to non-doped ZnO thin film multilayers, the sheet resistance decreased from 271.8 to 163.08 Ω. The optimum figure of merit at $4.73 \times 10^{-3}\ \Omega^{-1}$ was achieved for Mn doped ZnO multilayers with 77.1% transmission.

**Keywords** TCO · ZnO/Ag/ZnO · Thermal evaporation · Optoelectronic properties · Figure of merit

K. Settara (✉)
Laboratoire de Recherche sur la Physico- Chimie des Surfaces et Interfaces, Université 20 Aout 1955, Skikda, Algeria
e-mail: kh.settara@univ-skikda.dz

Groupe des Matériaux Fonctionnels, Laboratoire LGMM, Université, 20 Aout 1955, Skikda, Algeria

F. Lekoui
Division Milieux Ionisés & Laser, Centre de Développement des Technologies Avancées, Cité 20 Août 1956, Baba Hassen, Alger, Algérie

R. Amrani · O. Bouacha · H. A. Zerini
Département des Sciences de la Matière, Université Alger1 Benyoucef Benkhedda, Alger, Algeria

E. Garoudja · W. Filali
Plateforme Technologique de Micro-fabrication, Centre de Développement des Technologies Avancées, Cité 20 Août 1956, Baba Hassen, Alger, Algeria

H. Akkari
Département de Génie Industriel, Faculté de Technologie, Université Batna 2 Chahid Mostefa Benboulaid, 53, Route de Constantine. Fésdis, 05078 Batna, Algeria



S. Ziani et al. (eds.), *Proceedings of the 5th International Conference on Electrical Engineering and Control Applications–Volume 2*, Lecture Notes in Electrical Engineering 1224, https://doi.org/10.1007/978-981-97-4776-4_19

## 1 Introduction

Due to the enormous demographic growth and technological development, the demand for energy increases every day with the need to obtain environmentally friendly sources and reduce pollution as much as possible, making renewable energies the ideal solution to meet these requirements, which motivated many researchers in this field [1–3]. Recently, transparent conducting electrodes (TCE) attracted much attention showing a combination of good optical transparency and high electrical conductivity. However, combining these two properties is a priori contradictory. Indeed, a transparent material in the visible range has high gap energy (greater than 3 eV), preventing the absorption of visible light, and making it insulated. Thus, a material with excellent electrical conductivity is not transparent. A semiconductor is transparent in the visible range but has poor conductivity. Doping it with a low atomic percentage of metal can make it conductive. Today's most widely used transparent conducting oxides (TCO) is indium doped tin oxide (ITO) [4–6]. However, many studies aim to replace ITO with less toxic and less expensive TCO. Zinc oxide is a promising candidate due to its abundance on earth and properties, mainly doped with gallium [7], titanium [8], molybdenum [9], magnesium [10], aluminum [11], or manganese [12]. Another critical issue in TCO is the optical and electrical losses [13, 14]. An oxide/metal/oxide multilayer structure has been introduced to overcome this problem. In this work, the investigation of low percentage (5%) Mn doping effect on the structural, optical and electrical properties of ZnO/Ag/ZnO multilayer thin films grown by rapid (flash) thermal evaporation technique is the primary contribution. The results of this innovative study's comparison of ZnO/Ag/ZnO and Mn:ZnO/Ag/Mn:ZnO TCO revealed several intriguing effects.

## 2 Experimental

High-purity ZnO, Mn, and Ag powders (99.99% purity purchased from Sigma-Aldrich) were used to prepare ZnO/Ag/ZnO and Mn:ZnO/Ag/Mn:ZnO (5%Mn) multi-layers. The vacuum thermal evaporation was carried out with a device mounted at the Center for the Development of Advanced Technologies (CDTA). We deposited the first layer of ZnO on an ordinary glass substrate than another layer of Ag and a final layer of ZnO. The same steps were done for Mn Doped ZnO multilayers. The samples were then annealed using a furnace at 400 °C for one hour. The structure of the multilayers films was studied by X-ray diffraction analysis (XRD) using a Philips X'pert MPD diffractometer with a Cu-Kα cathode source and 1.54 Å of wavelength. The electrical properties were measured using Four-point probe technique while the optical transmittance was investigated using UV–Vis spectroscopy in the wavelength range of 200–1100 nm. The films thickness and the optical parameters like refractive index n, extinction coefficient k and absorption coefficient α were extracted using

our method based on PSO algorithm. Details on this method were provided in our earlier study [12].

## 3 Results and Discussion

Powder X-ray diffraction patterns of the non-doped and doped multilayers are shown in (Fig. 1). We notice five peaks corresponding to the planes (100), (002), (101), (110), and (103), which indicate the hexagonal wurtzite structure of ZnO according to the powder diffraction standard card No. 01-079-2205. Three peaks indicate the cubic structure of Ag with the planes respectively (111), (200), and (220) (standard card No. 00-001-1164).

No peak indicates the existence of Mn, which could be explained by the fact that Mn ions have substituted Zn ions without changing the structure. Lattice parameters increase slightly with the incorporation of Mn from a = 3.27 Å and c = 5.34 Å to a = 3.35 Å and c = 5.47 Å. The full width at half-maximum (FWHM) of the most intense peak (2θ = 30°) barely changed (form 0.012 to 0.013 rad).

The transmission of the multilayers (Fig. 2) increases slightly with adding 5% Mn, and both samples show a high transmission in the UV–Vis, at λ = 600 nm, 58.8% for the non-doped sample, and 77.1% for the doped one, their thickness is around 400 nm. The refractive index is the same for both materials, 1.89, which could be due to the absence of polarization because the atomic radiuses of Zn and Mn are so close

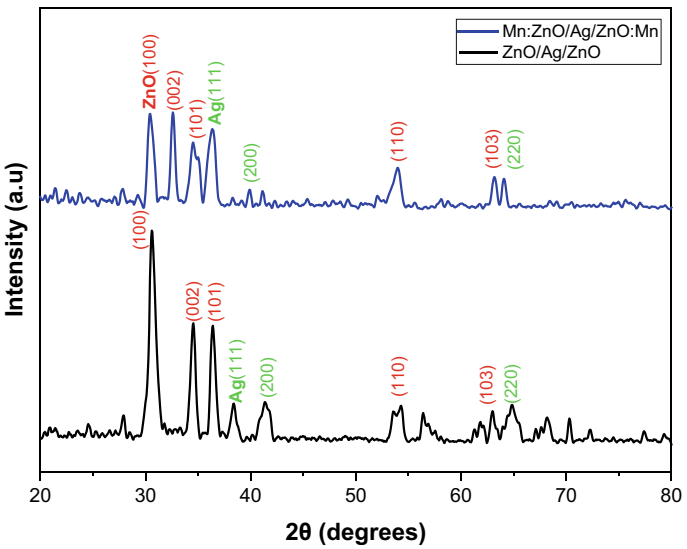


**Fig. 1** XRD patterns of ZnO/Ag/ZnO and Mn:ZnO/Ag/ZnO:Mn multilayers

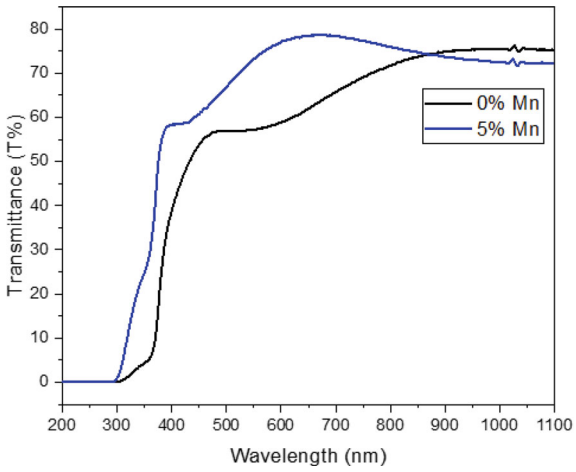


**Fig. 2** The transmittance spectra of ZnO/Ag/ZnO and Mn:ZnO/Ag/ZnO:Mn multilayers

[15], and Mn is introduced in a weak percentage. On the other hand, the extinction coefficient (k) increased significantly from 0.013 to 0.043.

By assuming that the transition between the valence and the conduction bands in ZnO is direct, we could calculate the energy gap (Eg) from the following equation:

$$\alpha h\upsilon = A(h\upsilon - Eg)^{1/2} \tag{1}$$

where α is the absorption coefficient, A is a constant, hυ is the photon energy, and Eg is the optical band. Figure 3 shows plots of $(\alpha h\upsilon)^2$ versus (hυ). The optical band gap of samples was calculated from these plots by extrapolating the linear region of the resulting curve to $(\alpha h\upsilon)^2 = 0$. The values of Eg for ZnO/Ag/ZnO and Mn:ZnO/Ag/Mn:ZnO are respectively 3.38 eV and 3.81 eV. The incorporation of Mn decreases the wavelength and therefore increases the optical gap.

The sheet resistance and resistivity of the multilayer films were characterized, as shown in Table 1. They both decreased from 271.8 Ω to 163.08 Ω and from 0.011 Ω cm to 0.007 Ω cm, respectively, due to the increase in mobility and carrier concentration of charges according to Schottky theory [16–18]. As a result, the conductivity increases. These results are great compared to ZnO single layer sheet resistance (180 kΩ) reported by Hong et al. [19], which confirms that the Ag layer plays an essential role in increasing charge carriers to produce conductivity.

The conductivity of the multilayers is mainly due to the silver interlayer sandwiched between the two dielectric zinc oxide layers [17, 20]. In 1976, Haacke [21] proposed a factor called the figure of merit (Φ), which is a correlation between the optical properties and the electrical properties; this factor is defined as the ratio between the transmission in the visible (400–800 nm) and the sheet resistance:

$$\Phi = \frac{T_{600nm}}{R_s} \tag{2}$$

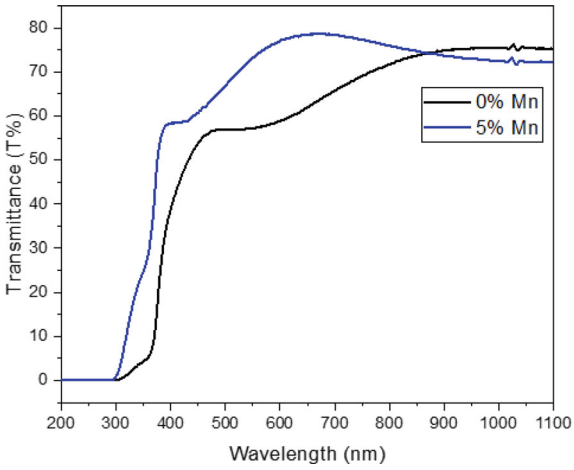


**Fig. 3** The plots of $(\alpha h\upsilon)^2$ as a function of photon energy

**Table 1** Sheet resistance, resistivity, conductivity, and figure of merit of the non-doped and doped multilayers

| Mn percentage | Sheet resistance Rs (Ω) | Resistivity ρ (Ω cm) | Conductivity $\sigma$ ($\Omega^{-1}$ $cm^{-1}$) | $\Phi \times 10^{-3}$ ($\Omega^{-1}$) |
|---|---|---|---|---|
| 0% | 271.8 | 0.011 | 91.979 | 2.16 |
| 5% | 163.08 | 0.007 | 153.299 | 4.73 |

This factor gives us an idea about the quality and effectiveness of our multilayers. The figure of merit improved by almost 120% by adding 5% of Mn, this is s mainly attributed to the decrease in sheet resistance.

## 4 Conclusion

The optoelectronic characteristics of ZnO/Ag/ZnO and Mn:ZnO/Ag/Mn:ZnO multilayers deposited on glass substrate were investigated. The effect of manganese addition on the structure optical and electrical properties of the multilayers films has been studied. XRD studies show that the Mn incorporated by substitution increasing the lattice parameters slightly due to the slight difference in the ion radius (122 pm for Zn ion and 139 pm for Mn ion). Both samples are transparent in the visible range. The band gap increases from 3.38 to 3.81 eV by adding Mn. We reported higher conductivity and figure of merit after doping, 153.299 $\Omega^{-1}$ $cm^{-1}$ and 4.73 $\times$ $10^{-3}$ $\Omega^{-1}$, respectively.

## References


1. Chen Y (2018) Review of ZnO transparent conducting oxides for solar applications. IOP Conf Ser: Mater Sci Eng 423
2. Dincer I (2000) Renewable energy and sustainable development: a crucial review. Renew Sustain Energy Rev 4
3. Ellmer K, Klein A, Rech B (2007) Transparent conductive zinc oxide: basics and applications in thin film solar cells. Materials science. Springer
4. Manoj PK et al (2007) Preparation and characterization of indium-doped tin oxide thin films. Ceram Int 33(2)
5. Chowdhury FR et al (2011) Optical properties of undoped and indium-doped tin oxide thin films. J Bangladesh Acad Sci 35(1)
6. Mohammad T, Kumar V, Dutta V (2020) Spray deposited indium doped tin oxide thin films for organic solar cell application. Physica E: Low-Dimens Syst Nanostruct 117
7. Ahn BD et al (2007) Influence of thermal annealing ambient on Ga-doped ZnO thin films. J Crystal Growth 309(2)
8. Liu J et al (2012) Effects of Ti-doped concentration on the microstructures and optical properties of ZnO thin films. Superlattices Microstruct 52(4)
9. Wu M et al (2015) Structural, optical, and electrical properties of Mo-doped ZnO thin films prepared by magnetron sputtering. Appl Surf Sci 324
10. Lekoui F et al (2021) Elaboration and characterization of Mg-doped ZnO thin films by thermal evaporation: annealing temperature effect. Braz J Phys 51(3)
11. Kim YS, Tai WP (2007) Electrical and optical properties of Al-doped ZnO thin films by sol–gel process. Appl Surf Sci 253(11)
12. Lekoui F et al (2021) Investigation of the effects of thermal annealing on the structural, morphological and optical properties of nanostructured Mn doped ZnO thin films. Opt Mater 118:111236
13. Ferhati H, Djeffal F (2020) Performance assessment of TCO/metal/TCO multilayer transparent electrodes: from design concept to optimization. J Comput Electron 19
14. Girtan M (2012) Comparison of ITO/metal/ITO and ZnO/metal/ZnO characteristics as transparent electrodes for third generation solar cells. Sol Energy Mater Sol Cells 100
15. Xie GC et al (2012) Effect of In-doping on the optical constants of ZnO thin films. Phys Procedia 32
16. Kim JH et al (2015) Highly flexible ZnO/Ag/ZnO conducting electrode for organic photonic devices. Ceram Int 41(5)
17. Lee JY et al (2009) Dependence of intermediated noble metals on the optical and electrical properties of ITO/metal/ITO multilayers. Opt Commun 282(12)
18. Sahu DR, Lin SY, Huang JL (2006) ZnO/Ag/ZnO multilayer films for the application of a very low resistance transparent electrode. Appl Surf Sci 252(20)
19. Hong CS, Park HH, Moon J (2006) Effect of metal (Al, Ga, and In)-dopants and/or Ag-nanoparticles on the optical and electrical properties of ZnO thin films. Thin Solid Films 515(3):957–960
20. Sharma V et al (2017) High-performance radiation stable ZnO/Ag/ZnO multilayer transparent conductive electrode. Sol Energy Mater Sol Cells 169
21. Haacke G (1976) New figure of merit for transparent conductors. J Appl Phys 47

DOCID 338194

# Influence of Mn doping on the optical property of ZnO thin films

Khaoula Settara[1,*], Hocine Akkari[1] and Fouaz Lakoui[2]

[1] Département de Chimie, Faculté des Sciences, Université 20 août 1955 – Skikda, route d'ElHadaiek, B.P : 26, 21000 Skikda, Algérie.
[2] Centre de développement des technologies avancées, Division des Milieuxionisés& Laser, Cité 20 Aout 1956, Baba Hassen, Alger, Algérie.

Abstract — In this work, we are interested in studying the effect of Mn doping percentage on the optical properties of zinc oxide (ZnO). Pure and Mn doped ZnO thin films were deposited onto the glass substrates by vacuum thermal evaporation then the samples were annealed under atmosphere at 500 °C to ensure the oxidation of ZnO. The optical property of these films was determined from the transmission measurement in the range of 250 - 600 nm using UV-visible transmission spectroscopy. The spectra are compared to the UV-visible spectrum of the glass substrate, we can conclude that the addition of Mn to ZnO thin films increases the wavelength and therefore decreases the optical gap.

Keywords: ZnO thin films, Mn doped ZnO, thermal evaporation, optical propreties.

Khaoula94stt@gmail.com